A Search for Radio Emission Coincident with Gamma-Ray Bursts

Richard Joseph Balsano

A Dissertation
Presented To The Faculty
Of Princeton University
In Candidacy For The Degree
Of Doctor Of Philosophy

Recommended For Acceptance
By The Department Of
Physics

January 1999

Abstract

For a few seconds, a gamma-ray burst (GRB) can be the brightest object in the hard X-ray and soft γ-ray sky. Despite over twenty years of observations, the origin of GRBs remains a mystery. Even two years ago, the basic question of whether GRBs are objects in our own galaxy at a distance of $\sim$ 100 kpc, or are in very distant galaxies, $\sim$ 1 Gpc away, was still unanswered. These energetic explosions remain mysterious largely because, prior to early last year, no convincing counterpart at energies below 20 keV had ever been found. Since then, dramatic progress has been made in counterpart searches all across the electromagnetic spectrum. This thesis describes one such experiment, a dedicated search for counterparts to GRBs in the radio band.

We repaired and remotely operated a 74 MHz, 1000 m^2 phased array located in Fallbrook, California, to search for radio emission associated with GRBs. We used a low-cost, custom-built receiving system with coarse spectral resolution. If GRBs emit radio waves, this low frequency signal will be delayed by dispersion in the interstellar and intergalactic medium. With our spectrometer, we can easily distinguish dispersed signals of astronomical origin from the non-dispersed terrestrial interference that is the major background for all radio transient studies. Measuring the dispersion of radio transients associated with GRBs would constrain their distances and the density of the intervening galactic or intergalactic plasma.

Our experiment ran autonomously and could respond within $\sim$ 10 s to the detection of a GRB by an Earth-orbiting satellite. This is the fastest triggered response that has been achieved with observations at any wavelength. We have taken high-quality data on 32 GRBs. In this sample, two radio transients were detected in close temporal association with GRBs, but a physical association between these signals and the GRBs is unlikely. Taken as upper limits, our observations constrain prompt radio emission from GRBs to a few kJy or less.

Contents

List of Figures

List of Tables

Acknowledgments

It is a great pleasure to record for posterity my gratitude to those who have given invaluable support, both professional and personal, through the journey that is graduate school. First and foremost, I would like to thank my adviser Professor Stephen Thorsett for giving me the opportunity to work on what can only be called a "cool" project. His patience and guidance were invaluable with what turned out to be a much more challenging project than I first supposed! It has been a privilege to work under such a "rising star" as Professor Thorsett; he comes up with many slick ideas and has been a great mentor. I have to also thank Steve for introducing me to *real* beer and body surfing "native style".

I would like to acknowledge the financial support for myself and the project described in this thesis. I thank the California Institute of Technology and Princeton University for support, including a tuition waiver from Princeton. The project described here received funds from: the Dudley Observatory under an Ernest F. Fullam Award, NASA through the CGRO and HST Guest Investigator programs and NSF through a small grant for exploratory research.

All rapid GRB follow-up experiments currently depend on the GRB coordinate network set up by Scott Barthelmy at NASA's Goddard Space Flight Center. Without Scott's large effort none of these experiments would be possible. I greatly appreciate Scott's efforts and his willingness to answer many questions about the system as I was learning how to use it.

This project would not have been possible without the radio array built by Professor Bill Coles and colleagues at UCSD. I would also like to thank Bill and Professor Barney Rickett for dispensing much wisdom on radio circuit design and debugging, as well as much needed advice on working with custom radio antennas.

Thanks to Paul Ray for taking a break from pulsar timing and applying his computer talents to the initial FLIRT software development. Thanks also to Tom Prince for lending us a computer (& Paul) in the early days of the experiment. Thanks to Jason Rhodes for help in the early stages of FLIRT and for being a traveling buddy in our exile to Hawaii on Hubble business. It is a great pleasure to acknowledge Michael Liu from UCSD for an excellent job constructing the FLIRT spectrometer; it is a beautiful piece of work. Thanks to Eric Splaver who helped me to improve this thesis by offering much editorial advice. Also I extend a great big thanks to Tom Chester of Fallbrook, California for enthusiastically volunteering time for site visits when things broke, which was all too often with El Niño battering Southern California.

Working on a remote radio antenna in California while one is a graduate student in New Jersey puts some strains on the travel budget. I, and my funders, owe a great debt to Bill and Alma Coles as well as Barney and Holly Rickett for graciously offering housing during my trips to the San Diego area. The fresh fruit from the Coles' backyard was fantastic; seeds from loquats in their yard are now small trees, ensuring that at least something from my graduate days will bear fruit! Thanks also to Sandip and Mahasweta Sarkar for being wonderfully generous with their home in San Diego and in teaching me about all things Indian.

I've made many friends here in Princeton who have all made the experience much more enjoyable. I thoroughly enjoyed my time spent with Nick Hand and the rest of the Princeton Aikido crowd; I hope that we'll have many future meetings on and off the mat. Thanks to Ingrid for putting up with this cynic in many a late night discussion in the Pulsar lab. Thanks to Dave Pottinton for making many days and nights much more enjoyable with his wonderful British wit. Christopher Harrison greatly expanded my view of New Jersey by taking me on many great biking expeditions and introducing me to mountain biking New Jersey style. Karen and Weihsueh made recent life bearable by being steadfast thesis comrades, enjoying many late night tea sessions and by knowing the questions not to ask. I owe a great debt of gratitude to Mark for making me go where I needed to go and to Dave, Mark, Weihsueh and Karen for all visiting me while I was there. And, Aida, medu moj, thanks for being a patient partner and making my final months in Princeton much happier.

And, of course, who could ever even make it to graduate school, let alone through it, without the love and support of lifetime friends and family. Niki and Kedrick, thanks to both of you, for having seen me through thick and thin. Thanks also to my siblings, Bernie, Treace (wherever you are now), Jeff and Shari for being there for

me. Dad, thanks for encouraging me in all things scholastic and, Mom, thanks for always listening and being supportive even when I was speaking of the most foreign things.

Finally, I dedicate this thesis to my niece, Samantha LaVassor. Reach for the stars kid!

Chapter 1

Gamma-ray bursts: a brief history

1.1 Introduction

The discovery of gamma-ray bursts of cosmic origin is a good example of serendipity in science. In 1968, Colgate suggested that a supernova, the explosive death of a massive star, might be accompanied by a burst of γ-rays. Klebesadel, Strong and Olson (1973) searched for such bursts in archival data from the U.S. Department of Defense's *Vela* satellites*. The search produced sixteen bursts of γ-rays, but the times and positions of the events did not match any known supernovae. The Sun and Earth were also ruled out as the source of the mysterious signals. Thus began the search for the origin of gamma-ray bursts that continues today.

If the gamma-ray bursts (GRBs) were not associated with supernovae, what were they? Klebesadel and co-workers could not answer that question, but they provided the first glimpse of what defines a GRB. In those sixteen events, they found some that lasted a small fraction of a second and others that lasted tens of seconds. The detectors used onboard *Vela* were sensitive to radiation in the range $0.2 - 1.5$ MeV, so these events released energy in the hard X-ray to soft γ-ray portion of the electromagnetic spectrum. This type of radiation was suggestive of very energetic explosions. By everyday standards, the energy delivered to Earth by a GRB is very small. A square detector one meter on a side would have detected only $\sim 10^{-8} - 2 \times 10^{-7}$ J from one of these first GRBs; that is roughly equivalent to the amount of energy required to lift a grain of sand 1 cm. However, by astronomical standards, GRBs deliver an enormous amount of energy to the Earth. A GRB can temporarily outshine all other

*The *Vela* satellites were designed to detect nuclear blasts in space as a part of nuclear test ban treaty verification.

sources of γ-rays on the sky combined.

This thesis describes an effort to detect radiation from GRBs in the low-frequency radio band. To put this experiment into context, this introductory chapter will review the basics of GRB observations, the topic of §1.2. Present knowledge of GRBs at energies below γ-rays is the subject of §1.3. Models for GRBs are reviewed in §1.4. In §1.5 other γ-ray phenomena which are observationally similar to GRBs are discussed. Finally, §1.6 provides the justification for looking for counterparts to GRBs in the radio, at a frequency eleven orders of magnitude away from γ-rays.

1.2 What are gamma-rays bursts?

The Earth's atmosphere is, fortunately for us, quite opaque to γ-rays, so studies of GRBs must be undertaken with satellites. Many satellites have contributed to the progress made in understanding GRBs in the last thirty years. Here, however, we rely on the particularly noteworthy contributions of two recent satellites. *NASA's Compton Gamma-Ray Observatory (CGRO)* with its Burst and Transient Source Experiment (BATSE) (Paciesas *et al.* 1989; Fishman *et al.* 1989) has observed more than two thousand GRBs (Meegan *et al.* 1998a; Fishman *et al.* 1994b), the largest dataset of GRBs to date. The Italian-Dutch *Satellite for X-Ray Astronomy (BeppoSAX)* with its Gamma-Ray Burst Monitor (GRBM) (Feroci *et al.* 1997) and Wide Field Cameras (WFC) (Jager *et al.* 1997), on the other hand, has provided critical data on a small number of GRBs, leading to the first confirmed counterparts to GRBs below X-ray and γ-ray energies. In this section, a broad overview of the observed properties of GRBs is given, drawing extensively on data from these two satellites.

1.2.1 Observations

Time Series

Perhaps the most striking feature about GRBs is the large temporal diversity they exhibit. GRBs have durations in the range $t_{90} \approx 10^{-2} - 10^{3}$ seconds, where $t_{90}$is the time over which 90% of the γ-ray flux is received (see Figure 1.1). In addition to this wide range of observed durations, as can be seen in Figure 1.2, no two GRBs look exactly alike. The diversity in the temporal structure of bursts must be accounted

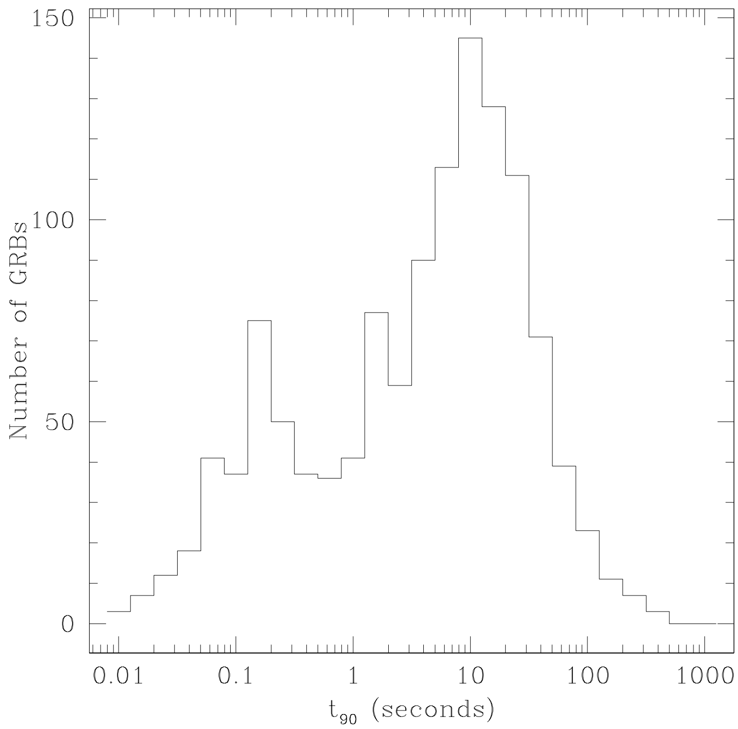

Figure 1.1: Histogram of BATSE GRB t_{90} values. The t_{90} is the time over which 5% to 95% of the flux from the GRB is measured. The bimodal shape of the distribution has been taken as evidence for two underlying populations of GRBs (Hurley 1992; Fishman *et al.* 1994b).

for in any model of GRB origins. This great variety suggests that GRBs may not be the result of a single phenomenon.

Spectra

GRBs are very energetic events, with a typical flux of $\sim 10^{-6} - 10^{-4}$ erg cm^{-2} in the energy range 20 keV $-$ 1 MeV, with most of the energy emitted in photons above 0.1 MeV. The time-averaged spectra are well described by an empirical (non-thermal) model:

$$N_e(E) \propto \begin{cases} E^{\alpha} \exp(-E/E_0) & , \quad E \leq (\alpha - \beta)E_0 \\ E^{\beta} & , \quad E \geq (\alpha - \beta)E_0, \end{cases} \tag{1.1}$$

with where N_e is the number of photons per unit area per unit energy over the duration of the burst, E_0 is a break energy and α and β are low and high energy power law

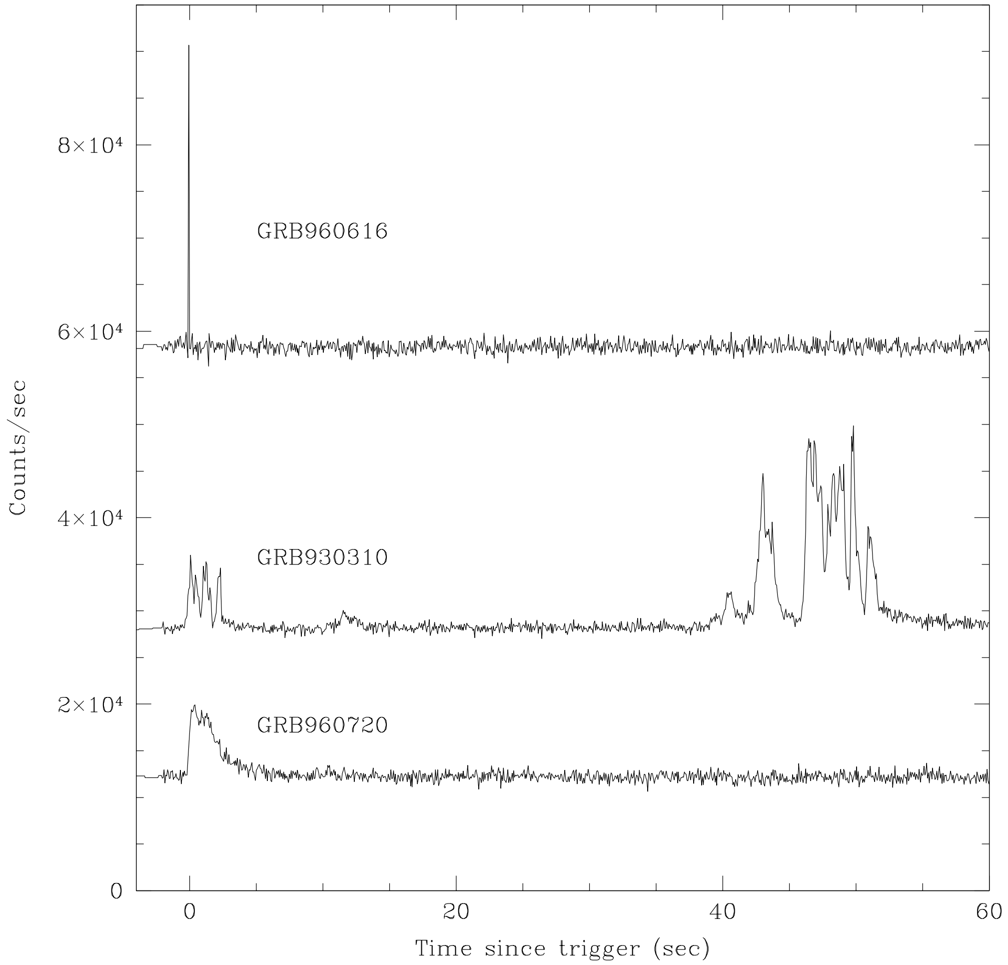

Figure 1.2: The BATSE light curve for GRB960720, GRB930310 and GRB960616; the latter two have been offset by 20,000 and 40,000 counts/sec respectively. GRB960720 has a sharp rise and a smooth decay while GRB930310 shows obvious structure and subpulses on multiple timescales. GRB960616 is a simple spike with no obvious structure, although it is brighter than both GRB930310 and GRB960720.

indices respectively. Fits to GRB spectra gives parameters with the following limits: $10 \lesssim E_0 \lesssim 1500$ keV, $-1.5 \lesssim \alpha \lesssim 2$ and $-5 \lesssim \beta \lesssim -1.5$ (Band *et al.* 1993). In Figure 1.3, a sample spectrum of the form in Equation 1.1 is plotted; from the figure, it is clear that this representation is simply a smooth, broken power law.

The time-averaged spectra wash out details, however, since some GRBs have spectra whose peak power shifts from higher to lower energy as the burst progresses

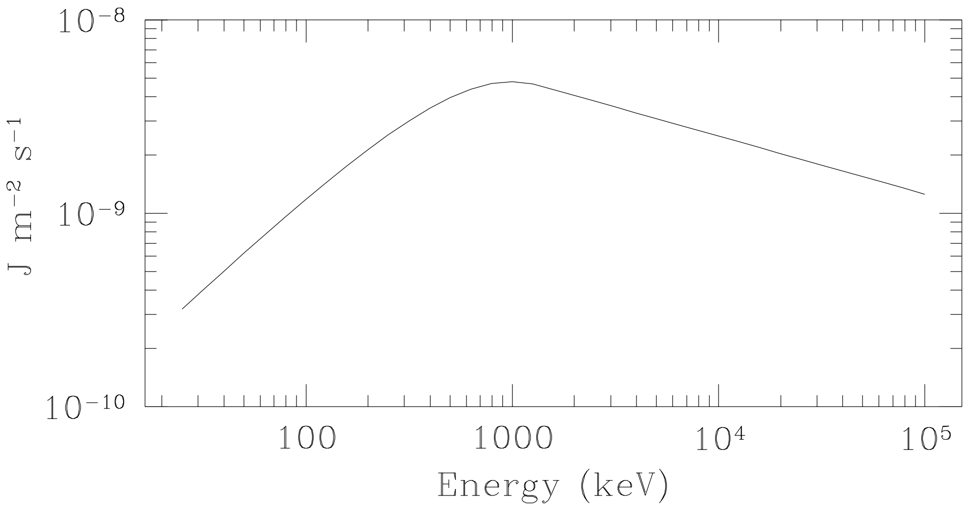

Figure 1.3: A Band *et al.* (1993) spectrum with $\alpha = -1$, $\beta = -2.3$, and $E_0 =$ 1000 keV.

(so-called "hard-to-soft evolution") (Bhat *et al.* 1994; Ford *et al.* 1995).

Studies on BATSE and Solar Maximum Mission data have shown that the BATSE sample of GRBs is somewhat incomplete for bursts with peak power at energies above ~ 1 MeV (Lloyd and Petrosian 1998; Harris and Share 1998). Nevertheless there is a steep drop-off in the number of bursts with peak energies above ~ 2 MeV so that, at least as far as peak energy is concerned, GRBs are hard X-ray/soft γ-ray phenomena. However, γ-rays from GRBs are sometimes seen at very high energies; the highest energy photon associated with a gamma ray burst was 18 GeV (Hurley 1994).

GRB directions

In addition to the properties of individual bursts, it is interesting to look at the large sample of GRBs as a group to search for hints about their origins. In astronomy, one of the primary means of identifying the source population for an unknown type of event is to observe the two-dimensional distribution of objects on the sky and, if possible, the radial distribution as well. Various distributions, e.g. ecliptic or galactic, can readily be identified in this fashion.

The large sample of GRBs from BATSE confirmed earlier suspicions that the Earth lies at the center of a bounded (Meegan, Fishman and Wilson 1985) and isotropic (Klebesadel *et al.* 1982, Atteia *et al.* 1987), distribution of GRB sources (Meegan

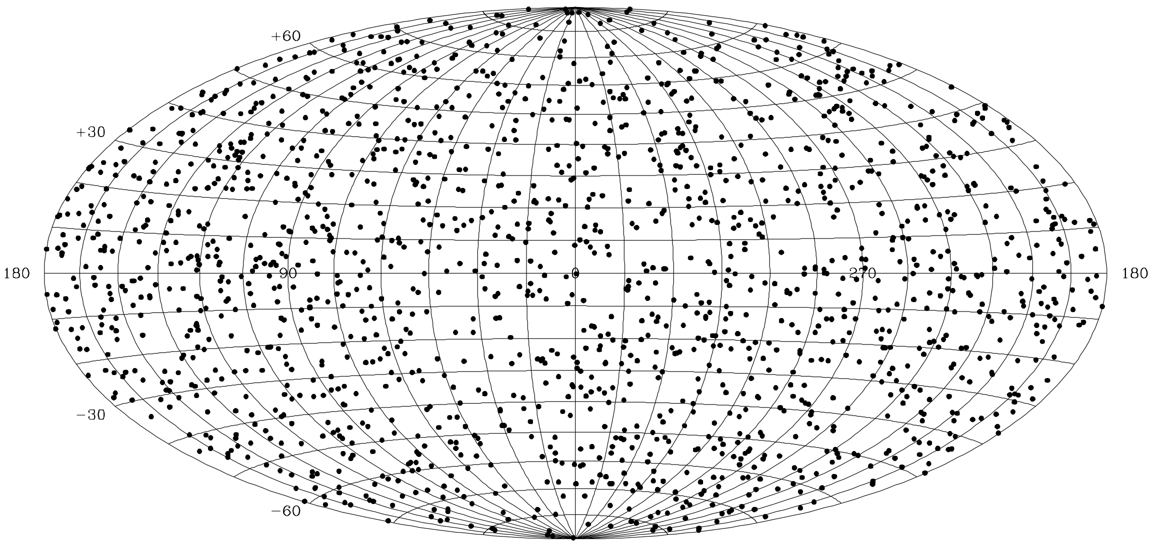

Figure 1.4: Locations for 1637 GRBs in galactic coordinates. The isotropy of GRBs has been taken as strong evidence for a cosmological origin of GRBs (Meegan *et al.* 1992; Briggs *et al.* 1996).

et al. 1992; Fishman *et al.* 1994b; Briggs *et al.* 1996). The fact that GRBs are isotropic on the sky is obvious from Figure 1.4; the number of GRBs per steradian is consistent with a constant across the sky. Analysis shows that their distribution is inhomogeneous, however, and this requires comment. If GRBs were a homogeneous population, then as a detector sampled weaker and weaker sources, the number of GRBs detected would be expected to grow as

$$N \propto P^{-3/2} \tag{1.2}$$

where N is the number of bursts with a peak flux greater than P. Equation 1.2 follows from the fact that the volume sampled grows as R^3 while the intensity of radiation falls off as R^2. Thus, for a homogeneous population, the $\log N - \log P$ plot should follow a $-3/2$ power law (cf. Figure 1.5).

This bounded, heliocentric distribution is consistent with sources from at least 3 separate distance scales: the Oort cloud (~ 0.1 pc) (e.g. Bickert and Greiner 1993), a galactic "corona" (~ 200 kpc, see Lamb 1995 for a review), or at cosmological distances (~ 1 Gpc, see Paczyński 1995 for a review). For the Oort cloud scale,

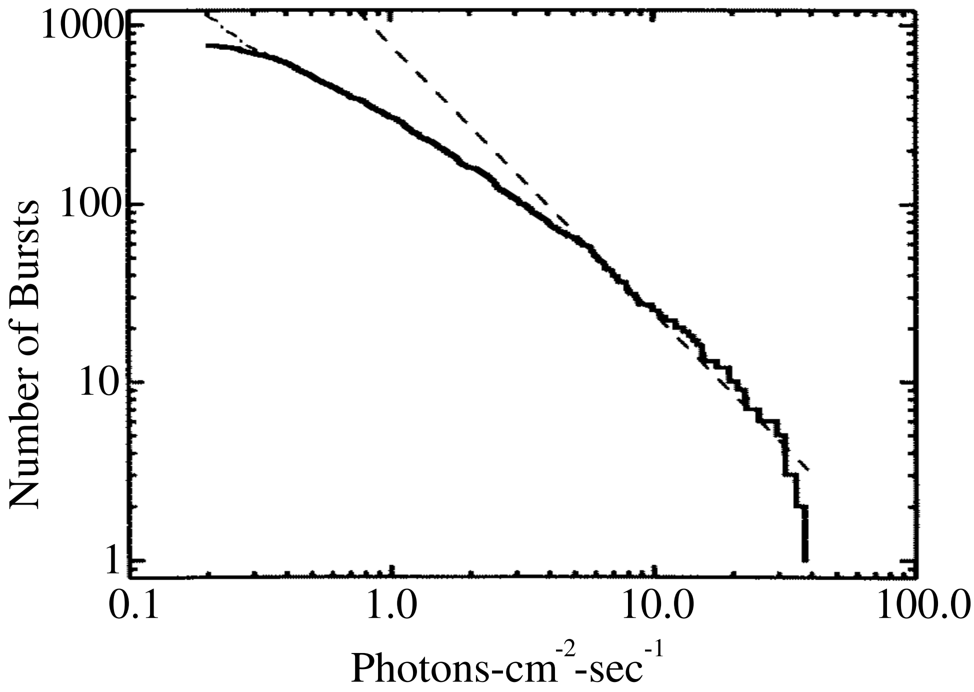

Figure 1.5: Number of bursts plotted against the BATSE one second peak flux in the $10-300$ keV band (adapted from Pendleton *et al.*, 1996). The dashed line shows the $-3/2$ power law expected for an isotropic distribution.

the sources must be at a distance $\gg$ 1AU so that the Earth-Sun distance does not introduce noticeable anisotropy. For similar reasons, in galactic models, the bursts must be at sufficient distance that the Sun's distance from the Galactic center is negligible. Given the lack of a plausible mechanism for release of γ-rays in the Oort cloud (Clarke, Blaes, and Tremaine 1994), the debate focused on the latter two scales. One of the goals of the experiment described in this thesis was to resolve this debate.

For a much more detailed, but slightly dated, overview of GRB observations, the reader is directed to Fishman & Meegan (1995).

1.3 Delayed low energy observations

Prior to the two years ago, the positions of GRBs on the sky were generally only known to several degree accuracy. In the last 24 months, however, GRB positions with several arcminute, rather than several degree, accuracy have become available just hours after a few GRBs. About 19 bursts have been localized with small position error boxes, either using the Wide Field Cameras (WFCs) of the *SAX* satellite or the All-Sky Monitor (ASM) of the Rossi X-Ray Timing Explorer (XTE). Follow-up observations have led to X-ray, optical and radio counterparts in roughly 70%, 50% and 25% of the GRB position error boxes respectively. Because these counterparts are detected hours or more after the GRB has faded, they are referred to as "afterglows." Using the accurate positions from optical and radio counterparts, three host galaxies have been identified at high redshift. These results are summarized in Table 1.3.

Selected X-ray, optical and radio data are described in the following sections. The results are generally in good agreement with the cosmological fireball models discussed in §1.4.3. However, the number of GRBs with accurate positions is still small, and strongly biased by observational constraints. In §1.5, some remaining uncertainties are discussed, including the possibility that GRBs arise from a heterogeneous source population.

1.3.1 X-ray observations

One of the first GRBs to be well-localized by *SAX* was GRB970228[†] (Costa *et al.* 1997b; Costa *et al.* 1997a). A new X-ray source in the error box for GRB970228 faded by a factor of roughly 20 in a matter of 3 days, following a $t^{-1.3}$ power law decay in intensity (Costa *et al.* 1997a). Other bursts have shown similar behavior, but a notable exception is GRB970111 (Feroci *et al.* 1998a). This GRB was one of the brightest seen by *SAX*. The γ-ray fluence of GRB97011 was ~ 3 times as large as that of GRB970228, while its X-ray afterglow was at least ~ 10 times weaker than the X-ray afterglow of GRB970228 (Feroci *et al.* 1998a). This clearly indicates that X-ray afterglows do not simply scale with the energy of the GRB.

1.3.2 Optical observations

The rapid localization of the X-ray counterpart to GRB970228 led to the discovery of an optical counterpart (van Paradijs *et al.* 1997); a pointlike object was discovered that varied by > 2 mag in 8 days. By March 9, 1997, the optical transient had faded enough that an object with integrated magnitude $R \approx 24$ was detected at the same position. This object has been taken to be the host galaxy of the optical transient.

[†]The current method of naming GRBs is to append the UT date of discovery to "GRB" with an optional alphabetic suffix if more than one GRB is detected on a given day. For instance, GRB790305 occurred on March 5, 1979.

Table 1.1: Summary of afterglow detections adapted from Greiner (1998).

GRB	RA hh:mm:ss	DEC	Error $'$	Detector[a]	X[b]	O[b]	R[b]	IAUC[c]
960720	17:30:37	$+49°05.8'$	3	WFC	n	n		6467, 6569
970111	15:28:15	$+19°36.3'$	3	WFC	n	n		6533, 6569
970228	05:01:57	$+11°46.4'$	3	WFC	y	y		6572
970402	14:50:16	$-69°19.9'$	3	WFC	y	n		6610
970508	06:53:28	$+79°17.4'$	3	WFC	y	y[e]	y	6649, 6654
970616	01:18:57	$-05°28.0'$	40×2	XTE/Uly	y	n		6683, 6687
970815	16:08:43	$+81°30.6'$	6×3	ASM	y	n		6718
970828	18:08:29	$+59°18.0'$	2.5×1	ASM	y	n		6726, 6728
971024	18:24:51	$+49°28.9'$	9.0×1	ASM	y	n		priv. comm.
971214	11:56:30	$+65°12.0'$	4	WFC	y	y[e]		6787, 6789
971227	12:57:35	$+59°15.4'$	8	WFC	?	?		6796
980109	00:25:56	$-63°01.4'$	10	WFC	n	n		6805
980326	08:36:26	$-18°53.0'$	8	WFC	?	y		6851
980329	07:02:41	$+38°50.7'$	3	WFC	y	y	y	6853
980425	19:34:54	$-52°49.9'$	8	WFC	?[d]	SN?[d]	y?[d]	6884
980515	21:18:04	$-67°14.9'$	5	WFC	?			6909
980519	23:22:14	$+77°15.3'$	3	WFC	y	y	y	6910
980613	10:17:46	$+71°29.9'$	4	WFC	y	y		6938
980703	23:59:07	$+08°35.6'$	4	ASM	y	y[e]	y	6966

[a] X-ray instrument which localized GRB; WFC = SAX Wide Field Camera, ASM = XTE All Sky Monitor, XTE/Uly = Combination of XTE Proportional Counting Array scan error box and Interplanetary Network annulus.
[b] X, O and R are X-ray, optical and radio counterpart detections respectively, a '?' appears where the association is tentative.
[c] IAU Circular in which detection of the GRB was published.
[d] SN1998bw was discovered in the error box of GRB980425 and was seen in both the optical and radio. A fading X-ray source was also detected in the GRB error box, but at a position inconsistent with that of the SN.
[e] Spectrographic redshifts of the optical transients and/or galaxies for 970508, 971214 and 980703 are 0.835, 3.14 and 0.966 respectively.

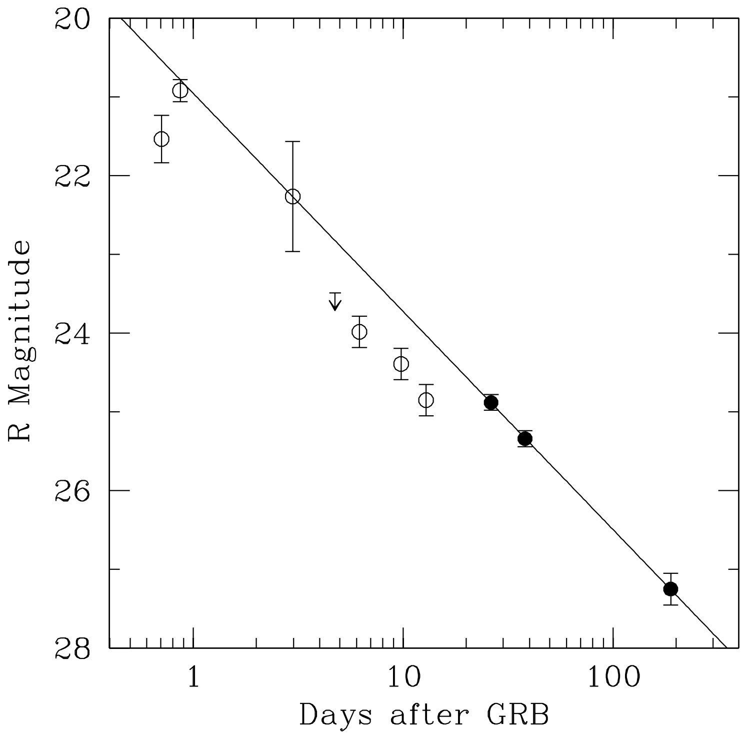

Figure 1.6: The R Band lightcurve for GRB970228. The line is a power law fit to the Hubble data points (shown with black symbols); the best fit exponent is 1.14 ± 0.05 (from Fruchter *et al.* 1998b).

Although the spectrum of the galaxy does not have absorption or emission features with which a redshift could be measured, this GRB is consistent with happening in a distant galaxy.

Hubble Space Telescope Imaging Spectrograph observations of the optical transient taken roughly 200 days after the burst detected the galaxy at $V = 25.7 \pm 0.25$, and the transient at $V = 28.0 \pm 0.25$, consistent with an $\alpha = -1.14 \pm 0.05$ power-law decay in brightness (Fruchter *et al.* 1998b) (see Figure 1.6).

A little over 2 months after the GRB, the optical counterpart to GRB970508 (Djorgovski *et al.* 1997) was detected and a redshift of $z \geq 0.835$ based on absorption

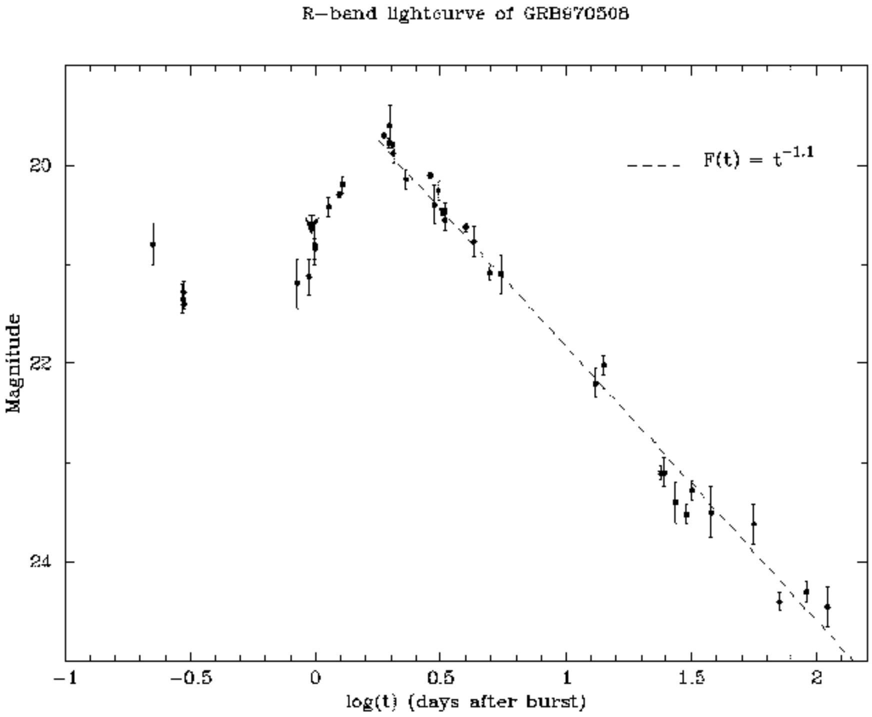

Figure 1.7: The R Band lightcurve for GRB970508 (courtesy of Titus Galama).

in FeII and MgII was measured (Metzger *et al.* 1997b); a lack of a Lyman-α forest constrained $z < 2.3$. Roughly another month later, O II emission lines from the underlying host galaxy were seen at the same redshift, $z = 0.835$ (Metzger *et al.* 1997a).

The optical emission from GRB970508 was different from that of GRB970228. As can be seen in Figure 1.7 (also, see Pedersen *et al.* 1998), the optical transient associated with GRB970508 peaked in brightness roughly 2 days after the GRB and then decayed as a power law. This is in contrast to the behavior seen in the optical afterglow of GRB970228 in which the initial rise, if it occurred at all, happened over several hours rather than several days. The final power law decay with exponent $\alpha = -1.21$, however, is within errors of the value for GRB970228.

The third confirmed optical counterpart to a GRB was that found in association with GRB971214 (Halpern *et al.* 1998). By identifying Lyman-α emission in the host galaxy, Kulkarni, *et al.* (1998) found a redshift of $z = 3.42$ for this burst, putting isotropic energy losses at $\sim 3\times 10^{53}$ erg, which is very near the total energy budget in neutron star merger models (see e.g. Narayan, Paczyńskiand Piran 1992). If, however, the γ-rays were highly beamed, neutron star merger models would still be viable for this burst. The lightcurve for this GRB had a power law decay with exponent $\alpha = -1.4\pm 0.2$ (Halpern *et al.* 1998), which is, again, consistent with those measured for GRB970228 and GRB970508. The lightcurve flattens out roughly two weeks after the GRB, due to luminosity from the underlying galaxy.

1.3.3 Radio observations

Paczyński and Rhoads (1993) first suggested that a GRB might lead to a radio signal at the mJy level roughly a week after a GRB. Thus far, only 4[‡] of the 19 rapidly well-localized GRBs have had radio counterparts despite an ongoing observing campaign (Frail 1998; Frail *et al.* 1997b; Galama *et al.* 1997).

The first two radio counterparts seen were GRB970508 (Frail *et al.* 1997a; Taylor *et al.* 1997) and GRB980329 (Taylor *et al.* 1998). The GRB970508 radio source was ~ 0.6 mJy at 4 and 8 GHz (Frail *et al.* 1997a) at late times, in rough agreement with model predictions (Paczyński and Rhoads 1993). Perhaps more interesting than the use of the radio afterglow to constrain afterglow models (Waxman, Kulkarni, and Frail 1998) is the idea that radio afterglows should scintillate in analogy with the twinkling of stars. Goodman (1997) predicted that the size of the expanding fireball producing the afterglow emission was ~ 3 μarcsecond initially and ought to undergo diffractive scintillation (large-scale fluctuations in intensity do to interference along multiple paths from the source) until the size reaches the critical angular size given by

$$\theta_s < 2.25\left(\frac{\nu}{10\ \mathrm{GHz}}\right)^{6/5}\left(\frac{d_{scr}}{1\ \mathrm{kpc}}\right)^{-1}\times (SM_{-3.5})^{-3/5}\mu\ \mathrm{a.s.}$$

where d_{scr} is the distance to the "scattering screen" producing the multiple paths and $SM_{-3.5}\equiv (SM/10^{-3.5}\ \mathrm{m}^{-20/3}\mathrm{kpc})$ is the integral along the line of sight of the magnitude of fluctuations causing scattering. After the source expands beyond this angular size, the diffractive scintillation is quenched and more modest fluctuations (refractive scintillation) are seen. Thus, with knowledge of the scattering parameters, one may indirectly resolve the fireball. Assuming that the early variability can thus be ascribed to diffractive scintillation, the size of the fireball in the first few weeks is $R\sim 10^{17}$cm (Frail *et al.* 1997a).

[‡]A fifth association is more controversial (see §1.5.4).

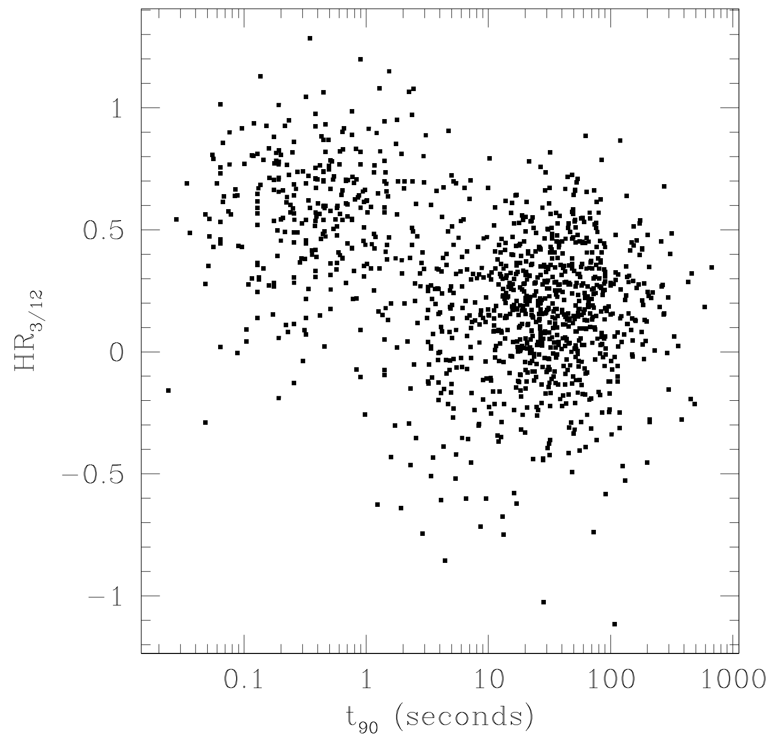

Figure 1.8: The ratio $HR_{3/12}$ of BATSE channel 3 fluence ($100-300$ keV) to combined channel 1 and 2 ($25-100$ keV) fluence plotted versus the duration of the burst. Two loci are clearly apparent and may represent two underlying populations.

1.3.4 Classifications of bursts

As is apparent from GRB time series (e.g. Figures 1.2), GRBs may not be a single phenomenon but a class of one or more distinct types of explosions. Further evidence for such a division is seen in Figure 1.8, a plot of the hardness ratio against the duration of the event. (The hardness ratio is the ratio of high to low energy γ-ray fluence and is analogous to a color in optical astronomy.) A convincing case can be made that short, spectrally harder GRBs may be a distinct class (Kouveliotou *et al.* 1993; Kouveliotou *et al.* 1996a). Furthermore, Belli (1997) finds a concentration of GRBs toward the galactic plane once separations based on spectral hardness and duration are applied.

There is also some evidence for a third class of GRBs hidden in the t_{90} distribution. Mukherjee *et al.* (1998) perform a multivariate analysis uncovering a third population of GRBs. The populations have typical durations of 0.3 s, 4 s and 30 s respectively. A similar result is obtained by performing a less-sophisticated set of log-normal Gaussian fits to the t_{90} distribution (Horváth 1998).

There is more evidence of diversity among GRBs based on their spectra. Pendleton *et al.* (1997) splits GRBs into groups based on a high energy spectral index into no high-energy (NHE), with no emission above 300 keV, and high energy (HE), with emission above 300 keV. They conclude that both types of emission are real states and can be seen in the same burst in different peaks, that is, peaks within the same burst can be of HE or NHE type. Thus, a single source can produce two distinct types of emission. Additionally, both NHE and HE emission are seen in both short and long bursts so that if the classes in, for example, Kouveliotou *et al.* (1993), represent different physical objects, then both classes of objects must be capable of producing two types of emission.

Models of GRBs must account for the temporal diversity seen in GRBs, the two loci of bursts in the duration-hardness plane, a possible third underlying population of bursts in the t_{90} distribution, and the groupings of GRBs based on HE and NHE emission. Whether this diversity represents different emission processes or different physical objects or both is unclear at this time. Given this uncertainty, one should be cautious about generalizations concerning GRBs as a class from observations of a small number of GRBs. This theme is taken up again in §1.5 in which other transient γ-ray phenomena are discussed. Each of the phenomena discussed there was at one point difficult to distinguish from "classical" GRBs. Given that, it is quite possible that the "classical" GRBs discussed here will again be subdivided once future experiments have elucidated their defining properties. Before turning to such considerations, we briefly review some GRB theory.

1.4 Models

The ultimate source of energy in GRBs is still a mystery, but considerable progress has been made in understanding what produces the GRB itself. An explosion releases $\sim 10^{52} - 10^{53}$ ergs, or $\sim 0.01 - 0.1 \times \mathrm{M}_{\odot}\ c^2$, in γ-rays in a matter of seconds. A shock wave is then produced which accelerates some material to Lorentz factors of $\Gamma \sim 10^2 - 10^3$ ($v \sim 0.99995 - 0.9999995 \times c$!) (Piran and Shemi 1993). Two basic ideas exist for producing the γ-rays. In the first scenario, a velocity distribution within the relativistic outflow causes internal shocks which lead to emission of γ-rays and account for the rapid time variability. In the second scenario, the shocks are produced by the relativistic material sweeping up matter external to the source. In either case, the shocked material expands and cools. While expanding, the material sweeps up matter from the surrounding medium and begins to emit synchrotron radiation at lower energies, thereby producing an "afterglow"; this is precisely the relativistic analog of a supernova explosion. This rough picture, and what we know about it, is what we will turn to next.

1.4.1 Fueling a fireball

At the very heart of the GRB mystery is the ultimate source of energy for these explosive events. As of 1994, there were already over 100 published models for the origins of GRBs (Nemiroff 1994), spanning the allowed distance scales discussed in §1.2.1. Prior to the launch of *CGRO*, most models placed GRBs on neutron stars in the galactic disk. As discussed above in §1.2.1 and §1.3, the cosmological distance of at least some GRBs is now well established. Harding (1994) gives a good review of the transition from galactic disk to galactic corona and cosmological models and the problems encountered by each.

Having settled on a cosmological distance scale, Piran (1997) gives the following requirements for any internal engine for GRBs:

- capability of accelerating $4 \times 10^{-8} \left(\frac{\Gamma}{100}\right)^{-1} M_\odot$ per steradian to $\Gamma > 100$,
- a minimum of $10^{46} \left(\frac{\Gamma}{100}\right)^{-2}$ ergs (assuming full relativistic beaming),
- at most $5 \times 10^{-7} \left(\frac{\Gamma}{100}\right)^{-1} M_\odot$ in baryons (assuming a spherical burst),
- modulation of γ-ray emission on timescales of $10^{-3} - 10^{3}$ seconds,
- a source size of < 1000 km, and
- capability of producing high energy photons with 8×10^{48} ergs steradian^{-1} and a small amount of baryon contamination ($< 4 \times 10^{-8}$ $M_\odot$ steradian^{-1}).

Given that energy requirements for cosmological GRBs are of order $M_\odot c^2$, it is natural to consider models involving the destruction of stellar mass objects, such as binary neutron star mergers and endpoints in the evolution of massive stars. Models generally start with the formation of a black hole surrounded by a massive accretion disk. They differ in how the black hole is formed and in how energy is extracted as a GRB.

The merger of compact objects, either in a neutron star-black hole binary or a neutron star-neutron star binary (Paczyński 1986), is a popular model for producing GRBs. The main appeal of these models is that we know of NS-NS binaries that must eventually inspiral due to energy loss through gravitational radiation (Taylor and Weisberg 1982). There is little doubt that sufficient energy for a burst is available; the difficulty lies in efficiently producing γ-ray radiation. Most attempts have focused on neutrino annihilation, but this appears to be several orders of magnitude too inefficient (Jaroszynski 1996; Vietri 1996; Ruffert, Janka, and Shäfer 1996; Mészáros and Rees 1997b).

An alternative to the merger model is that of a "failed" type 1b supernovae (Woosley 1993), which could occur when a Wolf-Rayet star exhausts its fuel and collapses. A Wolf-Rayet star, an O type star of mass $\gtrsim 25-40$ $M_\odot$ that has driven off its hydrogen envelope and exposed a helium burning core, is preferred for this model since a hydrogen envelope is opaque to γ-rays. The supernova is a "failure" only in the sense that an outward going shock, that would normally expel the outer layers of the star in a supernova, does not develop. Instead, a $\sim 0.1-1$ $M_\odot$ accretion disk forms around a $\sim 5-10$ $M_\odot$ black hole. Viscosity in the accretion disk will transport mass and angular momentum radially outward while some fraction of the material moves inward. Neutrinos in the inward moving material will annihilate and produce a pair plasma which can emit the γ-rays in a broadly beamed jet along the rotation axis of the black hole. The advantage of this scenario is that the neutrinos are ejected into an area with low baryon density so that the γ-rays are not thermalized.

Yet another model involves collapse of a massive and rapidly spinning star, a process that can release 10^{54} ergs by tapping energy of Kerr black hole in a dirty (contaminated by baryons) fireball (Paczyński 1998a). This "hypernova" scenario envisioned by Paczyński (1998b) builds on the "failed" supernova model, but also invokes very high $\sim 10^{15}$ G magnetic fields to extract energy from the dense torus of material surrounding the Kerr hole. The idea is still fairly schematic due to difficulties in theoretically modeling such a rare event where relatively little is known about the progenitors. However, Paczyński (1998a) points out that the lifetime of O stars is of order 1 Myr, so that if GRBs are hypernovae, then they should be associated with star-forming regions (Paczyński 1998a). This is in direct contrast to the NS-NS merger models which predict binaries will be far from star-forming regions after attaining large space velocities from two supernovae.

Many other models exist, but far too many to cover here. The ones discussed here were chosen since, despite uncertainties concerning the method of generating γ-rays, as Woosley (1993) states, "If the signature of a 5 $M_\odot$ black hole accreting stellar masses of material in a minute is not a gamma-ray burst, what is it?"

1.4.2 Fireball physics

At this point, we turn to more generic models of GRB sources. Assuming a model can generate sufficient energy, how does it produce an observable GRB? This and the following section discuss the answer to that question schematically.

When models shifted GRBs from the galactic disk to a galactic corona or to cosmological distances, the total energy released in the GRB implied photon densities sufficient to create an optically thick pair plasma (Harding 1994), an idea which had earlier been proposed by Goodman (1986). This thermal fireball adiabatically expands until it becomes optically thin, at which time radiation may escape. The escape temperature T_{esc} is relatively independent of the input energy (Piran and Shemi 1993) and is roughly $T_{esc} \approx 20$ keV. However, an observer located infinitely far away sees the radiation blue-shifted by a factor Γ so that $T_{obs} \simeq \Gamma T_{esc} = T_0$ where T_0 is the initial temperature of the fireball (Paczyński 1986). Thus, the blue-shift exactly compensates for the decrease in temperature due to adiabatic expansion and an observer "sees" the event as if the fireball is not relativistically expanding. However, this would predict a very well thermalized spectrum, which is not what is observed (see §1.2.1), so the γ-rays must be produced by another process once the fireball becomes optically thin.

Estimates of the Lorentz factor Γ of the relativistic expansion can be made by estimating the temperature of the fireball. The initial temperature of a cosmological fireball is $T_0 \sim 10$ MeV, while for a galactic fireball, $T_0 \sim 10$ keV. Thus, for galactic models, $\Gamma \sim 10$ and for cosmological models $\Gamma \sim 10^2 - 10^4$ (Piran and Shemi 1993). Another estimate of the bulk Lorentz factor is found from the observation of γ-rays with energies in the GeV range in some GRBs. In order for high energy photons to not be degraded by a pair production cascade, the medium must be optically thin at the time of emission. The only way to achieve transparency to these rays in a cosmological burst is to invoke Lorentz factors $\Gamma \sim 10^2$ (e.g. Baring and Harding 1997, Fenimore, Epstein and Ho 1992, Fenimore 1993).

In order to produce a GRB out of a relativistic fireball, it is necessary to convert kinetic energy from the bulk flow into radiation. The currently favored models are those invoking shocks, either internal, in which faster portions of the flow catch up to slower portions (Rees and Mészáros 1992; Rees and Mészáros 1994; Paczyński and Xu 1994), or external, in which the bulk flow interacts with an external medium (Mészáros and Rees 1993). In an external shock model the typical duration of features within a GRB is set by one of two timescales: the duration of the interaction between the boundaries of the expanding shell and the external medium or the delay in arrival of photons from different emitting regions on the expanding shell. In an internal shock model, the time variability is directly related to variabilities in the injection of energy into the shock from a central engine (Mészáros 1998 and references therein). There are two main difficulties with the internal shock model. The first is that the energy release from the engine must be postulated to last for the duration of the entire burst, which can be as long as 10^3 s. It is difficult to produce such a timescale, especially in NS-NS merger models in which the timescale for coalescence is $\sim 10^{-3}$ s. The second difficulty is that internal shocks are relatively inefficient (Fenimore, Ramirez, and Sumner 1998). The main difficulty with the external shock models for producing the GRB event itself is that the temporal variability (e.g. GRB930310 in Figure 1.2) requires an "unreasonably large" number density for the inhomogeneities in the material which is swept up by the shock (Fenimore, Madras, and Nayakchin 1996; Sari and Piran 1997).

1.4.3 The afterglow

Rees and Mészáros (1992) introduced what is now referred to as the external shock model for GRBs. Although, as stated above, it is not clear if an external shock can produce some or all of the observed GRBs, there is a general agreement that this model is applicable to the afterglow—the fading GRB counterpart observed at lower frequencies—of a GRB. The basic idea of the afterglow models is that an ultra-relativistic shock wave entering regions of typical galactic densities can efficiently convert its bulk kinetic energy into radiation. As material is swept up, a shock wave propagates out into the external medium and a reflected shock propagates back into the expanding fireball. The bulk kinetic energy of the expanding fireball is released as either synchrotron or inverse-Compton radiation emitted by electrons in this shocked material. For an inhomogeneous fireball, the spectrum of emitted radiation softens with time and most of the radiation is emitted from the ultrarelativistic material in a few seconds. The luminosity from the fireball goes as

$$L \propto \Gamma_t^{-\alpha} t^{-1} \propto t^{(8+\alpha)/(2+\alpha)} \tag{1.3}$$

with $\alpha \sim 0.5$ (Rees and Mészáros 1992) as suggested by detailed relativistic hydrodynamics calculations (McKee and Colgate 1973).

If ultrarelativistic expansion is invoked in producing the GRB itself, this fireball must eventually interact with the medium surrounding the source. This is the main reason external shocks have been invoked in explaining the afterglow.

Paczyński and Rhoads (1993) build on the the external shock model and derive the expected radio emission from the expanding fireball as the synchrotron emission peak moves into the radio and the shell becomes optically thin to radio waves. Although there are large uncertainties in the distribution of energy between γ-rays, electric fields, and magnetic fields, they predict that roughly a week after a cosmological GRB, a ~ 1 mJy fireball should be seen in good agreement with the observations discussed in §1.3.3.

Considerable work has since gone into fireball afterglow models, (e.g. Waxman 1997, Mészáros and Rees 1997, Vietri 1997) and predicting the long wavelength emission from a GRB afterglow. For comparison to observations, the most important results are the spectral form of the afterglow and its evolution. The spectrum should follow the form:

$$f(\nu) = \begin{cases} S_0(\nu/\nu_b)^{-\alpha} & , \quad \nu > \nu_b \\ S_0(\nu/\nu_b)^{-\beta} & , \quad \nu < \nu_b, \end{cases} \tag{1.4}$$

where α depends on the assumed power-law distribution of electron energies which are producing the synchrotron emission, β depends somewhat on the low energy tail of electrons but should be $\sim 1/3$ and the break frequency, ν_b is given by:

$$\nu_b = 2 \times 10^{14} \left(\frac{1+z}{2}\right)^{1/2} (\xi_e/0.2)^2 (\xi_B/0.1)^{1/2} E_{52}^{1/2} t^{-3/2} \text{ Hz} \tag{1.5}$$

where ξ_e and ξ_B are ratios of the electric and magnetic fields to equipartition values respectively, E_{52} is the energy of the burst measured in units of 10^{52} ergs and t is the time since the burst (Waxman 1997). The power law decline in intensity is in good agreement with the observations of afterglows at optical and X-ray energies as discussed in §1.3.2 and §1.3.1.

1.5 Other transient γ-ray phenomena

Despite the successes of the afterglow models in predicting long term fading behavior of GRB afterglows, there is still considerable uncertainty as to what GRBs actually are. As suggested in §1.3.4, GRBs may not even be a single class of objects. Instead,

γ-ray emission may be a common signature of a variety of physical processes which involve acceleration in a relativistic shock. Future data should clarify this situation, as the wealth of data presently available has allowed several other phenomena to be disentangled from GRBs. It is worth briefly reviewing these other classes of events here to gain greater perspective on the problem of mixing multiple GRB source populations.

1.5.1 Terrestrial gamma-ray flashes

One surprising discovery to come from BATSE was that, about once a month, gamma-rays are observed from areas of thunderstorm activity on Earth. The events have spectra which peak around 1 MeV, last a few ms and have fluxes of $\sim 10^{-7}$erg/cm^2 (Fishman *et al.* 1994a). They are distinguishable from GRBs by their hard spectra and short duration, but one must be struck by the rough similarity in timescales, spectra and observed flux between GRBs and terrestrial gamma-ray flashes. The BATSE team also reported 3 similar events of slightly longer duration which could not definitely be said to come from the direction of Earth (Fishman *et al.* 1994a). Given that one cannot positively distinguish between even a small number of bursts from the Earth and GRBs without good position information, one has to doubt it is really possible to separate different classes of GRBs reliably at this point.

1.5.2 Soft gamma-ray repeaters

A class of soft gamma-ray (or hard X-ray) transient sources known as soft gamma repeaters (SGRs) was separated from the "classical" GRBs in the 1980s (Mazets and Golenetskii 1981, Atteia *et al.* 1987, Laros *et al.* 1987 and references therein). These bursts are remarkably uniform both in regard to time profiles, $\sim$ 100 ms with no structure, and spectra, consistent with thermal bremsstrahlung at a temperature of $\sim$ 30 keV (Norris *et al.* 1991). This uniformity is in marked contrast to the diversity seen in GRBs. As their name implies, SGRs also repeat, something that has never been observed in classical GRBs.

Since SGRs repeat it is possible to find their positions more accurately than is possible with most GRBs, making associations with objects at other energies possible. There are four known SGRs: 0526$-$66, 1806$-$20, 1900+14 and 1627$-$41. In each case, the error box of the SGR contains a supernova remnant (Cline *et al.* 1982; Kulkarni and Frail 1993; Murakami *et al.* 1994; Kouveliotou *et al.* 1994; Vasisht *et al.* 1994;

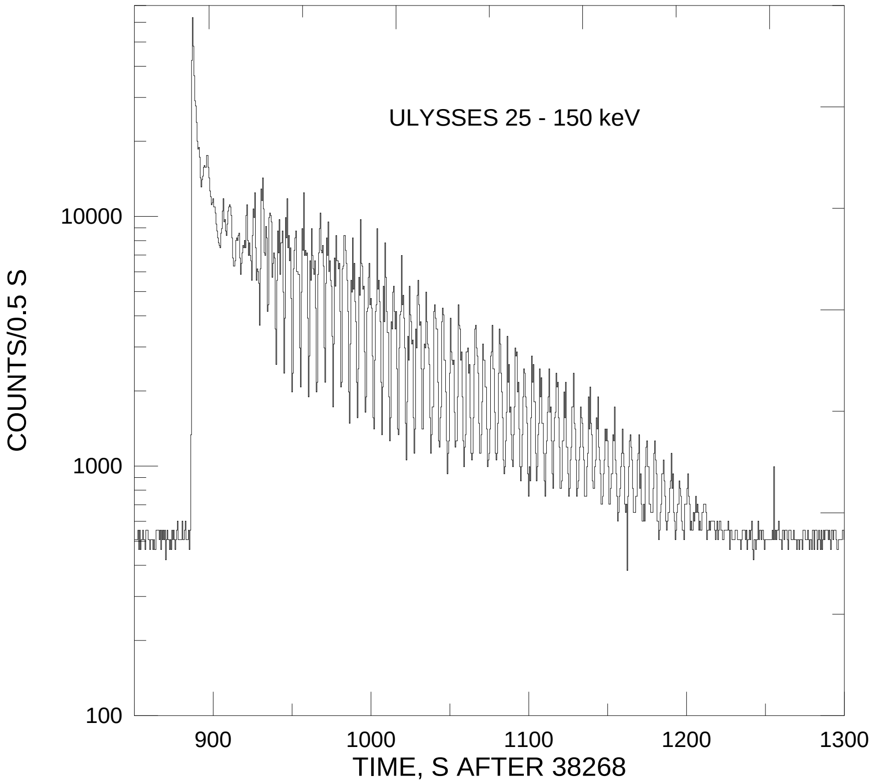

Figure 1.9: The Ulysses lightcurve for the August 27, 1998 event from SGR 1900+14 (Hurley *et al.* 1998). The pulsar's spin period of 5.15 s modulates the observed intensity during the interval $\sim 920 - 1210$ s.

Hurley *et al.* 1996; Kouveliotou *et al.* 1998; Woods *et al.* 1998).

If one accepts that the SGRs are associated with the supernova remnants that they are positionally coincident with on the sky, the three well-studied SGRs, 1806−20, 0525−66 and 1900+14 have distances of 15, 55 and 7 kpc (Hurley 1996; Corbel *et al.* 1997). Thus the distance scale to SGRs is firmly galactic. However, SGRs were only recognized as a separate class of objects little more than a decade ago, eight years after the first one was discovered. The situation is further complicated since SGRs can also emit a more GRB-like type of burst, which is the subject of the following section.

Superbursts

On March 5, 1979, SGR 0525−66 emitted the "super" burst, with a very bright initial peak ($\sim 1.5 \times 10^{-3}$ erg sec^{-1} cm^{-2}) originally thought to peak at low energies.

However, deadtime effects—inefficiencies in a γ-ray detector caused by the inability of detector electronics to respond to a large incident flux—were not properly considered for this bright burst and Fenimore, Klebesadel and Laros (1996) argue that it is, in fact, consistent with the range of classical GRBs. This burst is still classified as an SGR, however, because after the main burst, weak and soft 8-s period pulsations were seen for 200 seconds. If the burst had been weaker, these pulsations would not have been seen and the initial spike would have been classified as a GRB. The Pioneer Venus Orbiter, which observed the March 5th event, could not have detected such comparably weak pulsations in any other GRBs that it detected (Crider and Fenimore 1996).

A similar burst was detected on August 27, 1998, presumably from SGR 1900+14. The burst had an intensity "comparable to a strong γ-ray burst" and exhibited pulsations with a period of 5.15 ± 0.02 s (Cline, Mazets, and Golenetskii 1998). It was observed above 100 keV by instruments on the *SAX* satellite, with an initially hard spectrum which suddenly softened and then progressively hardened (Feroci *et al.* 1998b). A lightcurve from the Ulysses satellite is shown in Figure 1.9 (Hurley *et al.* 1998). If the burst had been ~ 40 times weaker, only the first ~ 15 s would have been detectable by Ulysses making it appear more like a classical GRB.

If SGRs can produce GRB-like bursts, are some classical GRBs produced by weak SGRs which are too faint to be observed in their normal bursting state? If so, this would be yet another class of events currently "polluting" the mix of GRBs.

1.5.3 Solar flares

Solar flares are another background for the BATSE detectors. Solar flares are identified by their locations near the Sun, their generally soft spectra and their coincidence with solar X-ray events detected by other satellites (Fishman *et al.* 1994b). Solar flare events are relatively long, lasting tens to hundreds of seconds, so they can only be confused with long, soft gamma-ray bursts. Nevertheless, position information is important in distinguishing between solar flares and GRBs, which implies that, despite their very different origins, solar flares and some GRBs appear similar when observed from Earth.

1.5.4 GRB980425: a unique afterglow

Using the wide field cameras aboard the *SAX* satellite, GRB980425 was localized to an $8'$ error radius and the position was released within a day of the discovery (Soffitta *et al.* 1998). This rapid localization allowed rapid optical followup observations which detected a supernovae, SN1998bw, in a spiral galaxy (ESO 184-G82) within the error box (Galama *et al.* 1998a; Galama *et al.* 1998b). The supernova brightened from R = 15.7 to R = 15.0 in the first three days and peaked at R = 13.6 two weeks after the GRB (Galama *et al.* 1998b). The redshift of the galaxy was measured using H-α emission to be $z = 0.0085 \pm 0.0002$ (Tinney *et al.* 1998). The lack of He I lines caused the SN1998bw to be classified as a Type Ic, although, even under this classification, it has unique characteristics (Pata and Piemonte 1998). A ~ 10 mJy radio source, coincident with the supernova position, was detected three days after the burst and brightened to ~ 50 mJy 4 days after the GRB (Kulkarni *et al.* 1998b). A steady X-ray source was also detected coincident with the supernova position (Piro *et al.* 1998). In order to explain the radio brightness and lack of X-ray emission, relativistic expansion of the stellar ejecta was invoked (Kulkarni *et al.* 1998a). Relativistic outflow of matter is invoked in most models of GRBs, making the connection between at least some supernovae and some GRBs seem appealing. Thus, we may have come full circle in that a connection between at least one supernovae and one GRB appears to have been made (Woosley, Eastman, and Schmidt 1998), a possibility first suggested by Colgate thirty years ago.

1.5.5 A cautionary tale

Terrestrial gamma-ray flashes are short and come from the direction of Earth. Solar flares are long and have soft spectra and come from the solar direction. Soft gamma repeaters have soft, non-evolving spectra, repeat and are likely associated with filled supernova remnants. However, the March 5, 1979 and August 27, 1998 events could have looked like classical GRBs if they had been weaker. GRB980425 appears to be associated with a Type Ic supernova in a nearby galaxy and GRB971214 came from a galaxy at a redshift of 3.4, implying the release of $\sim 10^{53}$ ergs of energy. Thus, we have several widely disparate physical processes which yield similar fluxes of gamma-rays when observed from near Earth orbit. It may very well be that the objects which we call GRBs are, in fact, several different classes of objects which we have yet to distinguish as such. Since distinguishing characteristics are likely to be found at other than γ-ray energies, it is critically important that unbiased searches for counterparts be conducted. At this point, counterpart observations of any single GRB are insufficient to make generalizations about GRBs as a class.

1.6 Prompt radio emission from GRBs

In contrast to the GRB counterpart observations discussed in §1.3, this thesis describes an effort to detect low-frequency radio emission nearly simultaneous with the GRB itself. To distinguish such radiation from the afterglows discussed above, it is referred to as *prompt* emission. Currently, only limits exist on the spectrum of GRBs below ~ 1 keV at the time of the GRB itself. It is not known how far the power-law spectrum shown in Figure 1.3 continues below γ-rays. Does the spectrum turn up or down at lower energies? Does the power law continue indefinitely? Answering these questions could provide clues about the origin of GRBs.

In the following sections two basic arguments are developed to motivate the experiment described here. The chapter ends with a discussion of historical experiments which set limits on prompt radio emission from GRBs and the latest group of experiments aimed at detecting prompt radio emission.

1.6.1 Looking for dispersion

One of the great advantages to working in the low-frequency radio is that dispersion caused by the interstellar medium delays radio emission relative to higher frequency radiation. Since GRBs are a transient phenomenon, this time delay can allow a radio telescope to point toward a GRB position *prior* to when the radio emission reaches Earth.

The amount of delay a radio wave experiences is quantified by the dispersion measure, DM, which is defined as the column density of free electrons along the line of sight or $\mathrm{DM} \equiv \int_0^L n_e(z)dz$ (see Appendix A for details). Pulsars have been used to model the density of free electrons n_e in the galaxy. The maximum DM looking through the galactic plane is ~ 1400 pc cm^{-3}, while the minimum looking out the pole is ~ 20 pc cm^{-3} (Taylor and Cordes 1993). The dispersion due to the inter-galactic plasma along the line of site is (Palmer 1993)

$$\mathrm{DM}_{\mathrm{IGP}} \approx 2.64 \times 10^4 \Omega_{\mathrm{IGP}} \frac{h}{q_0}[(1+2q_0 z)^{1/2} - 1] \ \mathrm{pc\ cm}^{-3} \tag{1.6}$$

where $\Omega_{\rm IGP}$ is the amount of ionized plasma in the intergalactic medium in units of the closure density, q_0 is the cosmological acceleration parameter, and the Hubble constant is parameterized by $h = H_0/(100\ \mathrm{km\ s^{-1}\ Mpc^{-1}})$. For $\Omega_{\rm IGP} = 0.03$, $h = 0.75$, $q_0 = 0.5$, and $z \ll 1$, $\mathrm{DM}_{\rm IGP} \approx 600 \times z$ (Palmer 1993).

In principle, the delay caused by dispersion could be used to provide a rough distance estimate to a GRB from the transient itself rather than relying on a redshift of an afterglow or a host galaxy. With an independent estimate of the distance, the dispersion measure can be used to probe the average electron density along a line of sight. Motivated by this property of radio waves, Ginzburg (1973) suggested the idea of measuring the density of the intergalactic plasma using GRBs, "unusual" supernovae or any other distant source capable of producing radio bursts.

1.6.2 Scaling arguments

The second argument for searching for GRB counterparts in the radio is that relativistic electrons responsible for γ-ray emission can also produce coherent radio emission. This happens in environments such as active galactic nuclei, the Sun, pulsars and even terrestrial thunderstorms. To provide a reasonable flux density for which a radio search should aim, one would, in principle, calculate the expected coherent radio emission for many GRB models. However, very few models for GRBs include definite predictions for the expected radio flux from a GRB. An alternative to the difficult task of predicting radio flux densities from models is to estimate them by analogy with other systems observed at both radio and γ-ray energies, which is the procedure followed here.

In each of the examples to follow, the observed ratio of radio flux density to γ-ray flux is calculated and scaled to the flux of a typical GRB, roughly 10^{-7} erg cm^{-2} s^{-1}. Since the detection of a transient signal in the radio depends on its fluence, the expected flux density will be calculated as if it were a constant intensity source that emitted in the radio for 10 s.

The first estimate is based on pulsars since they are neutron stars, which are involved in a majority of the models for GRBs (Nemiroff 1994). The radio flux density values are taken from Taylor, Manchester and Lyne (1993) and scaled to 74 MHz, relevant to the experiment in this thesis, using a spectral index of -1.5. The γ-ray fluxes are taken from Table 3 in Ramanamurthy *et al.* (1995). If GRBs have similar radio flux density to γ-ray flux ratios, they could be detected in the range of $\sim 10 - 10^4$ Jy for a 10 s burst.

Solar flare activity is another phenomenon which generates both gamma ray and coherent radio emission. Hard solar X-ray bursts which often occur in association with Type III radio bursts can give another estimate of a reasonable radio flux density for GRBs. By analogy with the data found in Kane (1972), GRBs with flare-like X-ray or γ-ray to radio luminosity ratios would be found with radio flux densities in the range $\sim 10^4 - 10^7$ Jy for a 10 s burst.

A third process which can be used to generate a flux density estimate is high altitude terrestrial lightning. Brief γ-ray (Fishman *et al.* 1994a) and broadband radio (Holden, Munson, and Devenport 1995; Massey and Holden 1995) transients have both been associated with thunderstorms. If these phenomena arise from the same events, then we can scale to GRB fluxes by comparing the brightest gamma-ray flashes to the brightest radio transients. The brightest gamma-ray flux of terrestrial flashes, $\sim 10^{-6}$ erg cm^{-2} s^{-1}, (Fishman *et al.* 1994a) is comparable to the flux from a typical GRB. Using a bright transient found in (Massey and Holden 1995), suggests a GRB could be accompanied by a burst detected as a 10^3 Jy source in a 10 s integration.

These three estimates presented here are simplistic and the environments in which GRBs are generated are likely to be very different from any of the cases used here. The point is that these *observed* phenomena give us a rough idea of what a relevant sensitivity for a prompt radio counterpart search may be.

1.6.3 Previous work

Several experiments have previously attempted to detect *prompt* radio emission from GRBs. Due to the poor localization of GRBs on the sky, radio telescopes with large beams are most appropriate. This section will summarize the efforts made on this aspect of the GRB problem.

In 1976, the detection of an apparently astronomical radio transient at 4 frequencies (spanning the range 151 MHz to 408 MHz) from a near solar, but non-solar, direction occurred within 1 minute of a GRB (Mandolesi *et al.* 1977). However, balloon observations of the bright, 10^{-4} ergs cm^{-2}, GRB put its position $\sim 50°$ away, inconsistent with a common origin for the radio and γ-ray transients (Sommer and Müller 1978). Nevertheless, this radio event may have been astronomical in nature.

Using several geographically separated stations, Baird *et al.* (1975), searched for radio pulses from 1 hour before to 10 hours after ~ 20 GRBs. Their search failed to locate any astronomical radio pulses other than those with a solar origin down to a limiting flux density of 10^5 Jy.

Using systems at 151 MHz and 408 MHz, Inzani *et al.* (1982) determined that for 80% of GRBs the emitted radio flux density was $< 10^4$ Jy. However, for 20% of the 65 GRBs analyzed, there was a weak excess of radio bursts *prior* to the GRB event at a flux density of $> 10^4$ Jy. Unfortunately, it was impossible to rule out terrestrial interference as the source of the observed events.

The limiting flux densities reached by these searches was $10^4 - 10^5$ Jy and terrestrial radio frequency interference (RFI) could not be ruled out. Given the estimates for GRB radio flux densities in §1.6.2 along with the somewhat weak limits reached by the older experiments discussed here the time had come for a new round of experiments.

1.6.4 Contemporaneous work

The experiment described in this thesis was one of four contemporaneous radio searches for GRB counterparts. Each experiment had its strengths and weaknesses which will now be discussed.

The Survey for Transient Astronomical Radio Emission (STARE) project, based at MIT, used geographically separated total-power radiometers with roughly full-sky coverage to search for transient astronomical signals at 611 MHz (Katz 1997; Katz *et al.* 1996). Monitoring of 108 GRBs produced a number of inter-site coincidences but the number obtained was consistent with that expected due to random chance (Katz *et al.* 1998). In general, the limits on transient radio emission that STARE produces are ~ 10 kJy or poorer. STARE's main strengths are the use of geographically isolated sites to reduce RFI events, a nearly full sky beam to make triggering on GRB events unnecessary and a large sample of observed GRBs. Its major weaknesses are its relatively poor sensitivity and the inability to remove random RFI coincidences at different sites.

In another recent experiment, the Cambridge Low-Frequency Synthesis Telescope (CLFST) was used to search for rapid counterparts to GRBs at 151 MHz. The CLFST was configured into 7 beams, each with a $\sim 10°$ field of view, so that, allowing for slewing of the telescopes, 10 % of sky was visible within 1.5 minutes. By comparing several beams, terrestrial interference could be removed (astronomical transients should only occur in a single beam). Another guard against terrestrial interference was provided by using the visibility phase as a function of baseline to look for patterns related to the array geometry (Green *et al.* 1996).

The CLFST put limits at the 200 Jy level from 1-6 hour after GRB940301. Actually, the noise level in the data is much better, but terrestrial interference cannot be ruled out as the cause of less intense spikes. For this same burst, images were made 1, 2, 7, 16 and 36 days after event, and no new sources were found at the 80 mJy level (Koranyi *et al.* 1995).

Two other bursts, GRB950430 and GRB 950706, were also observed by CLFST, down to limits of $\sim 10-100$ Jy (Green *et al.* 1996). It is somewhat difficult to know how to interpret their results as only pulses within the 1σ γ-ray error box are analyzed (Green *et al.* 1996). Unfortunately, data on only three GRBs were published and the CLFST experiment has stopped due to lack of funds. The obvious strengths of the CLFST are its good sensitivity and large beam areas. However, in order to push for greater sensitivity, the experiment gave up one check against terrestrial RFI by moving all 7 beams to the same location once a GRB trigger was received. In addition, of the three bursts observed, only one could really be called a *prompt* observation in that the GRB was in one beam before the trigger was received. Unfortunately, the diversity of GRBs and the small number sampled by the CLFST makes it difficult to assess the significance of the null result for GRBs *in general*.

One other recent effort of note used a 7 m parabolic antenna with a 40 MHz - 1000 MHz sweeping receiver with 1 MHz spectral resolution and sweep time of 0.25 seconds (Benz and Paesold 1998). The antenna reached a sensitivity of $\sim 10^5$ Jy for 7 bursts within 10° of the solar direction and within ± 2 minutes of the GRBs. Although the sensitivity was low, the spectral coverage made this an interesting experiment.

1.6.5 Fallbrook low-frequency immediate response telescope

The topic of this thesis is a dedicated search for prompt radio emission from GRBs. The Fallbrook Low-frequency Immediate Response Telescope (FLIRT) was designed to respond rapidly, within ~ 10 s of a GRB, and point a sensitive radio array at the position of the GRB. The FLIRT array operates at 74 MHz, where the dispersion delay expected is four times as long as at the CLFST's frequency of 151 MHz. The heart of the FLIRT experiment was a 4-channel spectrometer which was capable of the direct measurement of the dispersion of any astronomical transient. The use of dispersion as a discriminator against terrestrial RFI was an efficient way to eliminate terrestrial signals.

The remainder of this thesis discusses FLIRT in depth. In Chapter 2 the instrument design and calibration are discussed. Chapter 3 describes the method used to search for dispersed transients. Finally, Chapter 4 presents two interesting candidate events and provides a list of limits on radio emission associated with GRBs.

Chapter 2

FLIRT instrument and calibration*

2.1 Experimental design

There are two basic constraints when designing a GRB counterpart search. First, and most importantly, GRB positions are generally only known to an accuracy of a few degrees, so large and/or multiple beams are required. Second, GRBs are usually brief and do not repeat, so that a rapid response is required if one wants to detect emission related to the GRB itself and not to its delayed afterglow.

The approach taken in this experiment is to use a low-frequency, phased radio array. This has several advantages. First, beam widths in the radio are naturally large, especially at the low frequency, 74 MHz, used here. Second, electronically steered phased arrays can be pointed in much less than a second which significantly shortens the delay time over a mechanically steered dish. Third, dispersion in the interstellar medium delays radio signals relative to their high frequency (e.g. γ-ray or optical) counterparts and the delay goes as ν^{-2}, making very low frequencies attractive.

In order to advance the experiment as quickly as possible, it was advantageous to find an existing radio array. The University of California, San Diego (UCSD) radio array in Fallbrook, California (Coles, Frehlich, and Kojima 1994) was available when Professor Stephen Thorsett first investigated possible sites for the experiment. The full array has a geometric area of ~ 8000 m^2 with a half-power beam width of 1.75° (N-S) by 3.5° (E-W) and was designed in a manner which made division into 8 subarrays with $7° \times 7°$ beams straightforward. The array is located on the Fallbrook Naval Weapons Depot, adjacent to the Marine base Camp Pendleton, in Southern

*Some material from this chapter is published in Balsano *et al.* (1996) and Balsano *et al.* (1998).

California. The land is leased quite cheaply ($500/yr), which made it affordable on the limited budget allowed for this experiment. However, it is located roughly 1-2 kilometers from the nearest electrical outlets and telephone pole, which greatly limited the equipment that could be used. The array was last used in early 1990 for a study of refractive scintillation in pulsars (Gupta, Rickett, and Coles 1993), so that by 1992, it had degraded considerably. Nevertheless, it was available and Professors William Coles and Barney Rickett at UCSD were able to assist in upgrading the array for this experiment.

In §2.2, a brief overview of the experimental setup is discussed with more detail given in §2.2.1-2.2.7. The calibration of the array is discussed in §2.3.

2.2 Experimental setup

A block diagram of the Fallbrook Low-frequency Immediate Response Telescope (FLIRT) instrumentation is shown in Figure 2.1. FLIRT is triggered by the reception of GRB coordinates ~ 5 s after a GRB is detected by BATSE. The coordinates of a GRB are sent to a workstation at UCSD that relays them over a dedicated phone line to a laptop computer at the Fallbrook radio array. The laptop sends out phasing and gain control commands to each of the array elements.

At the array, the 74 MHz radio frequency (RF) signal from each antenna element is amplified by an adjustable amount, delayed for proper phasing (pointing), then summed with 15 other antenna elements. This signal is amplified in two more stages and then mixed down to an intermediate frequency (IF) of 10.7 MHz. The IF signal reaches a spectrometer where it is filtered into four frequency channels and sampled several times during each DOS clock cycle (18.2 Hz). Data is later retrieved over a dedicated phone line whenever necessary.

In the following sections, all stages of this brief overview are treated in greater depth. The description will follow the data from the source of GRB coordinates all the way to a detected radio signal, elaborating on details as necessary.

2.2.1 BACODINE/GCN

The GRB Coordinate Network (GCN) is a system which provides rapid coordinate dissemination for GRB and other transient events. It was formerly known as the BATSE COordinate DIstribution NEtwork (BACODINE) before its GRB data sources were

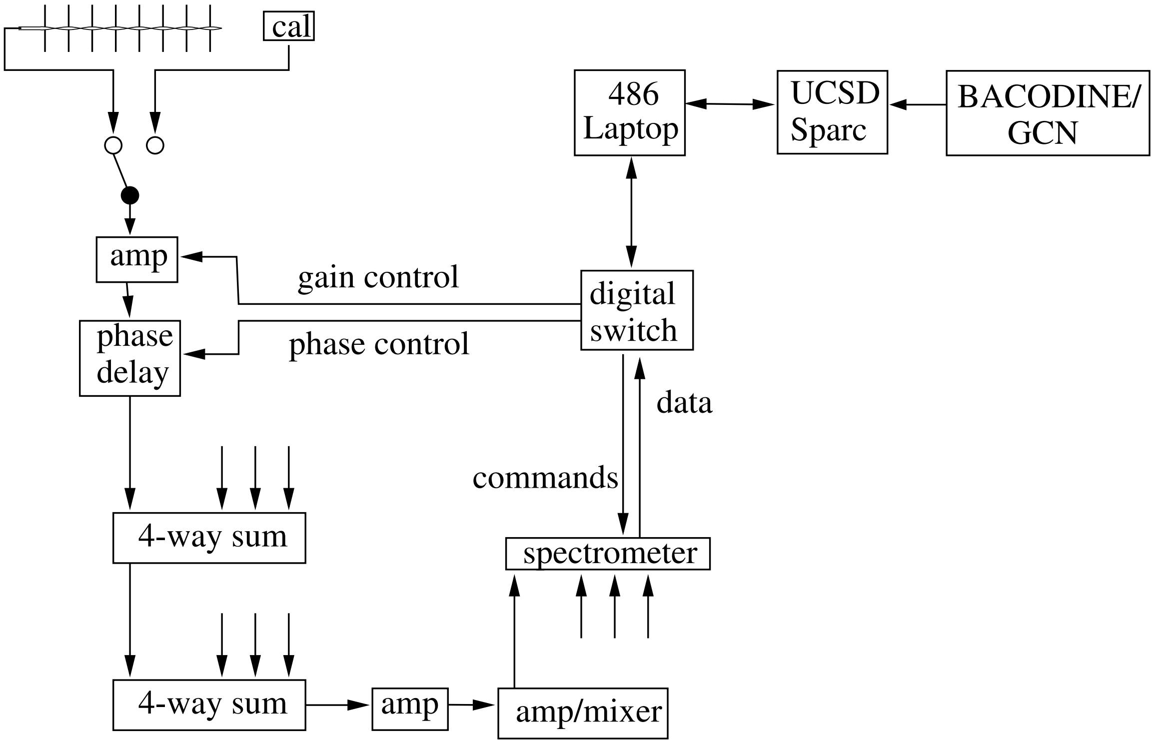

Figure 2.1: Block diagram of the FLIRT experiment. The data and signal flow are detailed in the text. A group of three arrows appearing without a source next to a longer arrow with a source represents a total of four identical copies of the source.

expanded beyond BATSE locations[†]. The telemetry from BATSE is relayed via TDRS satellites to Goddard Space Flight Center in 2 second chunks with a delay of 2 seconds. Thus, by the time data gets to Goddard, it is $2-4$ seconds old. GCN calculates a position for the GRB based on this initial data in ~ 0.1 s. After calculating coordinates, GCN sends notices over Internet sockets to sites wishing to do followup observations. A more complete description of the BACODINE/GCN system is available elsewhere (Barthelmy *et al.* 1996; Barthelmy 1998).

To understand how coordinates are generated from BATSE data by GCN, it is necessary to give a brief overview of the BATSE instrument. BATSE consists of eight, uncollimated NaI scintillator large-area detectors (LADs) positioned on the corners of the *CGRO* satellite, each sensitive to sources in one hemisphere. A BATSE detector cannot produce a position independently. However, ignoring all systematic

[†]FLIRT only used the BACODINE portion of the GCN

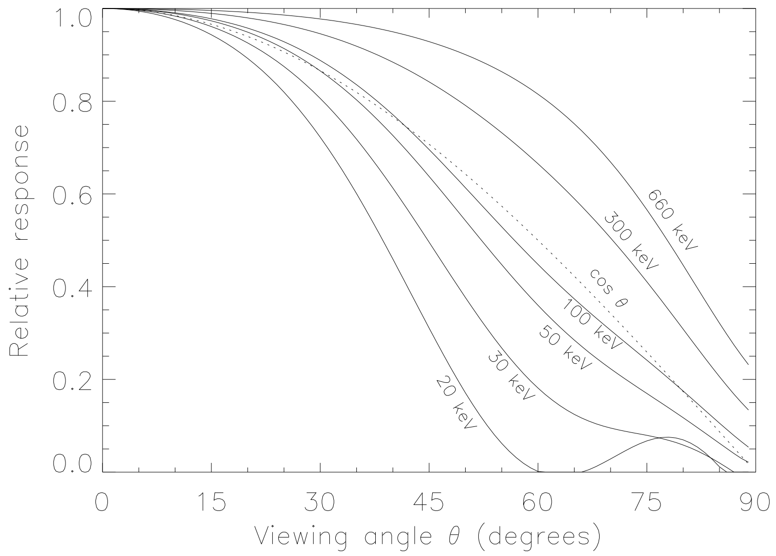

Figure 2.2: The angular response function for the BATSE large area detectors (Figure from Chakrabarty 1996). The low energy response is poor at large angles due to increased pathlength in the absorbing Al shielding on the detectors. The high energy response is flatter than $\cos\theta$ for small θ due to the thickness of the crystal being comparable to the high energy photon attenuation length which gives photons arriving at large angles greater chance of being absorbed in the NaI crystal (Chakrabarty 1996).

effects, the observed intensity in a detector scales as the projected area of the detector visible to a source, which in turn scales as $\cos\theta$ with θ the angle from the detector normal. By observing a source with three or more detectors, it is possible to derive a position and intensity for the source. There are two main systematic effects which cause the observed signal to deviate from the ideal. First, the BATSE detectors are known to have significant energy-dependent deviations in their angular response as seen in Figure 2.2. Second, γ-ray photons can be scattered into the detector from the Earth's atmosphere. Both of these effects are accounted for in the final GRB positions produced by the LOCBURST algorithm (Pendleton, Briggs, and Meegan 1996) used by the BATSE team. GCN, however, computes the coordinates of a GRB using ideal $\cos\theta$ responses for the detectors‡. Given that GCN ignores the non-ideal

‡Positions calculated with the BATSE LOCBURST algorithm were available for some bursts, but with a delay of $\sim 15-30$ min and were not used in this experiment

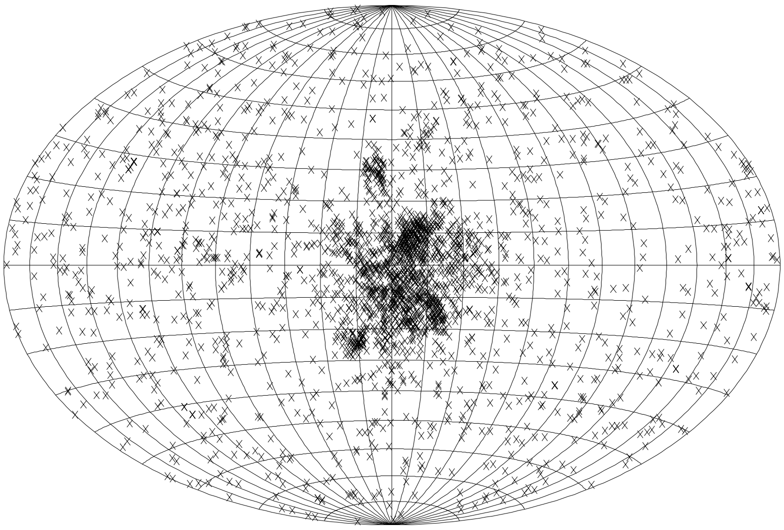

Figure 2.3: All GCN triggers received by FLIRT in galactic coordinates. The triggers from the GRO burster $1744-28$ are clearly seen in the center of the plot.

response of the detectors and Earth scattering, it is not surprising that the "typical worst case" error circle is $\sim 20°$ in diameter (Barthelmy *et al.* 1998).

To investigate the systematic errors in the GCN positions for GRBs, it is useful to look at a plot of all of the trigger positions sent via GCN to FLIRT as shown in Figure 2.3. The distribution appears random and uniform except for the noticeable cluster around the galactic center. An expanded view of the central region is shown in Figure 2.4. Most of these triggers are due to the GRO burster $1744-28$, an accreting X-ray binary neutron star (Kouveliotou *et al.* 1996b). These bursts are soft compared to GRBs, so that the systematic errors of $\sim 10-30°$ are larger than would be expected for GRBs (cf. Figure 2.2). Looking at the distribution of GCN positions for $1744-28$ shows that the statistical errors are $\sim 10°$, which is comparable to what is found for weaker GRBs.

To quantify these systematic errors for the set of FLIRT observations, the angular offsets between GCN and final LOCBURST positions are shown in Figure 2.5. Out of 150 burst notices, ~ 135 moved more than $3°$ and ~ 85 moved more than $7°$. The FLIRT beam is $7°$ in diameter at the 3 dB points (see §2.3.1), so the final sensitivity of FLIRT to most GCN triggered bursts is quite low (see Table 4.2). Nevertheless, GCN is the only source of GRB coordinates available on minute or shorter timescales.

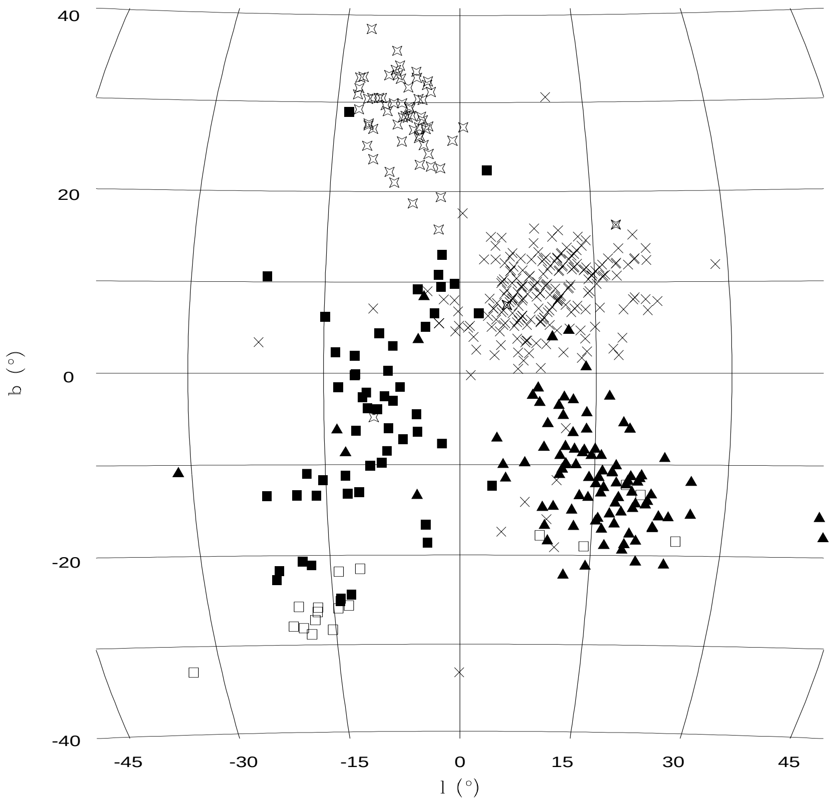

Figure 2.4: GCN triggers near the position of GRO1744-28, $(l, b) = (0.4°, -0.3°)$. A different symbol is used for each pointing of the *GRO* satellite during the period covered by this plot. The positions for bursts from GRO1744 − 28 found by GCN cluster with a statistical uncertainty of $\sim 10°$ for a given pointing of *CGRO*, but the systematic effects with pointing of the satellite are $\sim 10 - 30°$.

Dealing with the positional uncertainties inherent in such a system is one of the major challenges in doing GRB counterpart searches.

2.2.2 Communications

Initially, the connection between UCSD and the FLIRT array was done via a cellular modem. There were several disadvantages to this approach:

- cellular connection delays were often as long as several minutes,

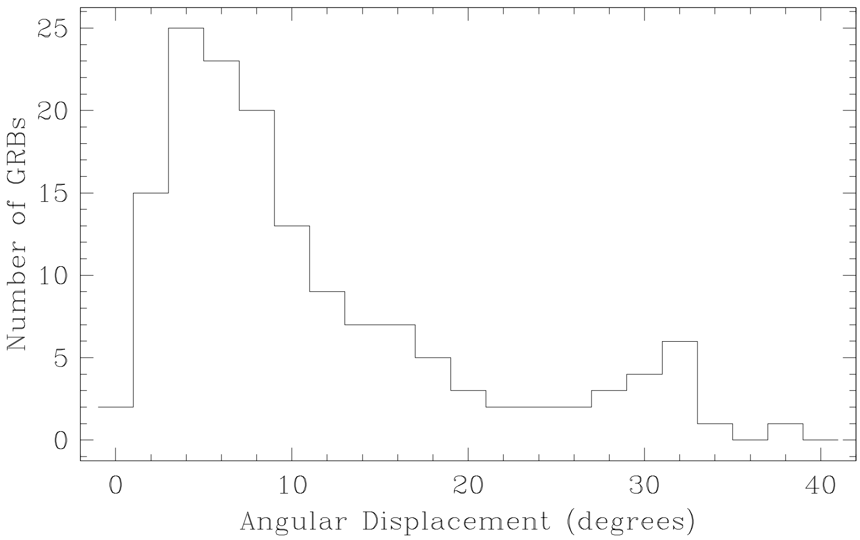

Figure 2.5: Separation between GCN and LOCBURST position for 150 GRB triggers received by FLIRT. All triggers are plotted except for 4 outliers at 50°, 57°, 64° and 143°.

- the modem connection was often lost and had to be re-established, sometimes causing the laptop computer to reboot during an observation,
- the modem reached only 2400 baud at best, and
- doing any substantial interaction with the site easily led to monthly cellular bills of \$200 – \$300.

Due to these problems, in May of 1996, two phone lines were installed by Bill Coles and the author to improve remote access to the array. Approximately 400 m of twisted pair phone line was installed in UV-resistant PVC irrigation piping[§]. The connection was made between a telephone pole on nearby privately owned land and the remote telescope control shed on Navy land. The wire was pulled through the PVC by hand with difficulty so it had to be spliced in two locations near tight bends. The spliced sections were brought together in water resistant meter boxes.

[§] Burying the line in a trench would have been a better method but doing so would have forced an environmental impact review due to concerns over endangered ground squirrels in the area.

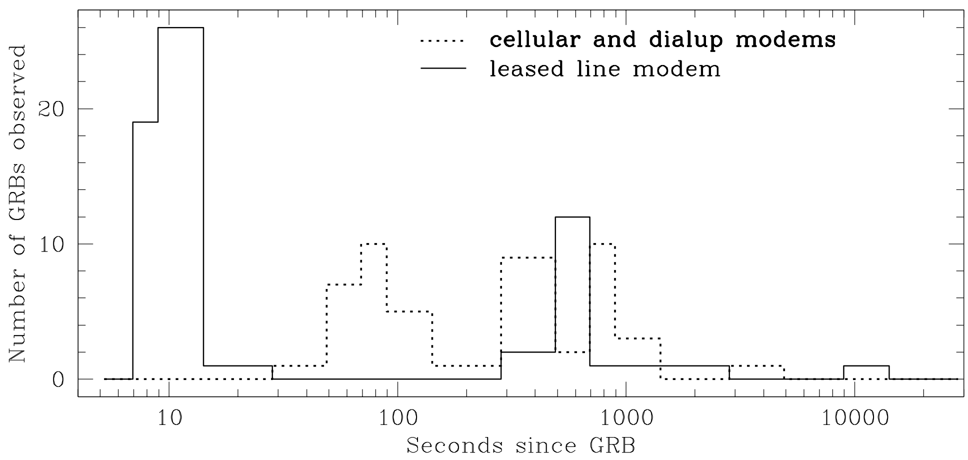

Figure 2.6: Histogram of FLIRT response times for 113 GRBs, defined as the delay between detection of a GRB event by BATSE and the first data records from FLIRT. The dashed and solid lines are histograms for before and after, respectively, the leased line was installed. The peaks at several hundred seconds are due to delayed GRB event notification by GCN during *CGRO* telemetry gaps.

In July of 1996, one of the installed phone lines was converted to a dedicated analog circuit (a “leased” line). The connection time delays went from $\sim 1-3$ min with the cellular modem, to ~ 40 s with the dialup line to ~ 2 s with the dedicated line. The rapid connection time allowed FLIRT to be on source within 10 s of the start of a GRB. In addition, a standard modem could be used over the phone line so that transfer rates up to 14 kbaud were achieved, greatly simplifying remote operation and testing.

The dedicated leased line enabled FLIRT to be one of the quickest GRB followup studies, *at any wavelength*. The response times for the duration of the experiment are shown in Figure 2.6.

One consequence of laying approximately 400 m of phone line above ground was increased susceptibility to power surges. During the 2 years following the installation, one modem was damaged beyond repair and two phone line surge suppressors were burned out, presumably as a result of lightning discharges near the array causing ground currents to couple to the phone lines. Nevertheless, the land line added significant functionality to the system.

The connection between GCN and the FLIRT site was maintained by a workstation at UCSD which monitored incoming data on a dedicated Internet socket. Burst notices within 60° of the array normal triggered a script to activate the leased line connection and start an observing program on the site laptop.

2.2.3 Array description

In order to understand the FLIRT experiment performance, it is necessary to have a better understanding of the array itself. This section gives a closer look at the FLIRT array.

The array is composed of 128, $4\lambda \times 1\lambda$ (EW × NS) elements arranged in a grid 4 elements in the EW direction and 32 elements in the NS direction for an overall size of $16\lambda \times 32\lambda$. The array is subdivided into 8 sections, each of which is 2 elements in the EW direction and 8 elements in the NS direction for a $8\lambda \times 8\lambda$ subarray (see Figure 2.7). The idea was to use each subrarray, with a $\sim 3.5°$ half-power radius beam, independently to have 8 beams tiling the BACODINE error box.

The primary element is composed of 8 linear, full-wavelength dipoles, put on $\lambda/2$ spacing. The dipoles are connected to transmission lines which are twisted such that adjacent dipoles are phase-reversed and each dipole is driving the transmission line at an anti-node (see Figure 2.7). The array and its construction are described in Coles *et al.* (1994) . The method used to point a phased array is described in Appendix B.

In its original form, the array was operated as a single unit. However, the array was arranged in the 8 sections mentioned above. For this experiment, instead of summing the 8 subarrays, each was treated as a separate entity. BNC cables were brought from the eastern half of the array (4 subarrays) to the control shed early in the experiment. Use of the western 4 subarrays was given lower priority; it would have required digging a trench for more cables, fixing antenna drive electronics for the 4 subarrays and manufacturing more mixer units. Instead, attention was focused on the 4 eastern subarrays.

Of the eastern subarrays, only one provided a useful signal. Of the remaining subarrays, one had insufficient gain to detect sky signals and the other two had filters in place which either attenuated the sky signal to unobservable levels or interfered with the phasing algorithm outlined in §2.3.2. The one working subarray had an effective area of 650 m^2¶, the equivalent of a 29 m diameter reflector.

¶In principle, it would be ~ 1000 m^2 but 4 of 16 elements were not working.

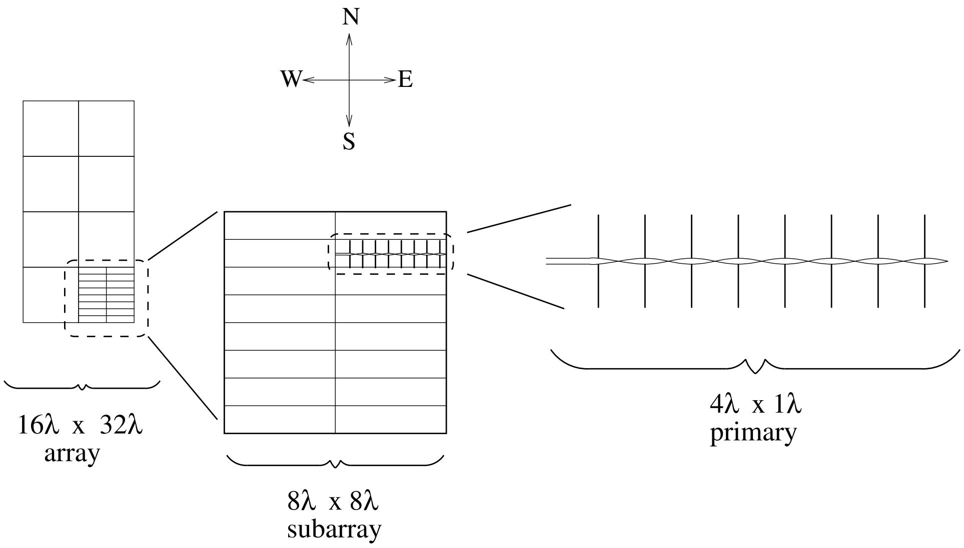

Figure 2.7: The FLIRT array schematic. In the lefthand figure each box represents one of the 8 subarrays. In the center figure each box represents one of the 16 elements within a single subarray. The righthand figure shows 8 dipoles arranged with $\lambda/2$ spacing to form a primary element.

2.2.4 RF section

The input radio signal was fed into a large circuit board where phasing and initial amplification were done. A diode switch controlled whether sky signal or a calibration signal[‖] was fed into the circuit. The initial amplification was ~ 15 dB and was digitally adjustable. After the signal was amplified, a series of diode switches controlled the signal flow to allow adjustable phasing. A section of digital logic controlled 7[**] bits used in phasing, each bit controlled a diode switch which allowed the signal to follow either a direct or a delay path, with delays of $\frac{1}{2}\lambda, \frac{1}{4}\lambda, \ldots, \frac{1}{128}\lambda$ available.

Each primary element was fed into 1 of 4 channels on a circuit board. Each subarray had four such circuit boards housed in a buried enclosed rack. After the signals were amplified and delayed properly, each set of 4 from a large circuit board was summed. The 4 resulting signals for a subarray were added and fed into a second amplifier with a gain of ~ 15 dB. The signal was connected by coaxial cable to the control shed, where it was fed into the amplifier/mixer stage. The amplifier within the

‖The power to the calibration source could not be remotely controlled, which limited use of the source to visits to the Fallbrook site.

**The 8th bit was used to control the sky/cal switch.

mixer was identical to the secondary amplifier; built on top of this was a mixer stage which mixes the 74 MHz signal down to 10.7 MHz and provides another ~ 40 dB of gain. The mixers were designed by Barney Rickett at UCSD and built by the author.

One of the difficulties with the mixers was that they were run near their saturation levels so that strong, out-of-band interference was sufficient to drive the inband signal level down. In addition, the local oscillator in the mixer consisted of a tuned LC circuit with an adjustable capacitor. The adjustable capacitors have temperature coefficients $\sim 0.1\%/^{\circ}$C so that the drift of the LO could be several hundred kHz during a typical day. In practice, however, no data exist to quantify the effects of this drift, which is not important for out experimental results.

2.2.5 IF section

Once the signal from a subarray was mixed down to 10.7 MHz, it was fed into the spectrometer board. The spectrometer was designed by Bill Coles and built by Michael Liu at UCSD. The spectrometer was a very simple design consisting of an amplification stage, 4 LC filters, diode detection and an op-amp amplifier. The spectrometer was built with 8 subarrays in mind, so that with 4 frequencies per subarray, a total of 32 IF signals were available. These signals are fed into 4 MUX chips and digital logic was designed to select the channel of interest. A single AD chip was used to convert the analog voltages from the IF signals into a digital voltage to be read in the laptop PC parallel port. Since there is only a single AD chip, all the channels are sampled sequentially. Typically, each of 16 used channels was sampled ~ 10 times during a MS-DOS clock interrupt, so each of the 16 working channels was sampled at a rate of ~ 200 Hz with an integration time of 0.3 ms per sample.

The bandpasses for each of the subarrays are shown in Figure 2.8. The individual channel bandwidths are nearly 1 MHz at their 3 dB points. The displayed bandpasses were measured in the lab using a swept signal centered on ~ 20 MHz and mixed up to 74 MHz. To simulate the array as closely as possible, the signal was injected into a phasing circuit board and underwent the same stages of amplification as a signal would undergo under normal operations. The only portion of the signal path not replicated in the lab was the antenna itself and its feedline. However, another set of measurements made using a crude dipole antenna manufactured in the lab confirm that the passband shape is largely unaffected by the antenna itself. The difference in passbands with and without the dipole was largest at the edges of the passband where it was at most 5% of the peak value. To a good approximation then, the response

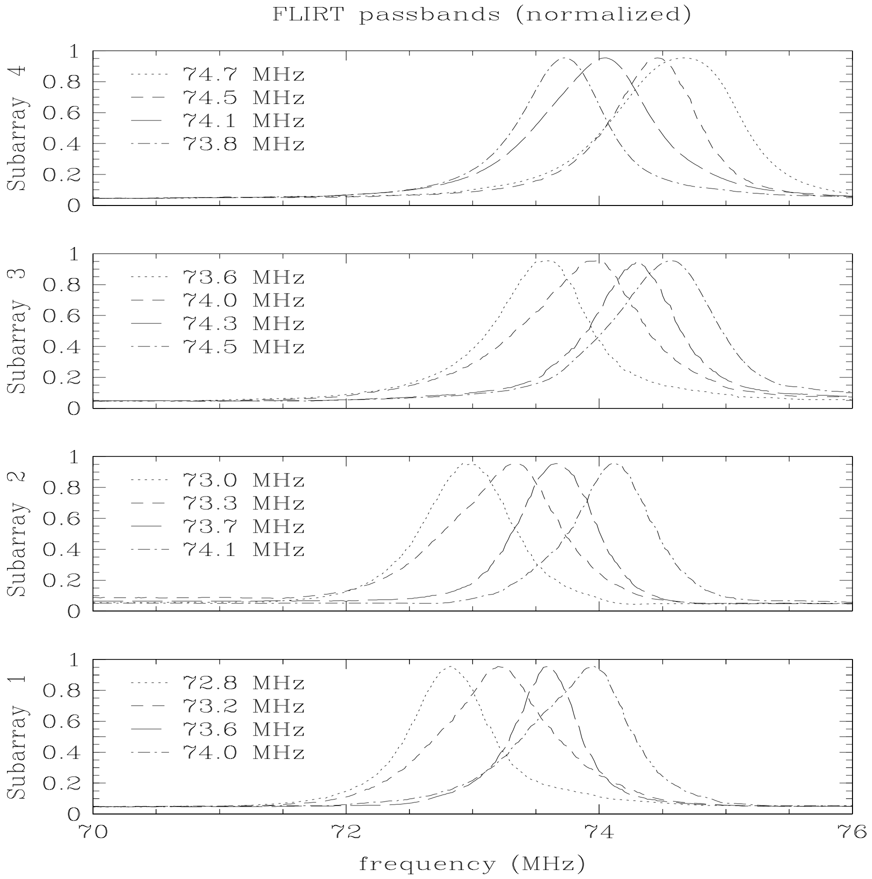

Figure 2.8: The bandpasses for each subarray, normalized at their maximum response. The fourth subarray channels were inadvertently tuned backwards relative to the other subarrays.

of the antenna across the bandwidth of the spectrometer channels can be considered flat, and ignored.

2.2.6 Drive computer

The most important consideration in purchasing a computer for FLIRT was low power consumption and the ability to run off a DC power supply (such as a car battery). An Epson ActionNote 4SLC2-50 laptop was purchased and performed adequately for several years, although on two occasions major repairs had to be made to the power system in the laptop. The experiment was finally ended in April of 1998 when a chip on the laptop computer shorted out and the computer was deemed irreparable.

The computer's main functions were to distribute gain and phase commands to the array and to read in spectrometer data. Since both the array control and spectrometer were designed to use the parallel port, a digital switch was designed to switch between these operations. The final version of the switch was built by Jason Rhodes.

Having a computer at the site simplified testing and retrieval of data. A standard software package, pcAnywhere, was used to allow remote control of the computer. A session on the laptop could be commanded from the workstation at UCSD and displayed remotely at Princeton. Various test and observation programs were compiled on the laptop and data could be downloaded as necessary.

2.2.7 Power

The Fallbrook site is run entirely off solar power, which poses severe constraints on both test and observing equipment. A total of 10 solar panels provides a maximum of 15 Amp charging current during full sunlight. The normal discharge current was 2.1 Amp at 24 Volt, for a total power consumption of 50 W. During some site visits, a gas-powered generator was used to power routine analysis equipment (e.g. a spectrum analyzer, oscilloscope and frequency counter). However, most electronic equipment did not run well with such a "noisy" power source, making field testing quite challenging.

The solar panels were connected to a charging unit that charged eight, 6 V batteries. In theory, the batteries have sufficient capacity to provide for FLIRT operations for a week without solar power. In practice, however, inclement weather caused the experiment to shut down on numerous occasions, presumably due to nearby lightning strikes. A set of circuit breakers provided some protection from current surges during thunderstorms, but a site visit was required to reset them.

2.3 Calibration

Although precise absolute flux calibration of the FLIRT array was not critical, two basic calibrations needed to be performed. If one used ideal electronics, pointing a phased array telescope would be a simple matter of computing the appropriate phase delays (see Appendix B) for each element in the array and then commanding these delays. However, delays inherent in the different electronics used for each element need to be calibrated out before pointing can be achieved. Furthermore, the observed voltages from the spectrometer need to be converted to physically meaningful units with at least modest precision.

In order to perform both phase and gain calibrations, it is necessary to have a good understanding of the antenna beam pattern, which is covered in section 2.3.1. Using this beam model, the phasing and gain calibration are detailed in sections 2.3.2 and 2.3.3 respectively.

2.3.1 Beam patterns

The beam pattern of a radio telescope is the gain profile on the sky over which the antenna is sensitive to radiation. By the reciprocity theorem, this pattern is equivalent to the far field radiation pattern of the same antenna when transmitting. The normalized far field power pattern, P_n, can be expressed as:

$$P_n(l,m) = \frac{P(l,m)}{P_{\max}} = \frac{\left|\vec{E}\cdot\vec{E}^*\right|}{\left|\vec{E}\cdot\vec{E}^*\right|_{\max}} \tag{2.1}$$

where $\vec{E}$ is the far field electric field and $P(l,m)$ is the power pattern as a function of direction cosines l and m.

The electric field is proportional to the Fourier transform of the current distribution within the array:

$$f(l,m) = \int_{-\infty}^{\infty}\int_{-\infty}^{\infty} g(x,y)e^{-2\pi i(lx+my)}\,dx\,dy \tag{2.2}$$

where $g(x,y)$ is the current distribution of the array, l and m are the direction cosines in the x and y directions respectively and x and y are measured in wavelengths λ. (See Kraus 1986 or Rohlfs and Wilson 1996 for more details on the theory and Christiansen and Hogbom 1987 for a good discussion of calculating beam patterns in practice.) Normalizing equation 2.1 produces:

$$P_n(l,m) = \frac{|f(l,m)|^2}{|f_{\max}|^2} \tag{2.3}$$

The theoretical beam pattern for an array is calculated in steps. The pattern due to the full array is computed assuming each primary element is an isotropic radiator (or receiver), and this pattern is multiplied by the pattern for the primary element. For FLIRT, the array is a 2×8 grid of primary elements and each primary element is an array of 8 dipole antennas. Therefore, the first step in the process is to calculate the beam pattern due to a dipole antenna.

The current distribution for a center-fed dipole oriented along the y-axis is well modeled as:

$$g(x, y) = \sin(2\pi|y|)\delta(x), \tag{2.4}$$

since the current at both ends of each half-wave must be zero. Taking the Fourier transform of Equation 2.4, one obtains the field pattern in the y direction:

$$f(m) = \frac{1 + \cos(m\pi)}{2(1 - m^2)}. \tag{2.5}$$

For a linear array of 8 ideal isotropic radiators on $\lambda/2$ spacing in the x-direction, the current distribution is:

$$g(x) = \sum_{\alpha=0}^{7} \delta(x - \alpha/2 + 7/4) \tag{2.6}$$

with $\delta(x)$ the Dirac delta function. Taking the Fourier transform of 2.6 and multiplying by 2.5 yields the primary pattern:

$$f(l, m) = \frac{1}{16} \frac{1 + \cos(m\pi)}{1 - m^2} \frac{\sin(4\pi l)}{\sin(\pi l/2)} \tag{2.7}$$

In equation 2.7, l and m are defined with respect to the array normal. However, the Fallbrook array itself is tilted such that the north end is at a slightly higher elevation than the south end by an amount $0.0413 \times \lambda$ per dipole. In addition, the dipoles are not quite full wavelength, but are $0.9084 \times \lambda$ in length. These modify equation 2.7, producing:

$$f_{primary}(l, m) = \frac{1}{16} \frac{1 + \cos(m' \times \pi)}{1 - m'^2} \frac{\sin(4\pi l)}{\sin(\pi l/2)} \tag{2.8}$$

with

$$m' = 0.99897 \times m + 0.04517 \times n \tag{2.9}$$

where n is the direction cosine in the z direction. The primary pattern is plotted in Figure 2.9[††].

[††]In proceeding from Equation 2.4 to Equation 2.5, the integration is still carried out over two half sine waves, and only the tilt of the array matters for calculating m'

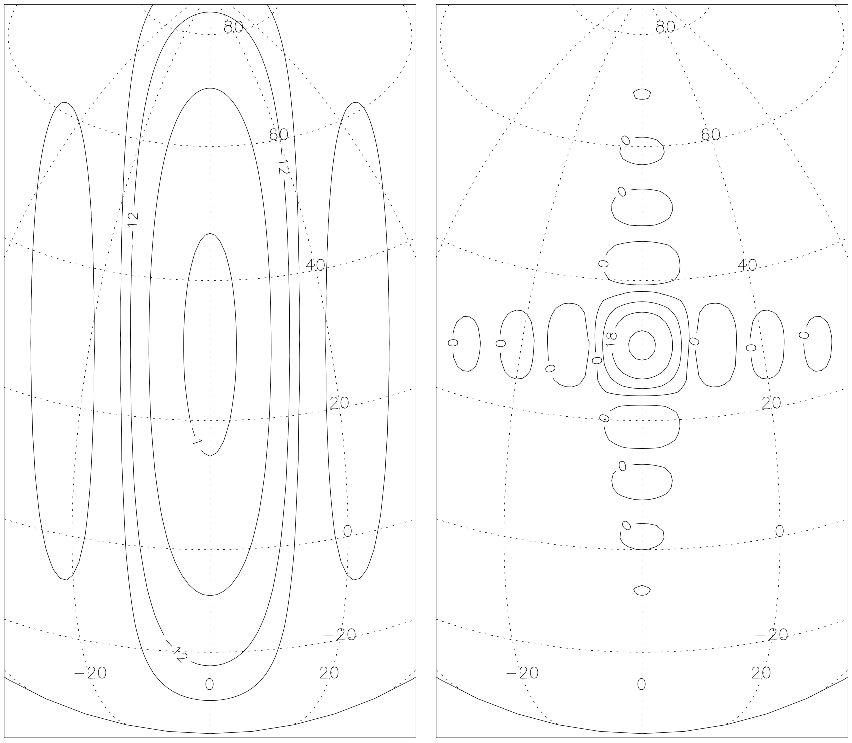

Figure 2.9: FLIRT normalized primary beam pattern (left) with contours plotted at 18, 12, 6 and 1 dB down from the maximum of 0 dB—only -12 and -1 dB are labelled. A FLIRT subarray beam pattern (right) with contours 24, 12, 6 and 1 dB down from the maximum ($\sim$ 24 dB (i.e. on the same scale as the primary element); the beam is pointed at the local zenith.

A subarray consists of 16 elements arranged in a 2×8 grid. The element spacing is $4 \times \lambda$ in the x direction and $0.9084 \times \lambda$ in the y direction, giving a $8\lambda \times 7.3\lambda$ array. The current distribution for this configuration is:

$$g(x,y) = \sum_{\beta=0}^{1} \sum_{\gamma=0}^{7} \delta(x - 4\beta + 2)\delta(y - 0.9084 \times \gamma + 7/20.4542)e^{2\pi i\phi} \tag{2.10}$$

where $\phi = l_0 x + m_0 y + n_0 z$ is the commanded electronic phase delay. The voltage is given by:

$$f_{array}(l, m') = \sum_{\beta=0}^{1} \sum_{\gamma=0}^{7} e^{2\pi i[\phi - l(4\beta-2) - m'(0.9084\times\gamma - 7/20.4542)]} \tag{2.11}$$

with m replaced by m' given by equation 2.9. If the sums are carried out, equation 2.11 becomes:

$$f_{array}(l, m') = 2\cos(4\pi(l - l_0))\frac{\sin(8\pi \times 0.9084 \times (m' - m'_0))}{\sin(\pi \times 0.9084 \times (m' - m'_0))} \qquad (2.12)$$

The advantage of leaving f_{array} in the form given in 2.11 is that primary elements in a given subarray may have different gains, including 0 (see below in §2.3.3), which can be accounted for by inserting coefficients in front of each exponential in the sum.

The total power observed at a given point is then:

$$P(l, m) = [f_{array}(l, m') \times f_{primary}(l, m')]^2 \qquad (2.13)$$

This beam pattern is also shown in Figure 2.9.

2.3.2 Phase calibration

Initially, phase calibration of the array was attempted using a line source at 73.8 MHz. The signal from this "cal" was distributed out to the array over 8 lines, one for each subarray electronics enclosure. The signal was distributed to each of the 16 channels on the phasing circuit boards described in section 2.2.4. Using this cal source, each of the elements in a subarray was phased with respect to a reference element by incrementing the commanded phase of the tested element and sampling the resulting antenna power. The power pattern is simply a sine wave, with the maximum power attained when the two elements were in phase. In addition to phasing the elements, general problems with the digital or RF circuitry could be diagnosed by looking at the phasing signal. This process only took a few minutes but was only performed during site visits since the cal source drew too much power to be left on indefinitely.

Unfortunately, the calibration scheme just described calibrates the entire signal path except for the coaxial cable from the antenna elements to the RF circuit boards. At first it was thought that this would be not be a serious problem. To correct this problem in earlier uses of the array, a time domain reflectometer was used to measure the phase delays along each coax cable. However, this was not done for the FLIRT experiment, so a scheme for remotely phasing the array had to be used.

There are a two bright sources of radio waves which can act as calibration sources, Cassiopeia A and Cygnus A, with 74 MHz flux densities of 15 ± 1 kJy[‡‡] and 17 ± 1 kJy respectively (Baars *et al.* 1977).

[‡‡]The flux density of Cas A decreases $\sim 1\%$/yr, the value given is for 1997.

Sky sources can be used as phase calibrators in a relatively simple scheme. As already mentioned in §2.2.4, each primary element has a phase adjustment with 128 (2^7) possible values. If the power in a channel is sampled at each possible phase setting for the element in question, the maximum in power is achieved when the element is properly phased relative to a reference element. This is the procedure used with the calibration signal. With a sky signal, however, using this signal directly is complicated by variable baselines due to RFI and sources slowly drifting through the beam. A clean way around this is to difference the power found at all pairs of phase settings that are 180° apart. In practice, this was performed with the most significant phase bit being switched on and off every sample while the least significant phase bit was incremented every other sample.

More formally, if we have for the voltage at the reference element:

$$V_r(t) = V_r \cos(2\pi t_i/T) \tag{2.14}$$

and for the element to be phased:

$$V_p(t) = V_p \cos(2\pi t_i/T + \phi(t)) \tag{2.15}$$

where V_r and V_p are amplitudes, T is the period of the 74 MHz signal, and ϕ is the sum of the instrumental phase offset and the commanded offset.

The power observed in a sample is proportional to the sum of these voltages squared and averaged over the sample interval. Since $T \sim 10$ ns and the integration time is $\tau \sim 0.3$ ms, all complete cycle cosine terms drop out and the power is:

$$P \propto V_r^2 + V_p^2 + 2V_rV_p \cos(2\pi\phi_k) \tag{2.16}$$

with ϕ_k the phase delay for the kth time sample.

With the phasing scheme outlined above, the phase delay can be written as:

$$\phi_k = \phi_0 + \frac{k \text{ div } 2 + 64(k \bmod 2)}{128} \tag{2.17}$$

where ϕ_0 is the phase error to be removed, div is integer division, and mod is the modulus operation. The signal we are interested in is the difference between consecutive pairs of signals, $S = P_{2k} - P_{2k+1}$, which, with Eq. 2.16 and Eq. 2.17 becomes:

$$S_k \propto V_rV_p \cos(2\pi(\phi_0 + k/128)) \tag{2.18}$$

The element is properly phased with k such that the argument to the cosine is 0.

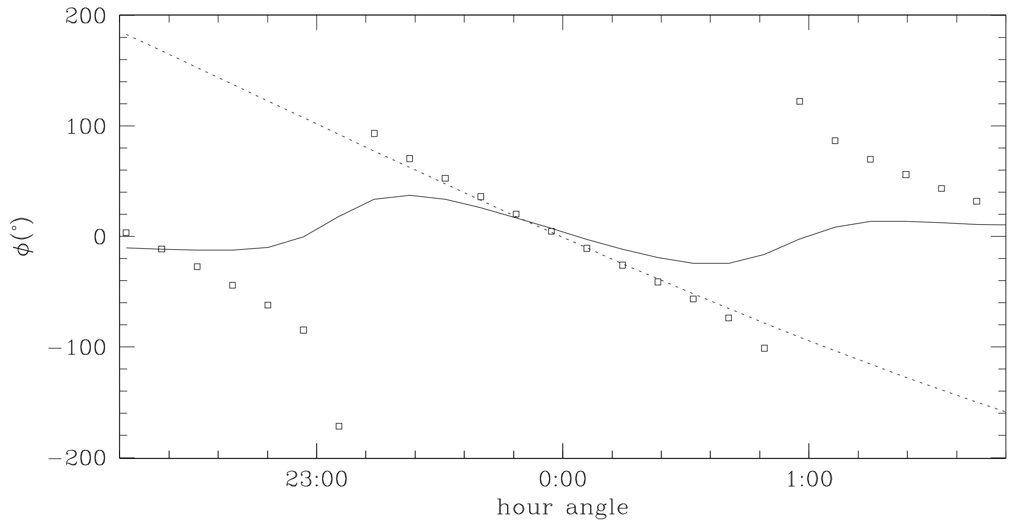

Figure 2.10: The expected phasing signal for a bright source drifting overhead. The array is pointed at the source declination and phasing is performed as in the text. The solid line is the curve generated for a simulation using a full sky map and the theoretical beam pattern. The points were generated using the beam pattern and a point source. The dotted line is the pointing offset, $\vec{k} \cdot \vec{x}$.

It was not obvious that this strategy would work starting with a randomly phased array, so simulations were done to understand how best to proceed. Since the array was randomly phased, it was easiest to let Cas A drift overhead and calculate the phase delay as a function of hour angle. Initially, it was thought that the measured phase delay for a point source drifting through the beam would be predicted by $\vec{k} \cdot \vec{x}$ where $\vec{k}$ is the source wave vector and $\vec{x}$ is the position vector of the array element. This is not at all the case, as can be seen in Figure 2.10, where a simulation of phasing is plotted using a full sky map as well as a map containing a single point source. The FLIRT beam is large enough that full account must be taken of the sky illuminating the beam in order to accurately predict the shape of the phase delay curve. Since no good maps of the sky at 74 MHz exist, a better method had to be developed. One thing that is apparent from Figure 2.10 is that the measured phase delay at null hour angle, HA $= 0$, is the same for the different models and thus might be a reasonable way to determine the phase delay.

To investigate a better method based on this idea, the simplest case to treat is

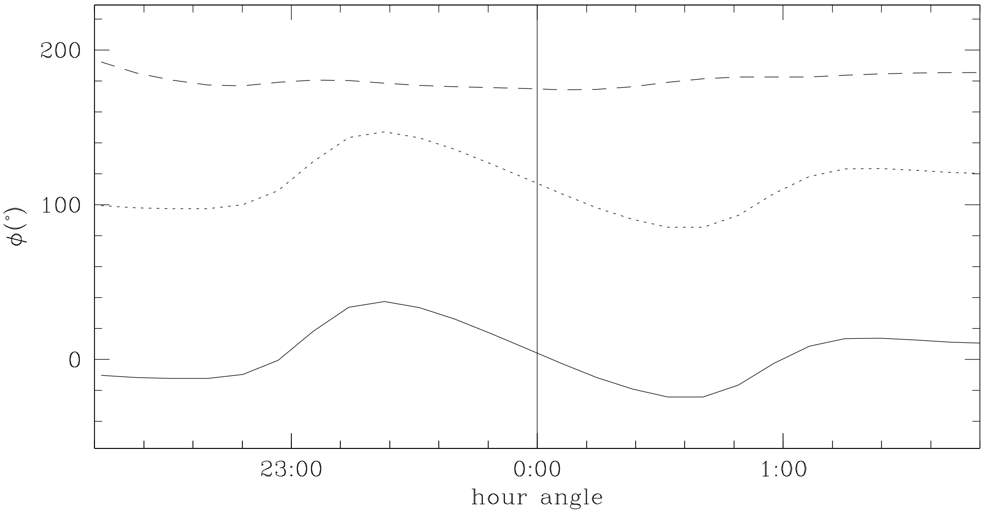

Figure 2.11: Simulated phasing offsets as a function of hour angle. The solid line gives the expected phase delay when the array is perfectly phased. The dotted line gives the expected phase delay when only the element being phased has a non-zero phase delay; the entire curve is shifted by the input phase delay. The dashed line is the calculated phase delay for random offsets assigned to each element with the same offset applied to the element in question; the curve no longer resembles the simple case and the phase offset at 0 hour angle is not directly related to the input phase delay.

that of a single element improperly phased with respect to the rest of a properly phased subarray. The measured phase delay drifts linearly while the source is in the main beam of the primary pattern (HA $\sim \pm 7^\circ$ to the nulls) and the instrumental phase delay shifts the entire phase delay curve as seen in Figure 2.11. Also plotted is a simulation run with all elements in the subarray assigned random phases. In this case, no simple relation exists between the new curve and the original phase delay curve.

Still, a practical guess for phasing when the entire subarray is unphased is the phase offset for HA $= 0$. Simulations were performed to check this concept. Starting with phases randomly chosen from 0 to 2π for all elements, the simulated phasing program was run. Estimated phase offsets at null hour angle were subtracted from the original, incorrect, phases and the process iterated. As can be seen in Figure 2.12,

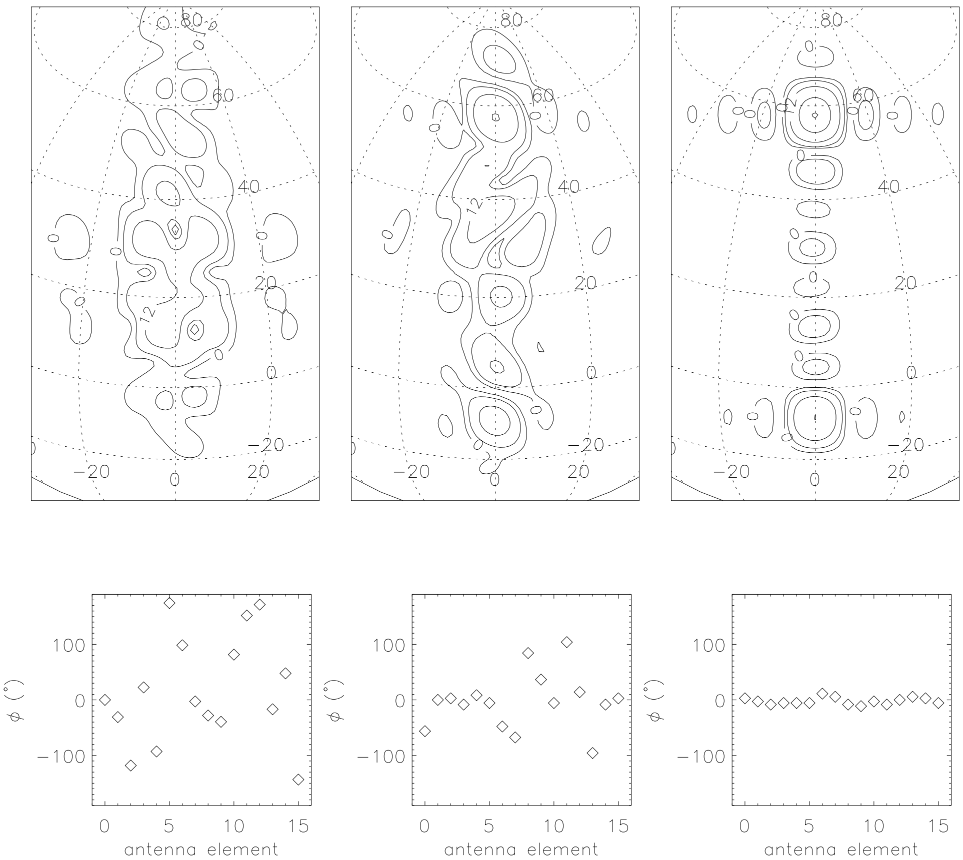

Figure 2.12: Top panels show beam model with phase offsets shown in the bottom panels. The far left is a randomly phased configuration while two iterations of setting the phase offsets as described in the text are shown in the middle and right figures. Contours are drawn at 24, 18, 12, 6, 3 and 1 dB from the maximum possible for a phased subarray.

this process brings a subarray from a completely unphased to phased state in a few iterations.

In practice, the method works reasonable well, but RFI complicated matters somewhat. When a significant RFI source is present, the phasing algorithm will determine a phase that is, at best, contaminated by the RFI source, and at worst, the phase delay for the RFI. Data from a fairly typical phasing scan made on Cas A are plotted in Figure 2.13. The data offset to higher values are caused by an intermittent strong

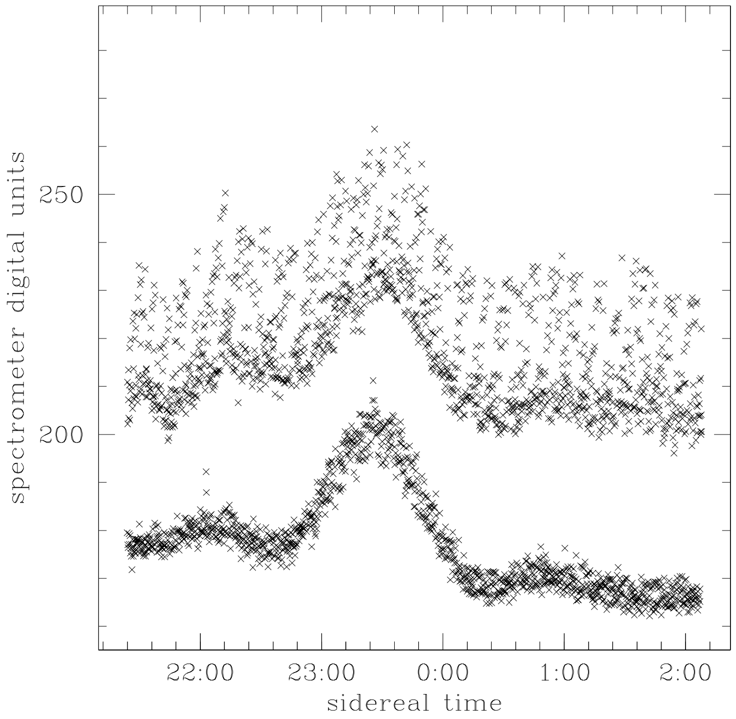

Figure 2.13: A full phasing run on Cas A with the low frequency channel shown; every 50th point is shown to avoid clutter. This channel has particularly bad interference caused by a narrow band transmitter just outside the protected radio band. Distinguishing between points contaminated by RFI is trivial in this case.

RFI source.

To eliminate RFI contamination, code was developed to find jumps in the data. It uses a simplistic box-car averaging scheme and monitors the means of two adjacent sections of data. When the means become discrepant, a jump is tagged. The data sections are then sorted and a threshold is applied to separate good from bad data. In practice the routine needed minimal hand processing to determine the thresholds and was otherwise automated. A close-up of a different phasing scan with good and bad points tagged is shown in Figure 2.14.

Once a phasing scan is taken, the data are processed at Princeton and phase delay curves are plotted. In Figure 2.15, a typical single element scan is shown. All four frequency channels give essentially the same result (within ± 2 phase bits) once the RFI source has been removed. The narrow-band nature of the source is also apparent

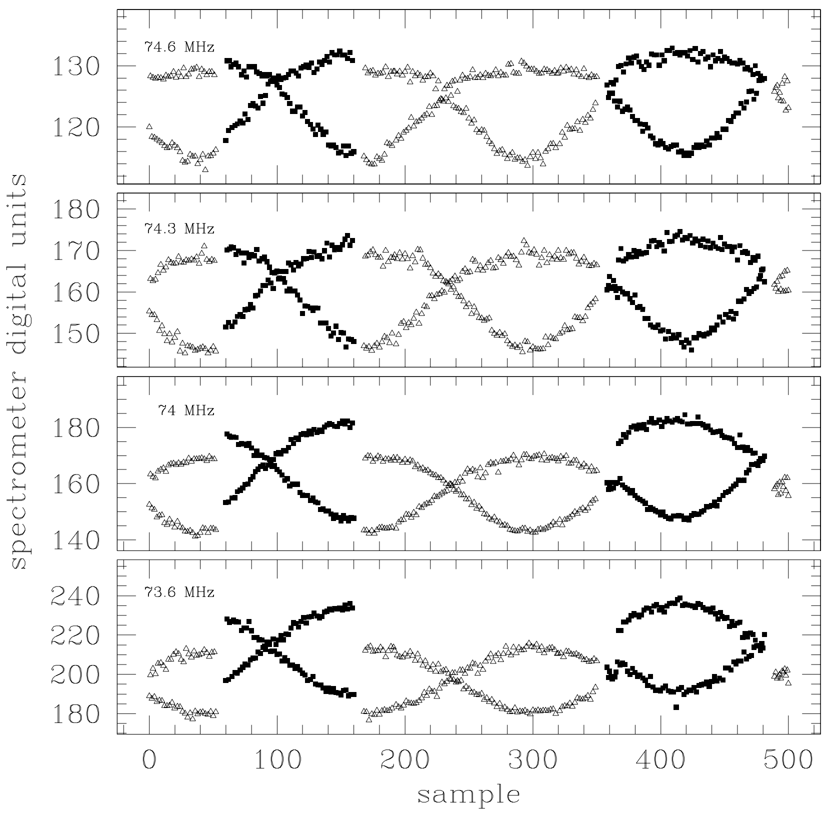

Figure 2.14: A phasing run on Cas A; all values are sampled raw voltages and data from only 30 seconds are shown. The data plotted with open triangles are good data and the filled squares show RFI contaminated data. The low frequency data are used to flag all channels as bad when the interfering signal is active. The algorithm for separating out data with RFI is robust even when contaminated points are only modestly affected.

in the lack of an effect in the two high frequency channels.

This algorithm worked satisfactorily on only 1 of the 4 subarrays for reasons stated in §2.2.3. However, the change in sensitivity to Cas A for the one phased subarray can be seen in Figure 2.16. Initially, Cas A was only marginally detected and there was no difference between "pointing" at or away from Cas A. Once the array was phased, pointing was easily demonstrated.

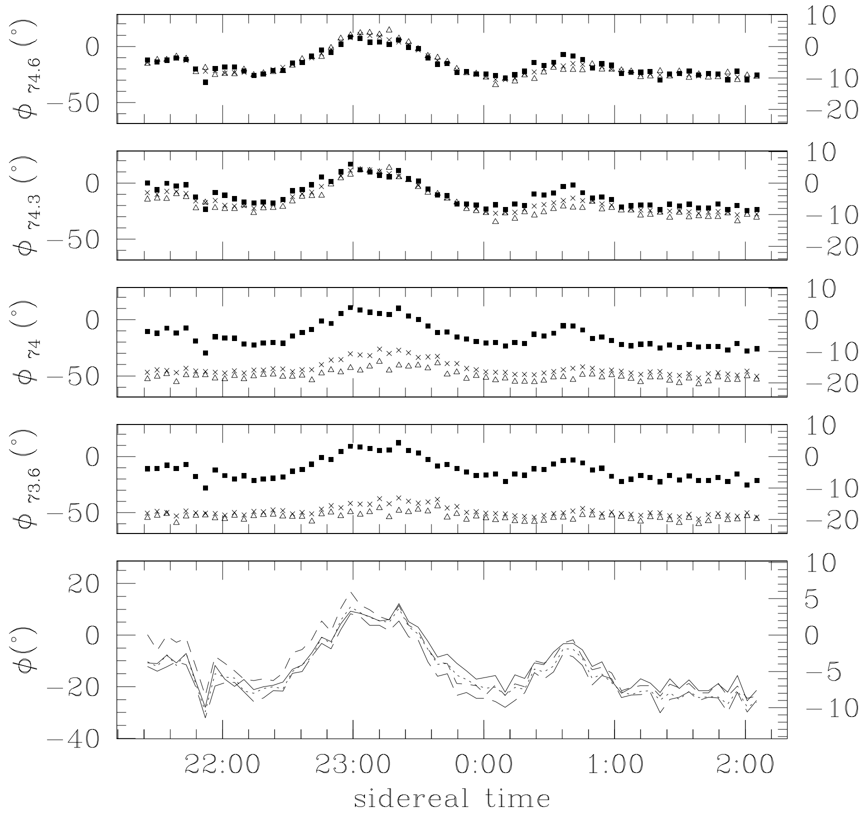

Figure 2.15: Calculated phases for all four frequency are shown in the upper 4 panels. The filled squares, open triangles and crosses represent phases calculated for data at times with: only a sky signal, only the interfering signal and both sky and interfering signal respectively. The vertical scale is in degrees on the left and in FLIRT phase units (range −64 to 64) on the right. The interfering signal has a large effect on the phases calculated for low frequency channels if it is not removed. The lowest panel shows the sky signal phases for all four frequency channels; solid, dotted, short dashed and long dashed lines correspond to 73.6, 74.0, 74.3 and 74.6 MHz channels respectively. The curves agree to within 2-3 FLIRT phase units.

2.3.3 Gain calibration

The goal of gain calibration is to take an observed spectrometer voltage, V_{obs}, and convert it to a flux density. The power received at an antenna is detected and converted into a measurable voltage which is directly related to an antenna temperature. The first step in calibration is to convert the observed voltage into an antenna tem-

Figure 2.16: The upper two curves are data taken once the array was properly phased. The upper solid line is a drift scan of the 15 kJy source Cas A and the lower solid line is a scan with the array pointed directly overhead. The dotted line shows a scan of Cas A before the array was properly phased. Pointing directly overhead with the array in the unphased state produced essentially the same signal.

perature, which can be written as:

$$V_{\rm obs} = V_{\rm off} + A(T_{\rm sys} + T_{\rm sky}) \tag{2.19}$$

where $V_{\rm off}$ is an offset voltage produced by the op-amps in the FLIRT spectrometer, $T_{\rm sys}$ is the receiver system temperature, $T_{\rm sky}$ is the sky temperature and A is a scale factor. In practice, A is not constant, with both diurnal and seasonal variations. These drifts are not accessible with the calibration data that was taken for this experiment. However, an experiment using the same array for pulsar studies found diurnal variations in the gain at the $10-20\%$ level, while seasonal variations led to the gain ranging from $\sim 0.5-2$ times the mean value (Gupta, Rickett, and Coles 1993). Furthermore, $T_{\rm sys}$ is actually the sum of all non-astronomical sources of power in the system, including steady sources of RFI. The contribution of interfering sources is estimated below, but cannot be removed.

The absolute flux calibration of a large beam, low frequency radio antenna such as the FLIRT array is fairly difficult for two main reasons. First, point sources must be very bright to dominate the total power received. Second, the contributions from galactic emission are sizeable and poorly constrained. These problems would, in principle, be alleviated by using a map at 74 MHz with resolution $< 1°$. However, no such maps exist. Therefore, the method to calibrate FLIRT data relies heavily on

Table 2.1: Point source removal parameters.

Source	$T_{sky}(K)$	$T_{source}(K)$	r_0 (°)	α
Vir A	18	37	1.9	2.86
Cas A	54	330[a]	2.1	2.8
Cyg A	35	300	2.1	2.8
Tau A	32	42	2.4	2.3

[a]The temperature of Cas A was also multiplied by 0.9 to account for fading of the SN remnant since the observations included in the Haslam map (Baars *et al.* 1977; Hook, Duffett-Smith, and Shakeshaft 1992).

two radio maps, the Haslam map at 408 MHz (Haslam *et al.* 1982) and GEETEE map at 34.5 MHz (Dwarakanath and Shankar 1990).

Calibration data were taken sporadically during the experiment and the most useful data consist of scans of many hours in which bright sources were allowed to drift overhead. Using drift scans rather than pointing scans for calibration reduces uncertainty due to the imperfect knowledge of the off-axis response of the primary elements. The method used here is to compare observed drift scans with simulated 74 MHz maps and derive the gain calibration by fitting the data to a series of models.

Making 74 MHz maps

Three maps were constructed based on the Haslam and GEETEE maps. The GEETEE map covers declinations from $-50°$ to $+70°$ and has several large scale spurious features. For this reason, the Haslam map was used as a template in all three maps. The first map is a simple scaling of the Haslam map using an $\alpha = -2.6$ spectral power law ($T = T_0(\nu/\nu_0)^\alpha$). The second map was generated by removing four strong sources at moderate declinations using a gaussian model of the sources (see Table 2.1). A gaussian of the form $T_{\rm source} * exp(-(r/r_0)^2)$ was removed from the Haslam map, scaled as $T_{74} = T_{408}(74/408)^\alpha$ and added back to the map. The galaxy was then scaled using $\alpha = 2.5 - 0.3\cos^2(b)$ (cf. Kraus 1986, Figure 8.6). Point sources were scaled separately and added back to produce the final map. The third map was made by calculating a spectral index between the Haslam and GEETEE maps. Regions near the spurious features listed in the GEETEE map were assigned a spectral index of -2.6.

Table 2.2: Array element gains

element	0	1	2	3	4	5	6	7	8	9	10	11	12	13	14	15
A_{obs}	3.9	0.8	1.9	0	1.0	0.7	1.1	0	0.16	0.5	0	0.4	0.6	0	0.3	0.6
G_{set}	5.3	0.9	1.2	0	0.7	0.6	0.9	0	0.13	0.5	0	0.4	0.6	0	0.3	0.7
A_{sim}	3.9	0.8	1.8	0	1.0	0.7	0.6	0	0.18	0.6	0	0.5	0.6	0	0.3	0.5

Beam models

Three different beam models were used. The first model is that of §2.3.1, assuming an ideal array. The second model left out 4 elements with poor phasing amplitudes, since these elements are unlikely to be functioning. The third model used measured gains of individual elements from phasing amplitudes in the beam model. The individual antenna gains are shown in Table 2.2.

Cygnus A scans

Cygnus A is a radio loud galaxy with a integrated flux density of 17 kJy at 74 MHz (Baars *et al.* 1977) at a declination of $+40.6°$ and is thus a useful calibrator for FLIRT. Drift scans pointed at $+40.6°$ were performed and each of 9 models were compared to the data using the model

$$V_{data} = A * T_{model} + B \tag{2.20}$$

where V_{data} is the observed spectrometer voltage and T_{model} is the model 74 MHz temperature produced by convolving the beam pattern with a model map. Fitted values, A and B, along with reduced χ^2 values, are shown in Table 2.3 for a single frequency channel. In addition, the RMS deviations between the models and the data are used to calculate a systematic error, σ_{sys} in sky temperature.

Clearly there are large systematic deviations between all models and the data, but the scaled map using a full array beam model has, by far, the lowest reduced χ^2. This model plotted with a set of data is shown in Figure 2.17.

As calculated, the values of B are related to terms in Equation 2.19 by:

$$B = V_{\mathrm{off}} + AT_{\mathrm{sys}} \tag{2.21}$$

.

Table 2.3: Temperature model fits

Model	B (Volt)	1/A (K/Volt)	χ^2	σ_{sys}
$\alpha = -2.6^{\mathrm{a,d}}$	147	165	780	1200
$\alpha = -2.6^{\mathrm{a,e}}$, inc	135	110	470	600
$\alpha = -2.6^{\mathrm{a,f}}$, var	110	63	860	500
p.s.[b,d]	152	141	400	700
p.s., inc[b,e]	146	99	350	400
p.s., var[b,f]	124	49	540	300
scale[c,d]	133	105	90	200
scale, inc[c,e]	119	79	260	300
scale, var[c,f]	105	61	1400	600

[a]Haslam map scaled by $\alpha = -2.6$
[b]Haslam map with point source scaling
[c]Pixel by pixel scaling between GEETEE and Haslam maps
[d]Full, perfect subarray
[e]Subarray with gains of 4 elements set to 0
[f]Subarray with gains as in Table 2.2

The values of V_{off} were measured in the lab; subtracting the values from B yields receiver temperatures of $7000 - 14000$K in the channels of the working subarray. Clearly these are very high and are indicative of both the relatively noisy receiving system and the large degree of RFI leakage into the passbands. An indication that a large contribution comes from RFI is that the system temperature is different in adjacent channels and on different days. A rough guide to the contribution that a single interfering source can make is given by the variable RFI that is present in all FLIRT data. In the calibration scans mentioned above, it is filtered out, but using the calibration indicates that it can contribute ~ 3000 K to the antenna temperature. If an RFI source is steady, rather than intermittent, this amount is simply included in the calculated T_{sys}.

FLIRT sensitivity

The sensitivity of a radio array can be expressed as the expected signal-to-noise ratio, $\mathcal{R}_{\text{sn}}$, given by:

$$\mathcal{R}_{\text{sn}} = S\frac{G}{T_{\text{sys}}}\sqrt{\Delta\nu\tau} \tag{2.22}$$

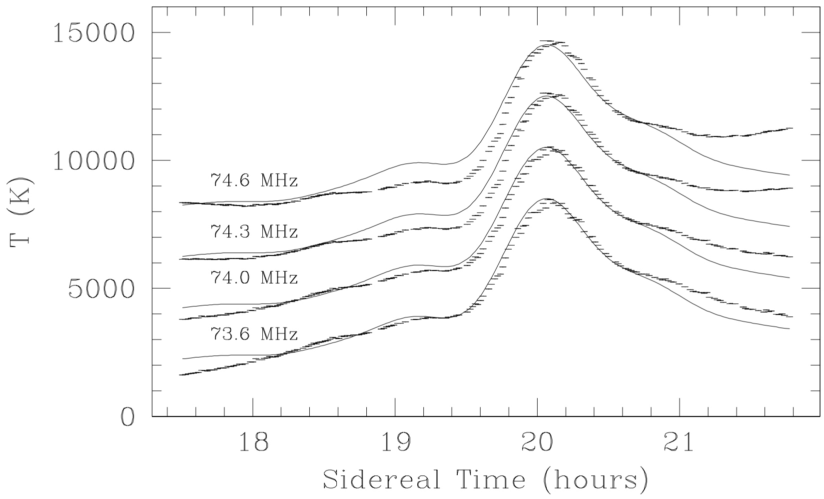

Figure 2.17: Cygnus A drift data offset and scaled according to the best of the models discussed in the text. For clarity, the 74.0, 74.3 and 74.6 MHz channels have been offset by 2000, 4000 and 6000 K respectively.

where S is the flux density of the source in Jy, G is the gain of the array in K/Jy, $\Delta\nu$ is the bandwidth in Hz and τ the integration time in seconds.

The gain, G, can be calculated by using drift scans of either Cas A or Cygnus A. The flux density of Cygnus A at 74 MHz is 17.1 kJY (Baars *et al.* 1977). Correcting for the declination of 40.6° gives an observable flux density of 15.7 kJy. Using Cygnus' flux density and the 81.5 MHz flux density ratio of Cas A to Cygnus of 1.11 ± 0.4 (Hook, Duffett-Smith, and Shakeshaft 1992) and taking into account the fading of the supernova remnant (Baars *et al.* 1977; Hook, Duffett-Smith, and Shakeshaft 1992), the 74 MHz flux density of Cas A is 17.8 ± 0.7 kJy. Accounting for the declination of 58.5° lowers the observable flux density of Cas A to 8.9 kJy. Measuring the strength of either of these sources above the background gives the gain, G, in FU/Jy*, and the gains thus calculated for Cygnus A and Cas A are in agreement. Converting from FU to K is done via the scaling discussed in §2.3.3. The gain, G, is found to be 0.25 K/Jy. The gain can also be calculated as

$$G = \frac{A_e}{2k_b K_s} \tag{2.23}$$

*FU = FLIRT digital unit

where A_e is the effective area of the array, essentially the geometrical area in this case; k_b is Boltzmann's constant; and K_s is a receiver constant, equal to 1 for a total power receiver. The geometrical area of the array is 930 m^2, but only 12 of the 16 elements are functioning, reducing the area to 700 m^2 and giving a gain of 0.25 K/Jy, remarkably close to the measured gain.

The bandwidth ν is the predetection bandwidth, which for a single stage filter, as used in FLIRT, is $\nu \sim 3 \times \nu_{3dB}$ where ν_{3dB} is the half-power bandwidth, which is measured from Figure 2.8. Furthermore, the integration time, τ, needs to be corrected for sampling below the Nyquist frequency which Equation 2.22 assumes. Each channel is sampled $\sim$ 9 times during a DOS interrupt, so each sample represents an integration time of 6 ms, while the time constant of the filters is 2 ms. This effectively reduces the integration time by a factor of 6.

Thus, each term in Equation 2.22 is independently measured; the calculated and observed $\mathcal{R}_{\rm sn}$ agree to $\sim 5\%$. Turning this around, using a 10 second integration with a system temperature of 15000 K, a 300 Jy steady source would be detected with a $\mathcal{R}_{\rm sn}$ of 10.

Having covered the calibration of the FLIRT array, the following chapters discuss the search strategy and results.

Chapter 3

Data analysis

3.1 Overview

This chapter discusses the FLIRT data in greater detail, focusing particular attention on how the data are processed. The data must first be corrected for the worst effects of RFI, a process which is discussed in §3.3. Once the data have had RFI removed, they can be searched for interesting transients, the subject of §3.5. A schematic of the RFI excision and search process is given in Figure 3.1. As described in §3.6, artificial dispersed transients are added to the data to assess the sensitivity of the search. As expected in a search for radio transients, most transient events are of terrestrial origin. §3.7 discusses typical RFI events which produce the background events for FLIRT. Results are presented in Chapter 4.

3.2 Description of data

As discussed in §2.2.5, during the bulk of the experiment, four frequency channels from each of four subarrays were sampled. For each DOS clock interrupt, voltages from the 16 used spectrometer channels were read sequentially and values were added to running totals for each channel; only the sample totals were saved to disk every clock interrupt (0.0549 s). Typically 8 or 9 reads were performed per channel per interrupt. Data were stored in records of 512 samples, or 28.1 s, with logging information kept for each record. The software allowed re-phasing every record, but for GRB followup data, re-phasing was done only once every 16 records (450 s). Once a record was filled, it was written to disk, which took an average of 0.19 s. Except for these write gaps, the data are continuous and uniformly sampled. The standard observation length was 42 minutes (90 records) and was chosen to include the range of dispersion delays expected from cosmological GRBs. This observation length also conserved limited disk space and minimized file transfer times.

3.3 Interference excision

The goal of FLIRT is to find a correlated signal in adjacent frequency channels delayed by an amount consistent with interstellar dispersion. The data format is essentially a uniform time sampling of total power at each frequency, so the only processing required before searching for signals is to remove the most obvious terrestrial interference. Although FLIRT operates in the radio astronomy protected band from 73.0 – 74.6 MHz, the FLIRT spectrometer bandwidths are wide enough to allow significant contamination from out-of-band interference. As described in §2.3.2, the main interference comes from an intermittent narrow-band signal which leads to a series of steps in the data as seen in Figure 3.2. Roughly 20% of the data has more severe RFI in which there are multiple steps in between each large step as seen in Figure 3.3. In some scans, the square wave pattern is barely discernible above the noise in the raw data as seen in the upper traces of Figure 3.4. However, in each case, over a limited period of time the data are well-described by a roughly constant signal with some variance, that is, the data are normally distributed.

3.4 Changepoint analysis

To locate and remove jumps due to RFI, a time domain search was performed. A time domain filtering scheme was preferable to a frequency filter for two reasons. First, the main RFI signal is only quasi-periodic and the jump edges it produces are quite sharp. These two features lead to many broad harmonics in the frequency domain. Essentially, the frequency signature of the RFI is not as "clean" as the time signature. Second, since a heavily dispersed signal may appear as a weak baseline shift, it was desirable to avoid Fourier filtering techniques that would exchange large discrete jumps with weak long term structure.

The data around a jump can be reasonably described as being drawn first from one normal distribution, with mean μ_1 and inverse variance τ_1 ($\tau_1 = \sigma_1^{-2}$), and then a second, with mean μ_2 and inverse variance τ_2. Using Bayes theorem and an assumed

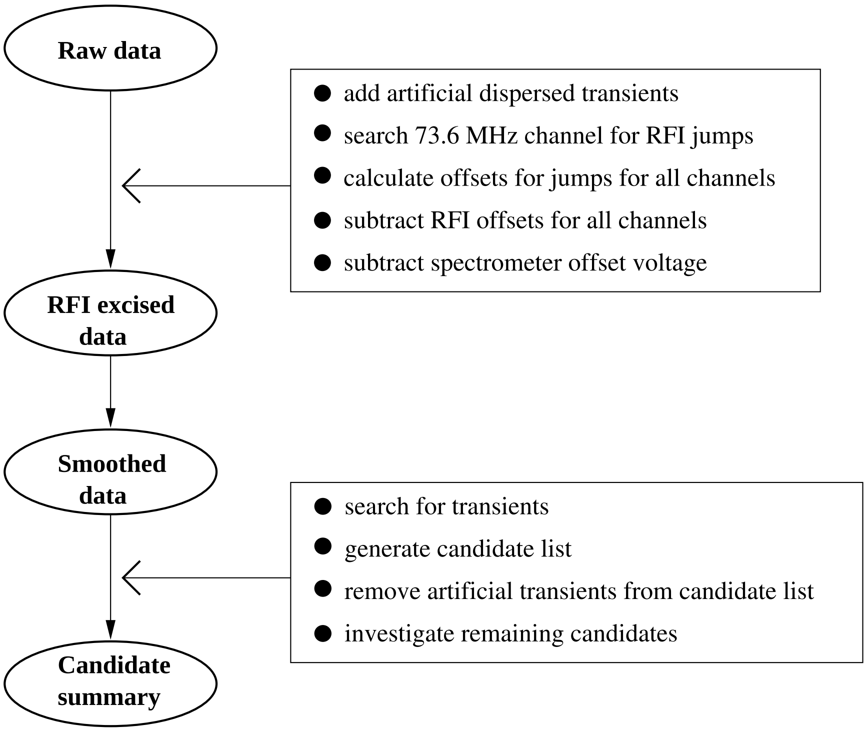

Figure 3.1: Schematic of the data analysis method outlined in the text.

prior probability distribution, one can compute the posterior probability distribution for a change occurring from one distribution to another anywhere along the data set. Following Smith (1975) and taking the prior element given by

$$d\tau_1\, d\tau_2\, d\mu_1\, d\mu_2{}^{*} \tag{3.1}$$

the probability of a changepoint occurring among the points $x_1 \ldots x_n$ at a point, r, is given by

$$\begin{aligned} P(r) \quad \propto \quad & \pi^{2-n/2}\Gamma(\frac{1}{2}r+\frac{1}{2})\Gamma(\frac{1}{2}(n-r)+\frac{1}{2})\,(r(n-r))^{-1/2} \\ & \left(\sum_{i=1}^{r}(x_i-\bar{x}_r)^2\right)^{-1/2(r+1)}\left(\sum_{i=r+1}^{n}(x_i-\bar{x}_{n-r})^2\right)^{-1/2(n-r+1)}, \end{aligned} \tag{3.2}$$

where $\bar{x}_r$ and $\bar{x}_{n-r}$ are the means of the points $x_1 \ldots x_r$ and $x_{r+1} \ldots x_n$ respectively. The most intuitive terms of Equation 3.2 are the summations which favor small

*Smith (1975) states that Equation 3.2 holds for the prior $\tau_1^{-1}\tau_2^{-1}\, d\tau_1\, d\tau_2\, d\mu_1\, d\mu_2$ rather than the prior in Equation 3.1 which is incorrect.

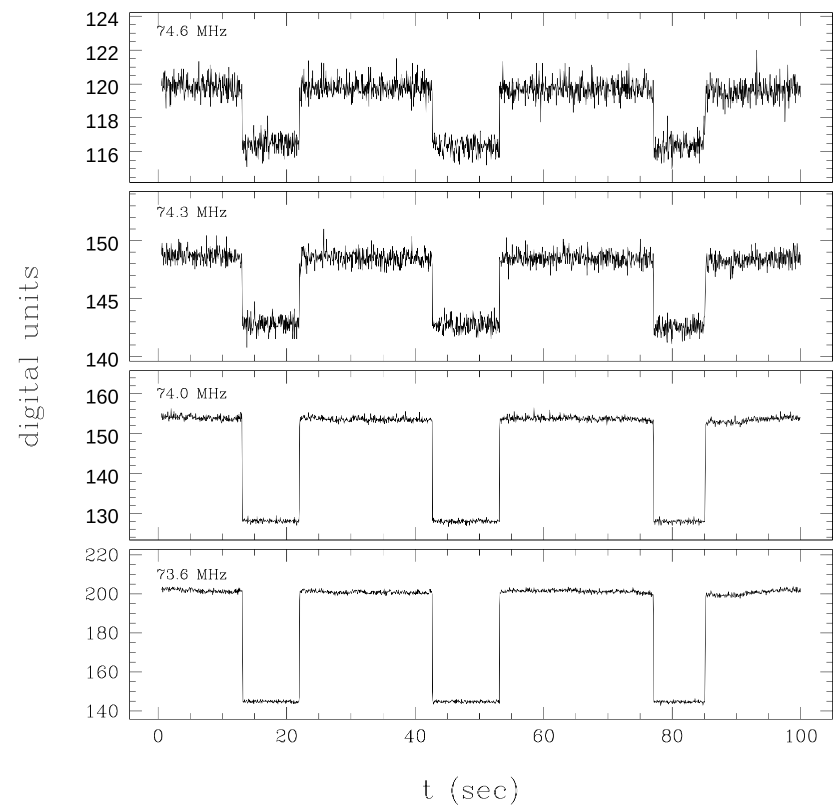

Figure 3.2: By far the most common type of RFI in FLIRT data, a step function strongest at low frequencies. The jumps shown here are large, but fairly typical. Units on the vertical axis are digital levels from the spectrometer AD converter.

variances in the divided data sets. The remaining terms serve as weights for the changepoints occurring at any point in the sequence.

Equation 3.2 is strictly true for a dataset with a single changepoint. However, in practice, it is possible to detect a changepoint in a data set with more than one changepoint and subdivide the data to look for remaining changepoints. A C program was written which recursively subdivides a block of data finding all significant changepoints. The method works well as a first pass on the data to determine where jumps occur in the data. The results of the process can then be adjusted manually to achieve the best result. For obvious reasons, the algorithm has more trouble with RFI like that seen in Figure 3.3 than like RFI seen in Figure 3.2. In the former case,

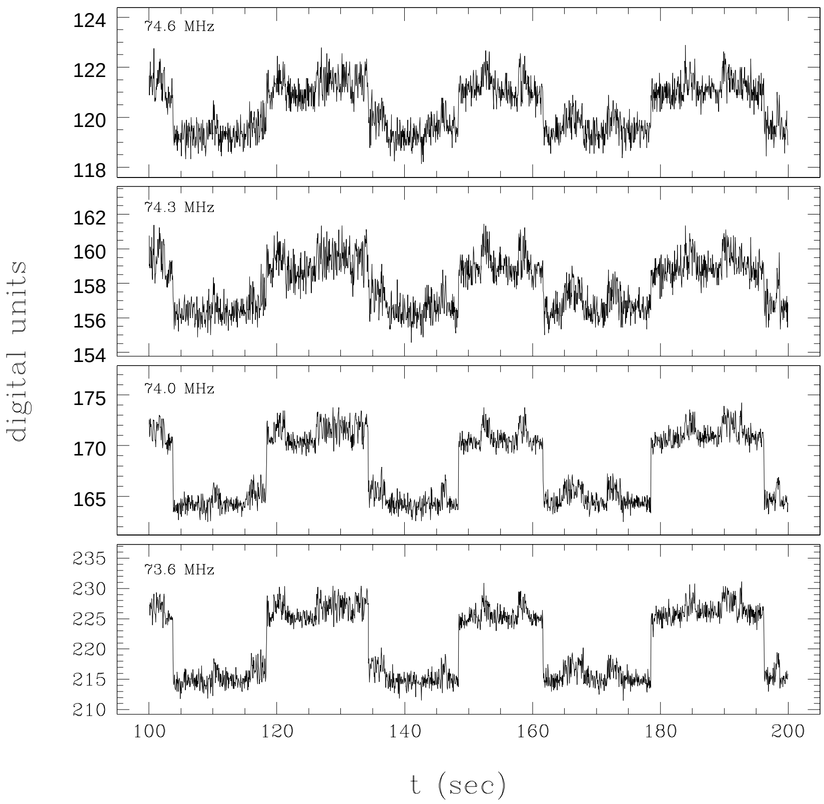

Figure 3.3: Less common and more troublesome RFI has multiple levels in each step. Units on the vertical axis are digital levels from the spectrometer AD converter.

the jumps can occur with very different amplitudes and it is difficult to tune the algorithm to pick them out as well as the human eye does. Therefore, these scans required the most time in manual processing.

The largest offsets are due to a low frequency signal, so the jumps are detected using only the 73.6 MHz channel data. To correct the RFI contaminated data, the average value in each data segment (i.e., between jumps) is calculated. For any section with RFI contamination, an offset is measured and subtracted to bring the data in line with neighboring sections. Once the offsets are removed from the data, they are ready to be searched for transient signals as described below in §3.5. The cleaned data from Figure 3.2 is shown in Figure 3.5.

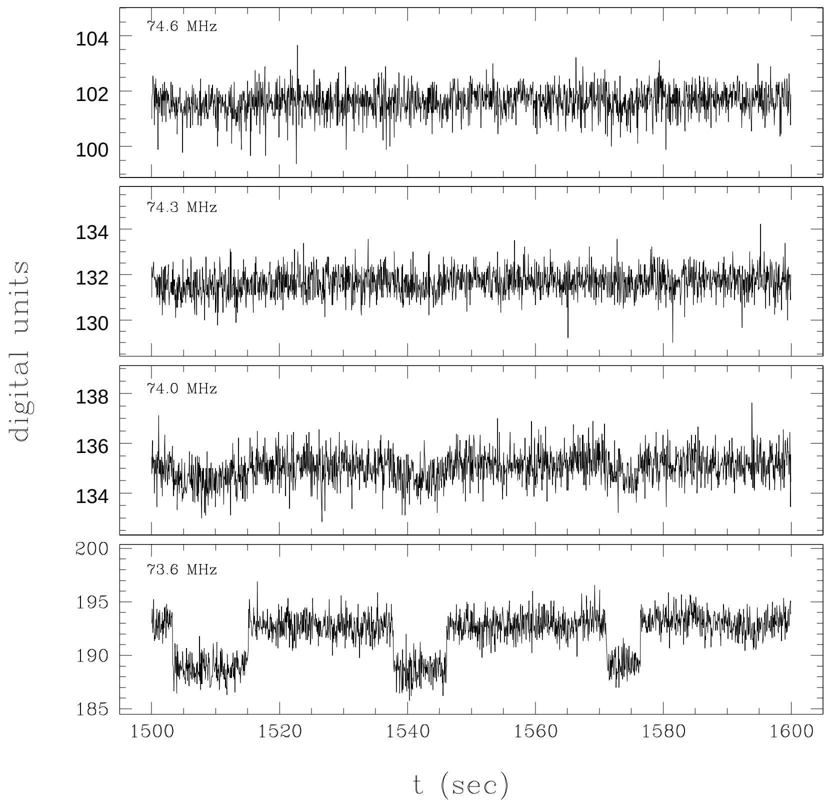

Figure 3.4: When RFI offsets are small in channels from the phased subarray, another subarray can sometimes be used as a guide to where RFI occurs. In this plot, the low frequency channel is from an unphased subarray and all others are from the phased subarray.

3.5 Search method

After RFI excision was completed, the data were scanned in segments to look for dispersed signals. In order to detect a signal at a given dispersion measure, the data are averaged over a time comparable to the dispersion smearing across a channel bandwidth. Table 3.1 lists the smoothing times used for searching. Two basic search methods were employed. The first was to observe the 73.6 MHz and 74.6 MHz channels along with their difference. Any places where sharp deviations in the difference were noted and all four channels were checked later. If a convincing candidate was found, it was noted and the search continued. The second method was to observe all

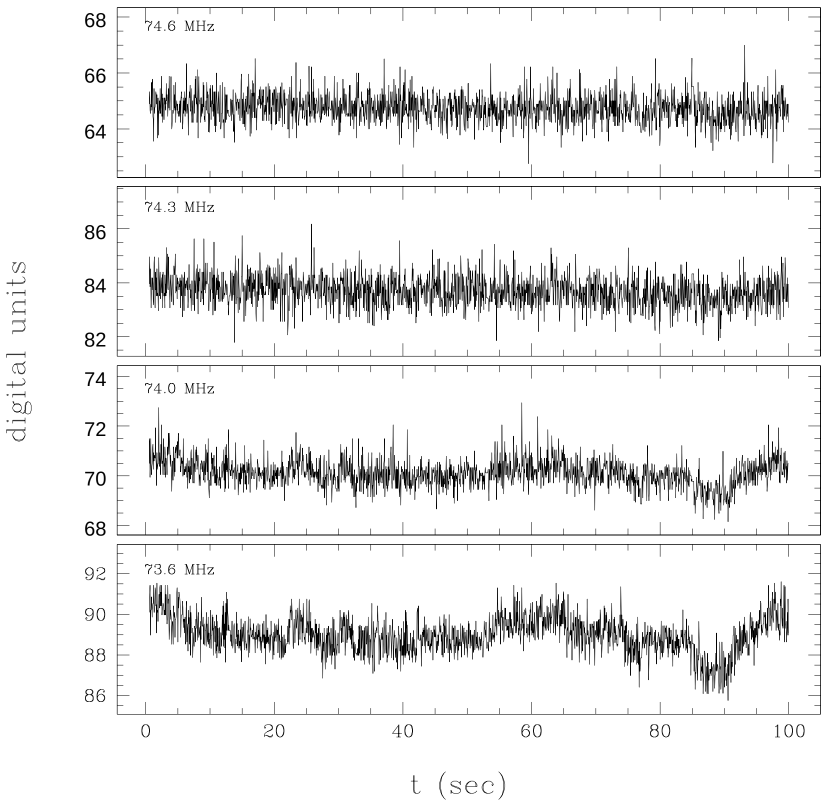

Figure 3.5: The same data as in Figure 3.2 but with RFI offsets removed. Known spectrometer voltage offsets ($\sim 50-60$ units) are also subtracted from each channel. Clearly there is some residual RFI in the low frequency channels, but it is at a tolerable level.

four channels directly. The former method works best in noisy sections of data where it draws the eye to the most interesting parts of the data. However, for most scans, the direct observation of all four channels was easier.

Given the 18.2 Hz effective sampling rate and a 1 MHz difference between low and high frequency channel centers, the minimum detectable DM would be 2.7 pc cm^{-3} with a single sample delay between high and low frequencies (the two middle channels could be aligned with either the high or low frequency channel). Such a signal is unlikely to be convincing, especially near the detection limit for the search. A more conservative lower limit on the measurable DM would require a single sample offset between each successive pair of frequency channels, giving a minimum detectable DM

Table 3.1: The number of samples averaged over, the DM and the corresponding time interval for which peaks in each successive channel will be delayed by one time interval. t_{samp} is 0.055 × samples.

samples	DM (pc cm^{-3})	t_{samp} (sec)
1	8	0.055
3	24	0.17
7	56	0.38
12	96	0.66
22	176	1.2
39	312	2.1
70	561	3.8
126	1010	6.9
224	1795	12.3

of $\sim$ 10 pc cm^{-3}.

Once an interesting signal is detected, the dispersion measure can be estimated by measuring the delay time between peaks in the 73.6 MHz and 74.6 MHz channels. A cross-correlation between all pairs of channels can also be used to pick out small dispersion measures. Since only a crude measure of a DM is needed in the initial search, either of these methods proved sufficient to pick out interesting signals. In the over forty scans that were well searched, only thirteen signals passed this first stage of analysis and were subject to further investigation. Of these thirteen, eleven were inspected more carefully and were clearly RFI events. The remaining two candidate events, most likely also RFI, are discussed in Chapter 4. Thus, searching for dispersed signals is a very efficient way of eliminating terrestrial RFI.

3.6 Search sensitivity and simulated events

Strictly speaking, the limiting flux density of this search is a function of an event's duration, sharpness and dispersion measure. The strength and variability of RFI also affects the sensitivity. The expected biases include:

- events landing on RFI spikes are less likely to be detected,
- shorter events lead to less integrated flux density, making them harder to detect,
- very long events are indistinguishable from changes in the baseline,

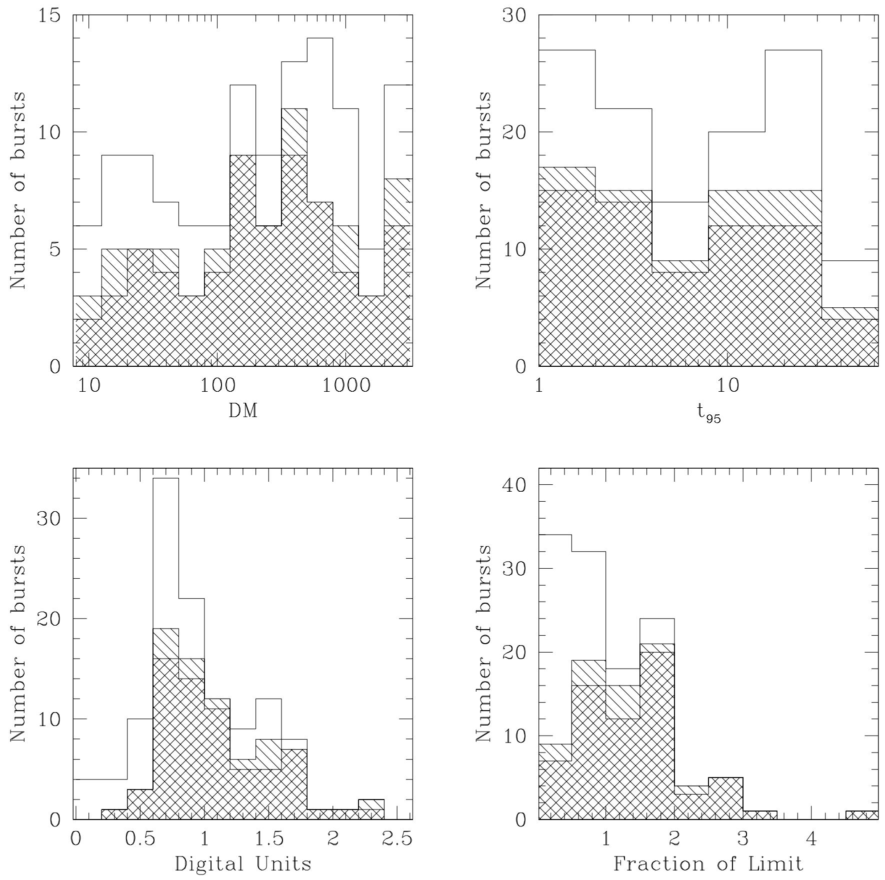

Figure 3.6: In each panel the solid line, cross-hatched region and singly hatched region denote respectively the total number of artificial events, the number of events detected and correctly identified and the number of events detected but mistaken for RFI or baseline variations.

- events with smooth features are not recognizably dispersed unless they have a large dispersion,
- low dispersion-measure pulses are difficult to distinguish from RFI, and
- a weak, highly dispersed signal will be stretched in time and therefore be indistinguishable from slow variations in the baseline flux.

To quantify these effects, 5 simulated bursts were added to each of 24 scans prior to the RFI processing discussed in §3.3. The bursts had random amplitudes chosen to

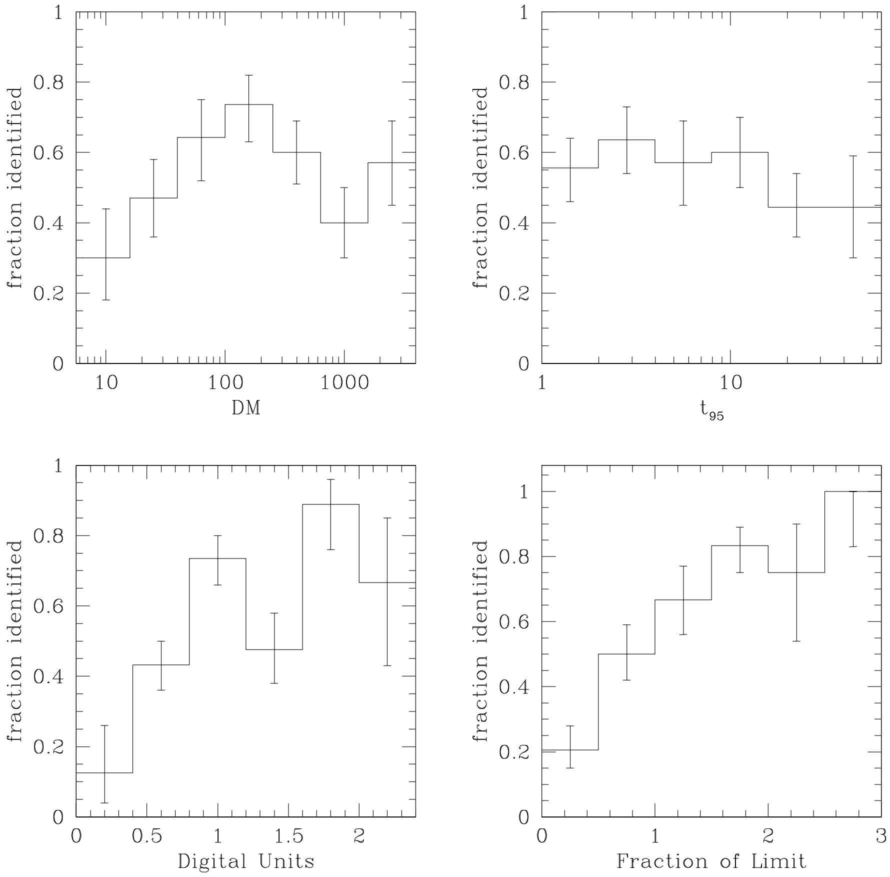

Figure 3.7: The efficiency of the detection algorithm. Only events that were correctly identified are included in the efficiency. Uncertainties are 68% confidence limits.

be near the detection limit. They also had randomly assigned positions, durations and dispersion measures. All events were dispersed gaussians: short gaussians (FWHM ~ 0.2 s) represent bursts with short timescale structure and long gaussians (FWHM ~ 10 s) represent smoother profiles. These are in some sense the worst cases to look at, as a more structured transient would be more noticeable.

A standard detection limit of 1 spectrometer ADC digital level peak amplitude in the 73.6 MHz channel was assumed, only slightly above a typical RMS of 0.6 for 50 ms integrations. This limit corresponds to ~ 400 Jy for a burst directly overhead. Artificial bursts were put in near this level to test the detection limit for each scan.

If RFI was particularly bad and the scan was generally noisy, the adopted limit for that scan was increased by a factor of 2 over the standard limit. If the scan was particularly quiet and all artificial bursts were easily detected, the adopted detection limit was lowered by a factor of 2.

Histograms displaying the recovery of artificial bursts are shown in Figure 3.6. The number of artificial bursts recovered as a function of both DM and t_{95} is reasonably uniform. This suggests that there are not significant selection effects biasing the search against any particular type of transient. The most informative histograms, however, are those showing the artificial burst detections as a function of raw spectrometer digital units and as a function of the adopted limits. By looking at the former, it is clear that the estimated limits are reasonable and that artificial bursts were generally put in near the limit of detection. The latter histogram shows that once the limits are adjusted by, at most, a factor of two, the artificial burst recovery rate is near $60 - 70\%$ at the adopted limits.

The same data are plotted as the fraction detected, giving an efficiency, in Figure 3.7. The uncertainties shown represent Bayesian 68% confidence limits computed using a binomial probability distribution. These efficiency curves quantitatively support the qualitative observations made at the beginning of this section. It should be noted that the largest amplitude artificial signal in the sample was placed coincident with an RFI spike. It was detected in the analysis but ruled an RFI event. On the whole, this analysis shows that the search method outlined in §3.5 is roughly 70% efficient at the adopted limits (see §4.5 for limits on individual bursts).

3.7 Backgrounds

In a search for transient radio emission, there are many “background” signals; signals which are definitely not of astronomical origin and must be identified as such. In this section a few examples are included to give a sense of what the background for an experiment like FLIRT is.

In Figure 3.8, a fairly common source of interference is shown. FLIRT is located on the Fallbrook Weapons Depot, land owned by the US Navy and adjacent to the Marine base Camp Pendleton. There is often quite a bit of helicopter traffic in the area and this signal shows up when helicopters come within a few kilometers of the array. Easily identifiable helicopter signals such as this occurred in only five data files.

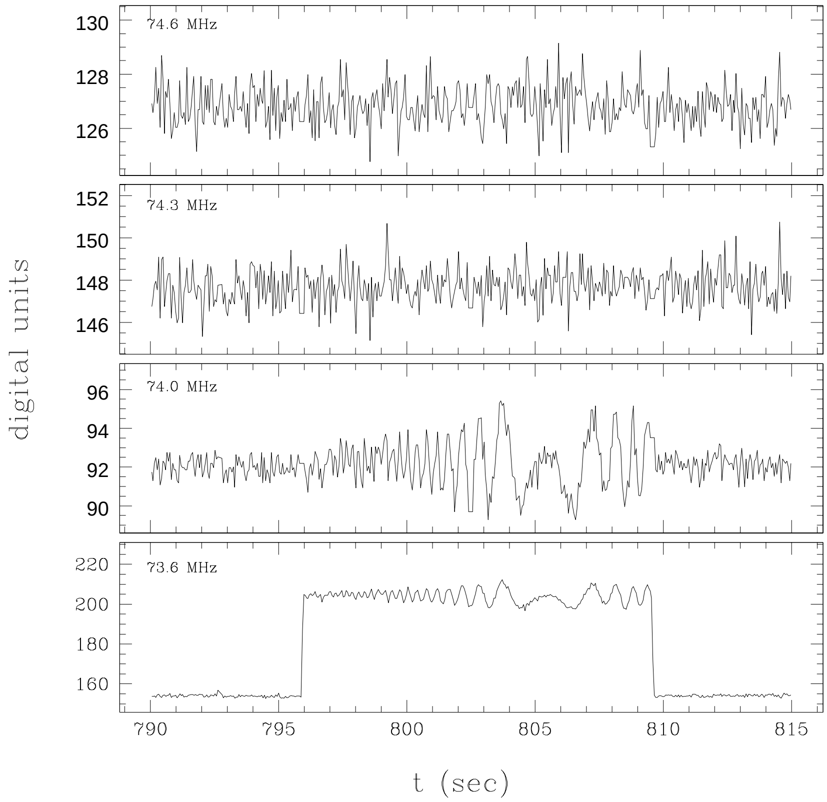

Figure 3.8: The signature of a helicopter. The 73.6 MHz data are raw, all other channels have a constant offset removed while the RFI is on. The interference pattern from the helicopter is only seen while the low frequency RFI is active, indicating that the helicopter is providing a secondary path for the signal to reach the antenna.

While searching data for differences between the 73.6 MHz and 74.6 MHz channel data, spikes like those shown in Figure 3.9 were detected. Presumably a narrow-band pulse is emitted first on one side, then the other of the protected radio band in which FLIRT operates. These spikes are easy to distinguish from dispersed pulses since a dispersed signal is expected to be systematically delayed as the frequency decreases, while the signal observed here is clearly two pulses of limited bandwidth. Signals such as these are fairly rare on the whole, but may appear quite often in a given data scan. One file had $\sim$ 30 such events, but fewer than five scans total had such obvious pairs as seen in Figure 3.9.

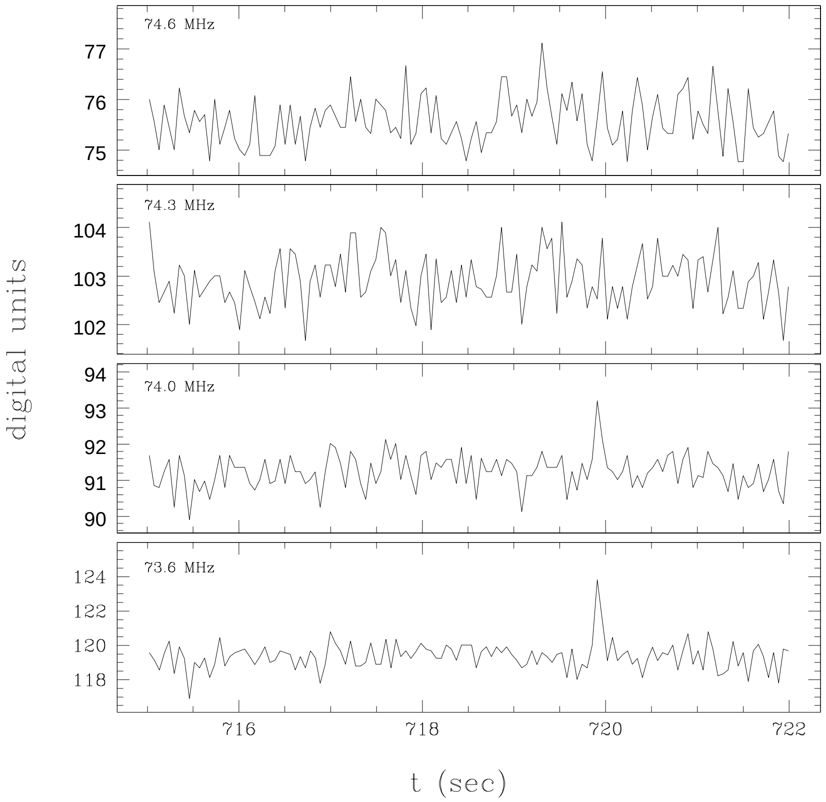

Figure 3.9: An interesting background event; a high frequency, narrow-band signal is detected, followed 0.6 seconds later by a low frequency spike. The low frequency spike is detected in all four channels. In other such events, the ordering of frequencies can be reversed.

In Figure 3.10, a residual baseline fluctuation is shown. These are typically easily discarded since they are not often detected in the high frequency channels. They are only detected when the main RFI source is on and varying or in a transition. Nevertheless, artificial bursts were occasionally mistaken for fluctuations like this. In most scans, such events were passed over immediately, but as many as four from a given data file were investigated more closely.

In Figures 3.11 and 3.12, the signals show no dispersion so they may be ruled out as astronomical sources. Broadband single RFI events like this occurs in $\sim 10\%$ of the data files. Two other files show dozens of non-dispersed transients which are likely to be solar in origin. The origin of the signals in Figures 3.11 and 3.12, however, in

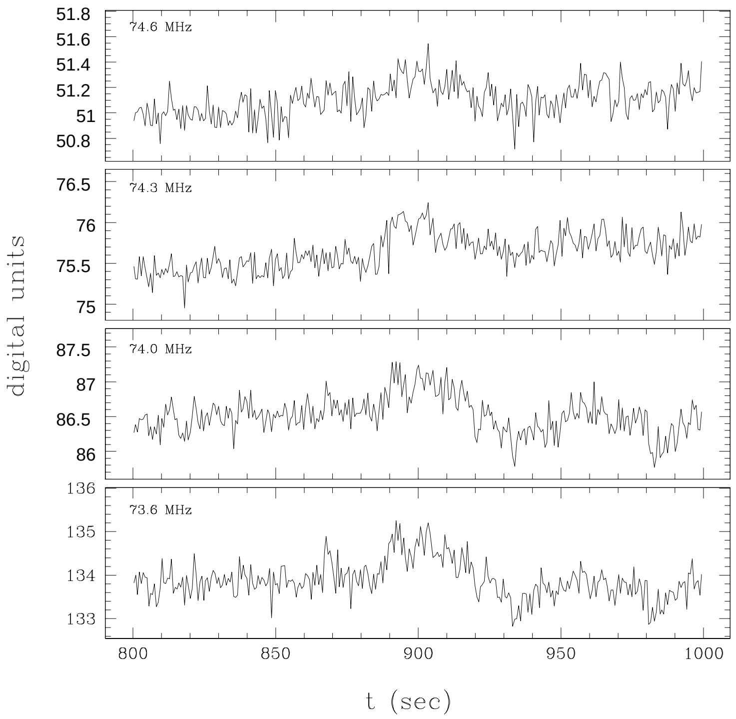

Figure 3.10: A typical baseline fluctuation.

unknown. In a typical data file, about five signals warranted closer examination than the rapid visual search. However, the number of such signals varied from essentially none up to roughly thirty. Most were clearly related to the low frequency RFI that is a constant problem at the FLIRT site. Once these events are excluded, there were only ~ 10 more interesting RFI signals which were pursued in any depth. Despite the large number of interfering signals, they are efficiently removed from consideration with the method outlined in this chapter.

An obvious way to improve on the experiment described in this thesis would be to use more spectral channels with much narrower bandwidths. Some interfering sources are very narrow-band and as much as 20 dB above the noise floor. Such strong signals make broad filters like those used for FLIRT highly susceptible to even small variations in the interfering signal. Nevertheless, with the methods described in the preceding sections, it has been possible to recover potentially interesting signals, as will be discussed in Chapter 4.

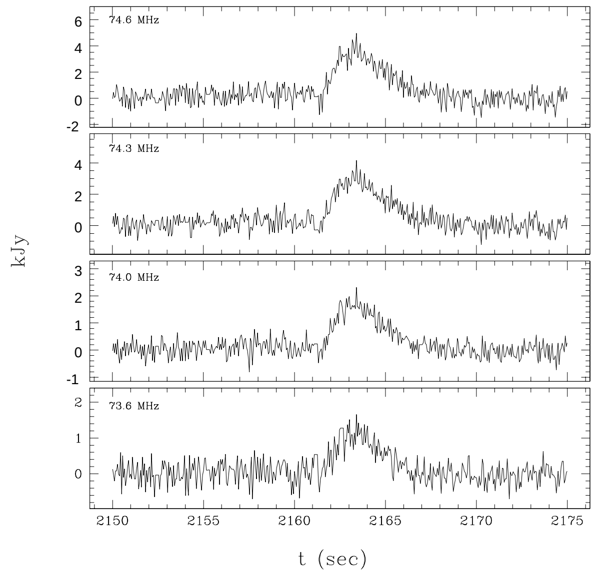

Figure 3.11: A non-dispersed pulse (DM < 6). The vertical axis is in kJy assuming an overhead source. This is most likely a fairly narrow-band signal between 74 MHz and 75 MHz.

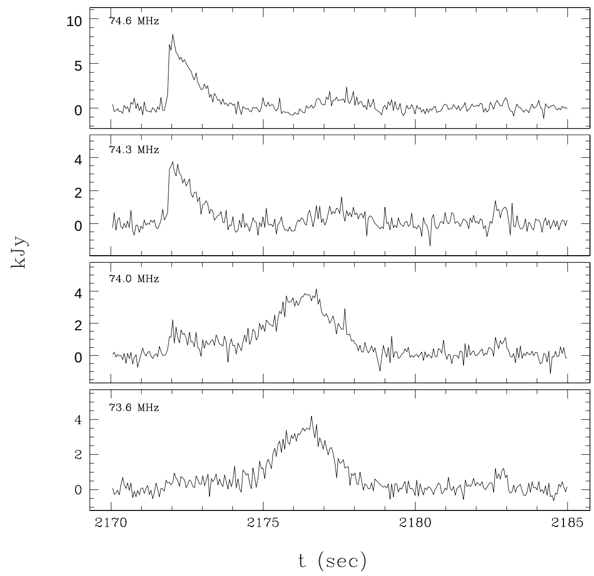

Figure 3.12: The most complex, non-dispersed signal seen in the FLIRT data. A decaying pulse at high frequency followed by a pulse at low frequency.

Chapter 4

Search results

4.1 Overview of results

In this chapter, the results of the FLIRT experiment are discussed. The parameters of the GRBs observed during the FLIRT experiment are presented in §4.2. In §4.3 and §4.4 two radio transients are discussed. These two transients are the only GRB counterpart candidate events which remained after the data processing outlined in Chapter 3. In §4.4.8, data on a solar flare are presented to provide support for arguments about spectral features made in §4.4. The solar data represent the only confirmed transient radio signals of astronomical origin observed by FLIRT. The main result, a set of flux density limits for prompt radio emission from GRBs, is presented in §4.5. The chapter ends in §4.6 with some concluding remarks about FLIRT and prospects for future experiments.

4.2 Observed GRBs

Parameters for the 34 bursts observed by FLIRT from September 1997 through March 1998 are presented in Table 4.1. During this period, one of the FLIRT subarrays was properly phased so that meaningful flux density limits for radio emission associated with GRBs could be calculated. All parameters in the table are taken from the online BATSE GRB catalog*. From August 1995 through August 1997, 86 additional GRB follow-up observations were made, but because the array was not yet properly phased, it is not possible to establish meaningful flux limits for this data set.

*Located at http://www.batse.msfc.nasa.gov/data/grb/catalog/

Table 4.1: Parameters of observed GRBs.

GRB name (yymmdd)	BATSE trigger	Fluence[a] 10^{-8} ergs cm^{-2}	RA (°)	DEC (°)	Error[b] (°)	l (°)	b (°)
GRB970903	6358	[c]	17.6	13.9	8.54	129.9	−48.7
GRB970906	6366	1 800	220.3	57.6	2.58	98.1	53.9
GRB970907	6368	230	346.9	11.3	8.32	86.2	−44.1
GRB970918	6385	22	31.5	40.2	6.42	138.0	−20.5
GRB970919	6390	2 100	298.6	59.6	2.69	92.5	15.7
GRB970925	6396	280	347.0	54.6	2.31	108.2	−5.3
GRB970926a	6399	140	139.4	18.3	2.46	211.3	40.3
GRB970926b	6400	360	313.7	40.4	1.82	82.0	−3.0
GRB970928	6401	55	168.3	78.6	9.19	128.8	37.3
GRB971002	6409	95	193.4	−8.0	2.85	303.8	54.9
GRB971012	6427	74	329.7	41.0	7.17	91.2	−11.0
GRB971015	6437	45	192.6	28.4	3.72	131.8	88.7
GRB971016	6439	9.5	51.8	49.3	17.89	147.2	−6.1
GRB971021	6443	100	147.0	3.4	9.45	233.2	40.3
GRB971029	6455	[c]	243.0	70.6	3.95	104.0	38.3
GRB971110	6472	26 000	241.7	50.4	0.62	78.8	46.5
GRB971120	6488	76	155.8	76.4	9.94	133.2	37.6
GRB971207	6523	270	95.1	3.4	1.39	206.3	−5.4
GRB971208	6526	17 000	356.5	77.9	1.19	119.4	15.5
GRB971209	6527	210	241.3	62.2	0.77	94.6	42.7
GRB971210	6529	90	253.5	32.7	5.63	54.7	37.9
GRB971220	6540	8.9	205.4	58.8	6.44	111.0	57.1
GRB971225	6545	350	265.1	64.7	1.83	94.2	31.9
GRB971228	6547	13	155.2	62.2	13.58	147.6	47.0
GRB971230	6552	110	147.6	−19.1	2.42	254.5	26.2
GRB980105	6560	1 499	37.2	51.7	1.43	137.9	−8.4
GRB980107	6562	9.2	190.2	−7.2	12.08	298.3	55.6
GRB980124a	6577	190	8.7	45.5	4.43	119.9	−17.3
GRB980124b	6579	220	345.6	−15.8	4.05	51.4	−62.3
GRB980125	6581	4 800	350.7	35.8	0.99	103.4	−23.7
GRB980315a	6641	59	75.8	20.4	3.63	181.8	−12.7
GRB980315b	6643	17	180.1	74.6	9.4	127.5	42.0
GRB980329a	6665	8 200	105.6	39.4	0.81	177.5	18.8
GRB980329b	6666	140	273.7	59.1	4.11	88.1	27.7

[a]Preliminary fluences are from the BATSE online catalog available at http://www.batse.msfc.nasa.gov/data/grb/catalog/flux.html.
[b]Statistical error (1σ).
[c]Fluence was not available for this burst.

4.3 GRB970925

The first radio transient not obviously of terrestrial origin was observed following GRB970925. The signal is weak, $\sim$ 1 digital unit (400 Jy overhead), and peaks roughly 3 minutes after the GRB. The signal bears a strong resemblance to long, relatively weakly dispersed artificial pulses which were added in the analysis. Since the signal is long ($\sim$ 90 s), it is difficult to detect a dispersion measure. Performing a cross correlation on the signals suggests a rough upper limit of DM < 150 pc cm^{-3}. The signal, along with the γ-ray light-curve, is plotted in Figure 4.1. The beam pattern at the time of the observation is shown in Figure 4.2.

The time delay between the peak of the γ-ray flux and the peak in radio emission is 185 s corresponding to a DM of $\sim$ 240 pc cm^{-3}. Such a large DM would have been easily observable. Assuming the limiting DM of 150 pc cm^{-3}, and that the radio transient and GRB are related, the radio emission would have begun at the GRB source after all the γ-ray emission had ended. Therefore there is no direct connection between the γ-ray emission and the radio transient.

The γ-ray light-curve in Figure 4.1 shows a rise within a few seconds of the rising edge of the radio pulse. The archived trigger report for this GRB [†] attributes the γ-ray rise to a Crab occultation rise. Data from all 8 BATSE Large Area Detectors (LADs) were checked for consistency with this interpretation. We found that the GRB signal and the claimed occultation rise illuminate different BATSE detectors, so that the two signals definitely came from different directions. We also know that the Crab could not have been in our beam. The Crab nebula was about 4 hours from transit at the FLIRT array. The FLIRT beam sensitivity at the position of the Crab, according to the beam model, is 40 dB down. Any more than 10 dB attenuation is enough to make the Crab nebula undetectable by FLIRT. Thus, the rise in γ-ray flux and the radio transient are not associated.

Roughly 30 seconds after the radio transient, a signal of similar duration but apparently greater brightness appeared in data from one of the non-phased subarrays. This subarray commonly detected the square-wave pattern from the main RFI signal, although it failed to detect any astronomical sources. A likely explanation is that a local moving source of RFI, perhaps a plane or helicopter, produced the signal. With only a limit on the DM and a similar transient displaced in time in a second subarray the association between the radio transient and the GRB is tenuous at best.

[†] Available from NASA/Goddard Space Flight Center's High Energy Astrophysics Science Archive Research Center Online Service http://cossc.gsfc.nasa.gov/cossc/BATSE.html.

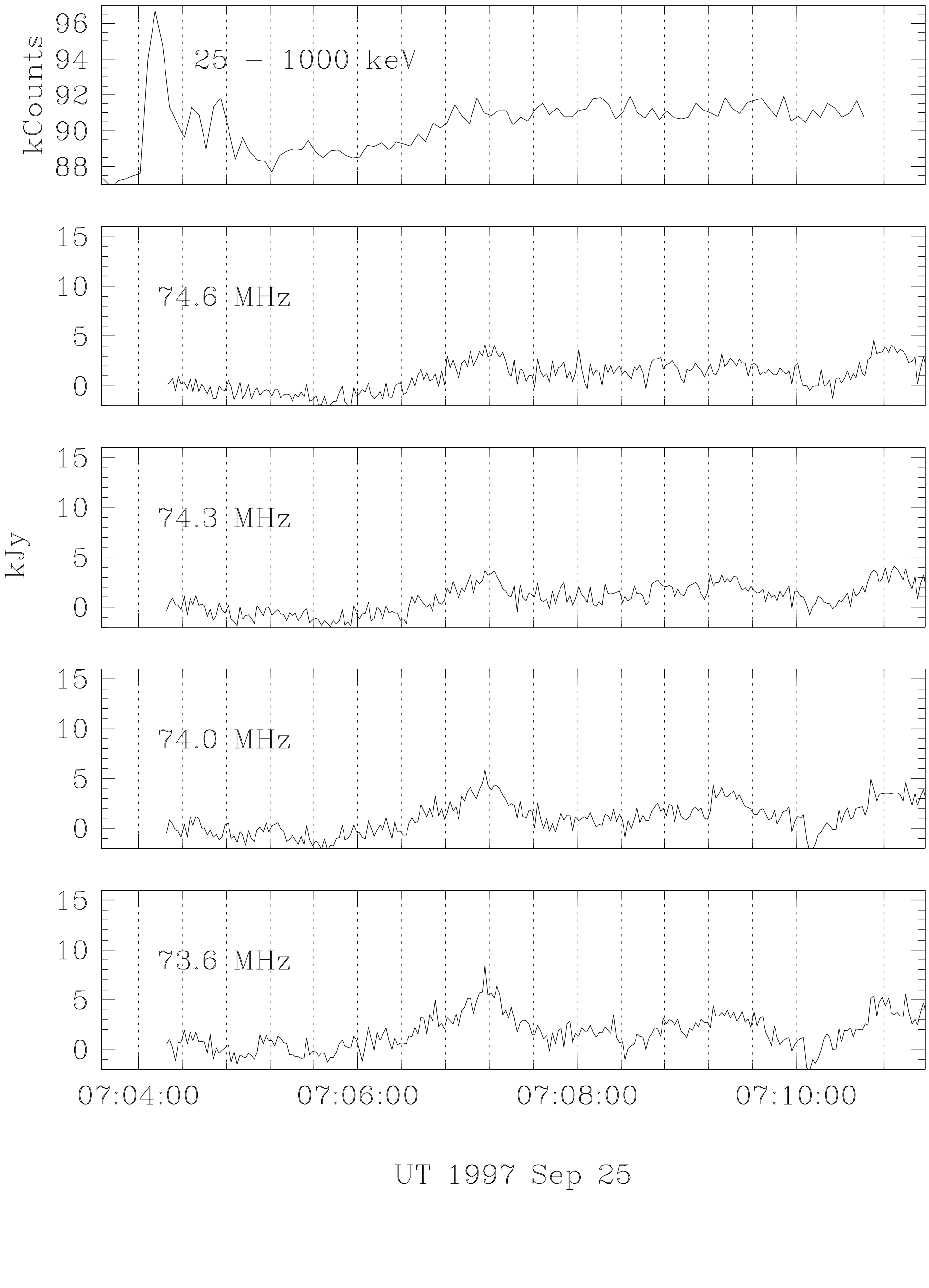

Figure 4.1: Radio and γ-ray light-curves for GRB970925. The γ-ray curve is the total number of counts in the energy range 25 keV – 1 MeV. The radio flux density scale is calibrated based on the LOCBURST position for the GRB. There is a coincident rise in γ-ray and radio signals from 7:05 to 7:07.

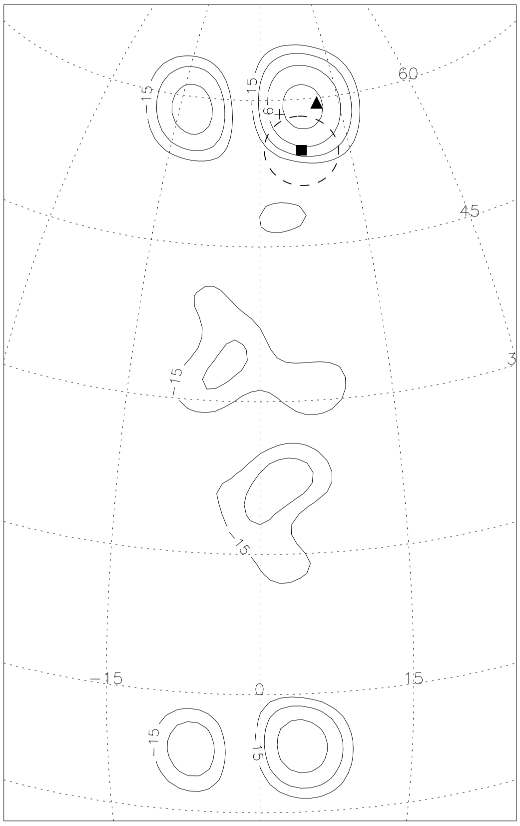

Figure 4.2: Map of the FLIRT beam pattern for GRB970925 as a function of hour angle and declination. Contours are plotted at every 3 dB and are relative to the maximum response capable with the array. The dashed circle outlines the BATSE 68% confidence position. The filled triangle and filled square mark the original GCN and final LOCBURST positions respectively. The + symbol marks the position of Cas A.

4.4 GRB980329

On March 29, 1998 at 03:44:47 UT, FLIRT responded to a burst that activated the BATSE onboard trigger at 03:44:38.49 UT. This burst, GRB980329, was also seen by a Wide Field Camera onboard the *SAX* satellite. As shown in Figure 4.3, FLIRT detected a spectrally complex signal just after GRB980329. §4.4.1 is a review of what is known about this GRB from BATSE and *SAX* as well as what is known about the GRB afterglow from the multi-wavelength followup observations made by other experiments. In §4.4.2 the FLIRT observations and data are described. The sensitivity of FLIRT to the GRB is discussed in §4.4.3. §4.4.4 is a discussion of whether the first spike seen in the data is consistent with a dispersed pulse. In §4.4.5, the possible effect of interstellar scattering is addressed and in §4.4.6 the likelihood of a chance coincidence of a RFI event and the GRB is considered.

4.4.1 The GRB and its afterglow

As observed by BATSE, GRB980329 lasted about 55 s, with a 10 s long, highly structured peak (Briggs *et al.* 1998). The peak flux of 8×10^{-6} erg cm^{-2} s^{-1} put it in the top 5% of the BATSE peak flux distribution (Meegan *et al.* 1998b). This burst was also observed by the by *SAX* WFC and localized with a $3'$ error radius. As of October 1998, this remains the brightest GRB observed by the WFCs onboard *SAX* (Frontera *et al.* 1998). A pointed observation with the *SAX* Narrow Field Instruments (NFI) was performed 7 hours after the burst. In the NFI observation a new X-ray source consistent with the position of the WFC source, now presumed to be the GRB afterglow, was detected and localized to $1'$ (in 't Zand *et al.* 1998).

On three consecutive days after the GRB, the X-ray error circle was observed with the VLA and a ~ 100 μJy source was detected with intra-day variability, suggestive of interstellar scintillation (Taylor, Frail, and Kulkarni 1998; Taylor *et al.* 1998). The position of the source is $\alpha = 07^{\rm h}02^{\rm m}38^{\rm s}.022 \pm 0^{\rm s}.004$, $\delta = 38°50'44.02'' \pm 0.05''$ (J2000) (galactic coordinates $l = 178.12$, $b = 18.65$). This source is the accepted radio afterglow of GRB980329.

Following the radio detection, many groups made optical and near-infrared observations of the VLA position. These observations are summarized in Palazzi, *et al.* (1998). The optical transient was very dim ($R > 22$, 16 hours after the burst) (Guarnieri *et al.* 1998) and red (Reichart *et al.* 1998). This has been attributed to extinction by dust (Taylor *et al.* 1998; Palazzi *et al.* 1998; Reichart *et al.* 1998), but Fruchter (1998) argues that the deficit in R is due to the GRB having occurred at high redshift, finding $z \sim 5$. However, this claim rests on the extrapolation of J and K lightcurves back to early times and on a somewhat uncertain I band observation. The possibility of the galaxy being at $z \gtrsim 5$ is also mentioned by Reichart *et al.* (1998) but not pursued. The effect of a high redshift GRB host galaxy on the expected dispersion measure of a radio transient is discussed briefly in §4.4.4.

The transient behavior of the X-ray, radio and optical sources are similar to those of other GRB afterglows and the link between the GRB and the transient source seems quite secure. Thus, for this burst we have a very accurate position.

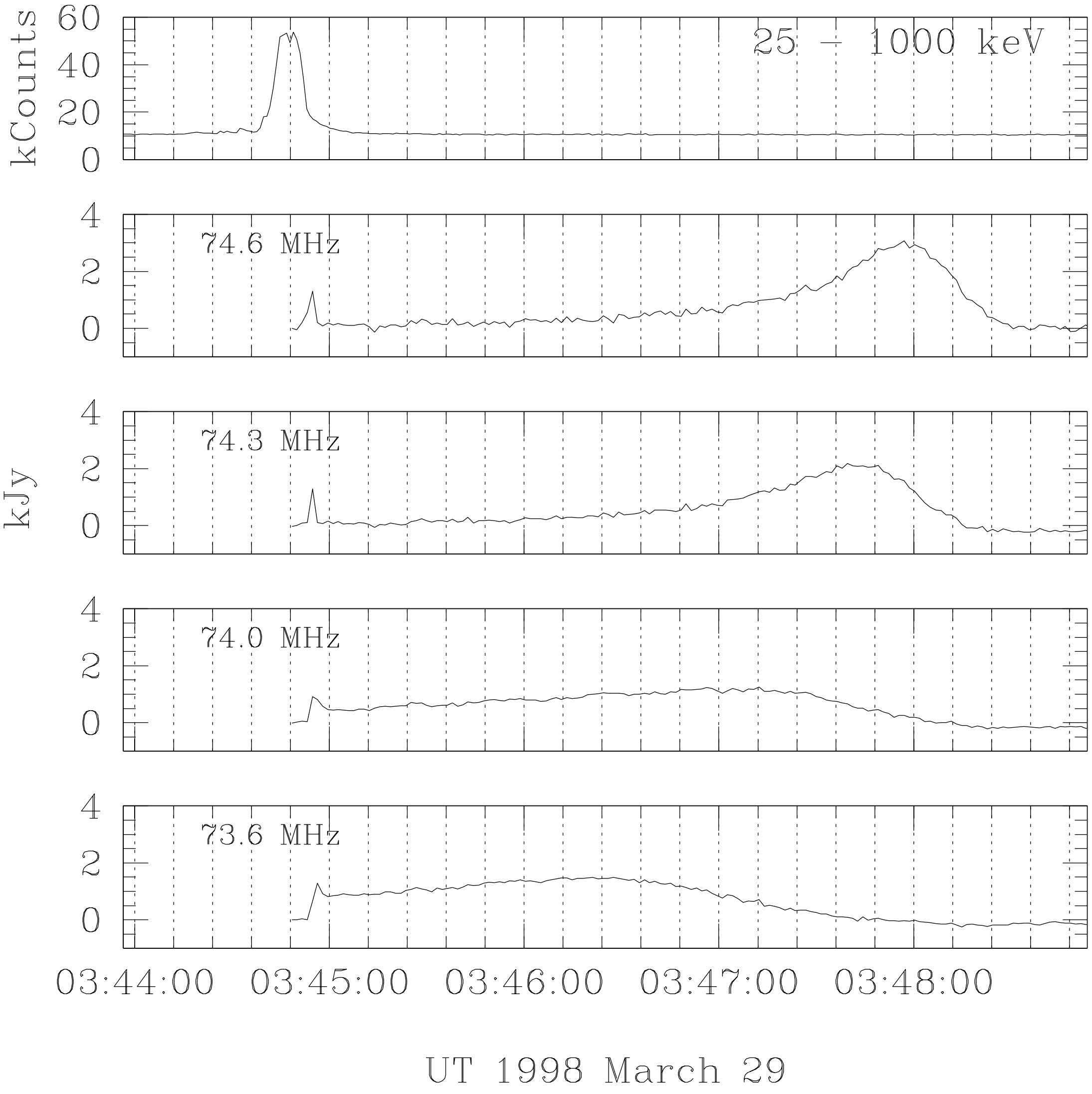

Figure 4.3: Radio and γ-ray lightcurves for GRB980329. The γ-ray curve is the total number of counts in the energy range 25 keV – 1 MeV. The radio flux density scale assumes the GRB happened directly over the array, which it did not. See the discussion in the text for the uncertainty is the absolute calibration.

4.4.2 Description of FLIRT signal

FLIRT began observations toward the end of the peak in γ-ray flux from GRB980329. From 03:44:53 to 03:44:59 there is a spike seen in all 4 channels. The spike appears first in the highest frequency channel and later in each successively lower frequency channel. The delay between signals at 74.6 MHz and 73.6 MHz is 1.4 s. In addition, from 03:45:00 to 03:48:30, there is a much longer event which sweeps slowly from low to high frequency.

Since the signal is sometimes only seen in one channel and the FLIRT channels overlap by several hundred kHz (see Figure 2.8), the signal must be narrow-band. By comparing the signal levels at 3:47:06 UT, it is found that a gaussian spectrum with $\sigma \lesssim 100$ kHz is consistent with the observed signals. If it is assumed that the signal is narrow-band throughout its duration, it is apparent that the signal changes frequency more rapidly both at the beginning of the first peak and the end of the second peak (i.e.the frequency sweep has curvature).

Finally, when the signal is calibrated as if it came from zenith angle 0, it is $\sim 50\%$ brighter at 74.6 MHz than at 73.6 MHz.

4.4.3 Sensitivity to GRB980329

Unfortunately for the FLIRT observation of GRB980329, the position of the GRB occurred 1.3° from the first null of the primary beam pattern. The beam pattern, along with the Inter-Planetary Network triangulation annulus (obtained by observing differences in arrival times for the GRB detected by *SAX* and *Ulysses*), the GCN, LOCBURST and VLA positions are shown in Figure 4.4. As can be seen in the beam map, when the array is commanded to point at the first null, the maximum sensitivity occurs at the local meridian. The reason for this is that with only 2 elements in the E-W direction separated by 4λ, there is a degeneracy between positions with x direction cosines l_0 and l_1 when $4\pi l_0 + n\pi = 4\pi l_1$ (see Equation 2.12). The first null occurs at $l = 0.25$ which is degenerate with $l = 0$ (i.e. at the meridian). Nevertheless, the side lobe shown has some sensitivity at the position of the GRB.

Just how much sensitivity FLIRT had to a source at the position of GRB980329 is uncertain since the beam model is expected to fail near the nulls and predict a deeper null than is actually achieved. According to the beam model, at the VLA position the FLIRT transient had a flux density of $\sim 400 - 600$ kJy, 200 times the flux required to produce the signal were the source at zero hour angle. The rather obvious question is

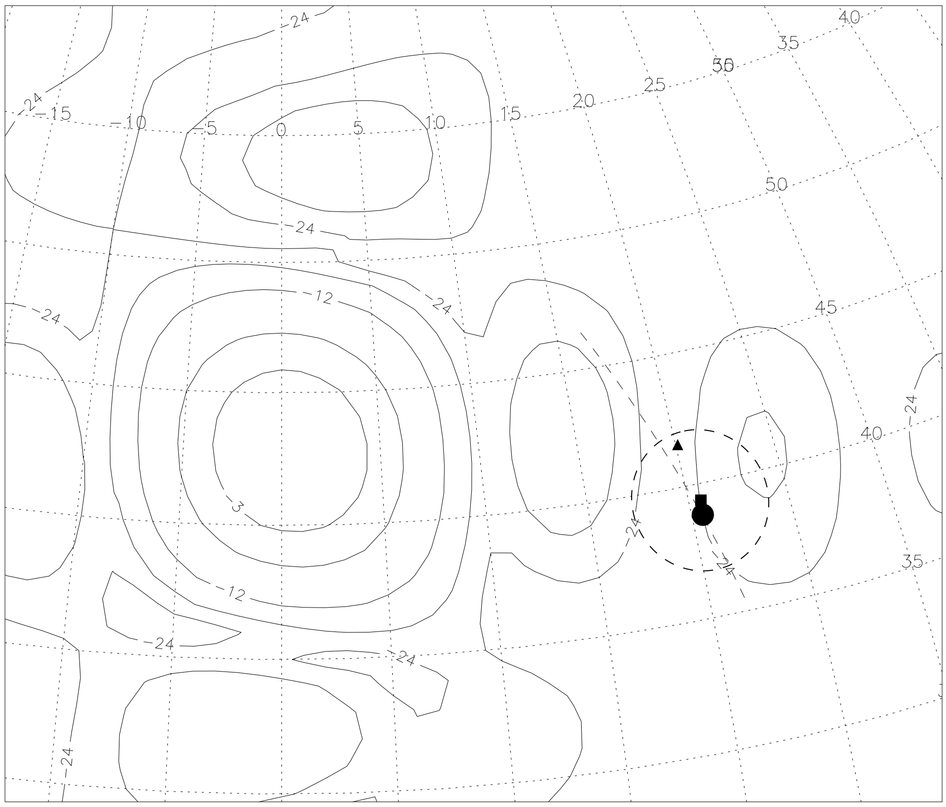

Figure 4.4: Map of the FLIRT beam pattern for GRB980329 as a function of hour angle and declination. Contours are plotted -24,-18,-12,-6 and -3 dB relative to the maximum response capable with the array. The dashed circle outlines the BATSE 68% confidence position. The triangle, square and circle mark the original GCN, final LOCBURST and *SAX*/VLA counterpart positions respectively. The dashed line shows the IPN annulus.

whether the FLIRT array actually possesses that degree of attenuation at the nulls. The ideal test of this would be to point the array at a bright source — Cygnus A would be the source of choice since it is very close in declination to GRB980329 — and monitor the observed signal as the source passed through the null. Unfortunately, the array ceased functioning within a week of this event after a series of thunderstorms. However, since pointing near the null produces a model beam which resembles the model beam for pointing at HA $= 0$, we can use a drift scan, in which Cygnus A drifted over the array to set a limit on the attenuation near the nulls. Doing so yields a limit of $\gtrsim 50$ for the attenuation and a limit for the flux density of $\gtrsim 100 - 150$ kJy. This is very strong for an astronomical signal; the two brightest sources at 74 MHz have flux densities of 15 and 17 kJy.

One question to address is whether the position of the transient at 74 MHz is as well defined as it is in the GHz range where the VLA observed the source. Ionospheric refraction could displace the apparent radio position by as much as $1 - 2'$ at 74 MHz (Erickson 1984), but this contributes less than 5% uncertainty to the flux density, an amount that is negligible considering the uncertainty in the beam model.

4.4.4 Dispersion?

The delay in arrival times observed in the first spike are consistent with a dispersion measure of 66 pc cm^{-3}, which corresponds to a time delay between γ-rays and radio of $\sim$ 50 s (see Appendix A). This time delay implies that the radio event would have preceded the peak in γ-rays by $\sim$ 40 s at the source. The maximum galactic dispersion measure in the direction of this GRB is, according to the model of Taylor and Cordes (1993), 50 pc cm^{-3}, and the DM reaches 90% of this value at a distance of only 4 kpc. There are relatively few pulsars in this part of the sky to constrain the electron density model, so taking an uncertainty of $\sim$ 50% in the DM seems reasonable. Thus, the observed DM is consistent with a galactic origin ($d > 4$ kpc), but we cannot rule out a much more distant extra-galactic origin.

The observed time delays are not the only constraints available in determining if the signal is consistent with what is expected for dispersion. In order to produce the observed signals, the signal must be quite narrow-band. What this implies is that as the signal sweeps down in frequency, the observed power in each channel will simply trace the frequency response, or passband, of the channel.

In Figure 4.5, the spike event is shown, along with a model dispersed pulse with DM $= 66$ pc cm^{-3}. The data shown in Figure 4.5 are calibrated using the scale set by Cygnus A. However, since the signal is clearly narrow-band while Cygnus A is not, the calibration depends on the total bandwidth of each channel. To account for this, the signal from each channel is normalized to the bandwidth of the 73.6 MHz channel.

The model dispersed signal amplitude is scaled to match the 74.6 MHz signal level. In addition, since the GRB occurred near a null, where the beam is expected to have

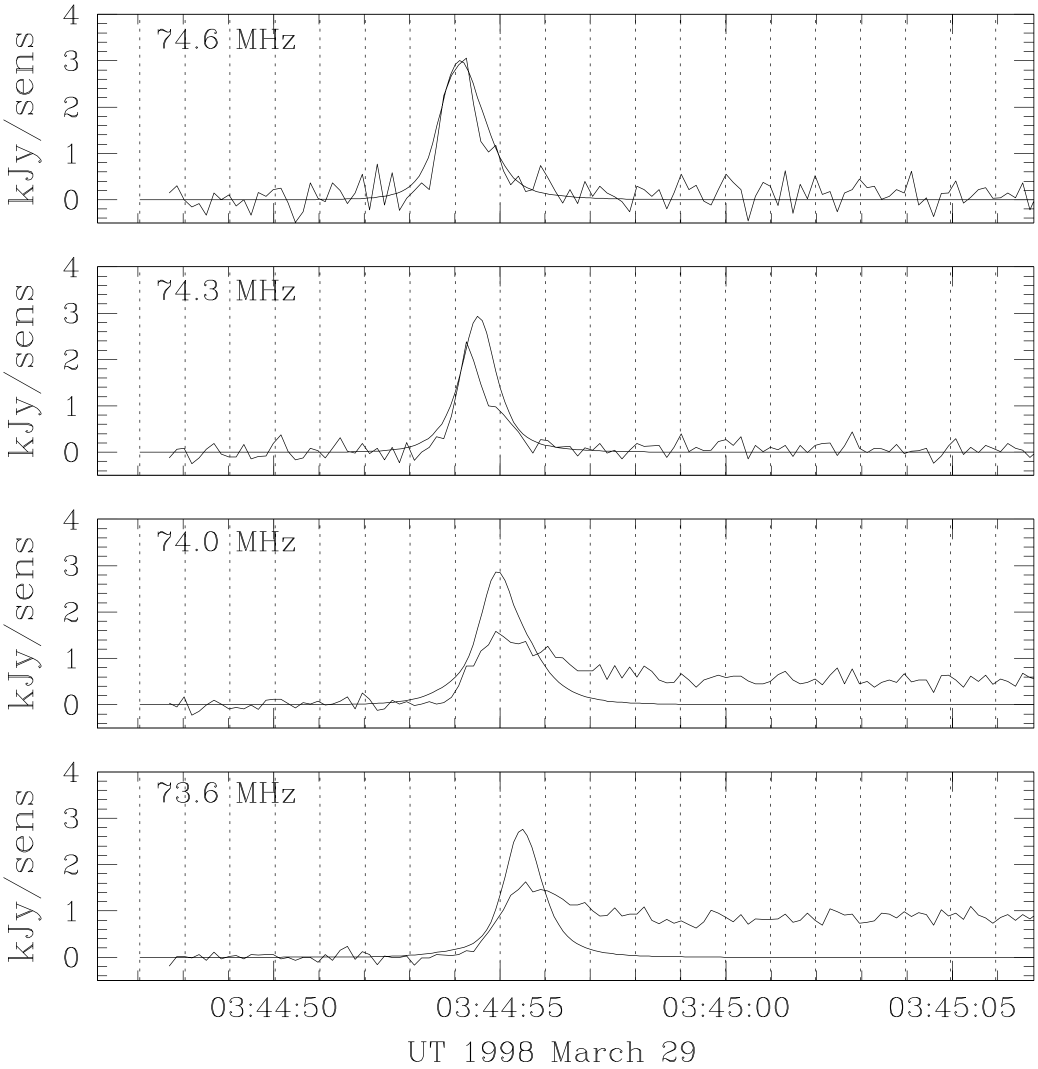

Figure 4.5: The high to low frequency sweep event observed in the GRB980329 data. A model DM 66 pulse is shown along with the calibrated data. There is an overall scale factor ~ 200 omitted from the calibration, assuming the signal came from the position of the *SAX* burst.

some frequency dependence, the model signals at frequency ν are scaled by

$$f(l) \propto \left(\frac{\sin(4\pi l\nu/\nu_0)}{\sin((\pi/2)l\nu/\nu_0)} \right)^2 \tag{4.1}$$

where ν is the center frequency of a channel, $\nu_0 = 74$ MHz, $l = 0.272$ and all channels are compared to the 74.6 MHz channel.

As seen in Figure 4.5, the observed signal is *not* particularly consistent with the simple model of a single narrow-band signal produced by dispersion. The signals in the 73.6 MHz and 74.0 MHz are of longer duration than expected and of lower amplitude than the signal in the 74.6 MHz channel. This argues against an astronomical interpretation of the spike.

Dispersion measure at high z

Even if dispersion is accepted as the source of the frequency sweep observed in the radio transient, one might worry that a DM ~ 66 would be too small to be consistent with a transient from another galaxy. We now show that the dispersion measure from the host galaxy itself can be minimized if the host galaxy is at high redshift. If the radiation from a source at redshift z is emitted at a frequency ν_s, an observer local to, but just outside, that galaxy would see the radiation after a dispersion delay of

$$\Delta t_s = \frac{\mathrm{DM}_s}{\alpha_d \nu_s^2} \tag{4.2}$$

with DM_s the dispersion measure local to the host galaxy. However, two events separated by a time Δt_s at a redshift z are observed on Earth to be separated by a time $\Delta t_o = (1+z)\Delta t_s$. Similarly, the observed frequency is given by $\nu_o = \nu_s/(1+z)$. Inserting expressions for Δt_s and ν_s into Equation 4.2 gives

$$\Delta t_o = \frac{\mathrm{DM}_s}{\alpha_d \nu_o^2 (1+z)}. \tag{4.3}$$

Thus, the observed DM is a factor $1+z$ lower than an observer local to the galaxy would measure. If GRB980329 is at a redshift of $z \sim 5$, then the effective dispersion measure observed due to the host is decreased by a factor of 6. Even a typical dispersion measure of DM ~ 50 in the host galaxy does not provide a serious constraint for the DM of the observed radio transient.

However, the radiation must also be dispersed by the intergalactic plasma (IGP) between the GRB and Earth. As stated in §1.6.1 Palmer (1993) estimates that the

DM due to the IGP is:

$$\mathrm{DM_{IGP}} = 2.64 \times 10^4 \Omega_{IGP} \frac{h}{q_0}[(1+2q_0 z)^{1/2} - 1] \text{ pc cm}^{-3} \tag{4.4}$$

where $\Omega_{\rm IGP}$ is the density of the ionized intergalactic plasma in units of the closure density, h is the Hubble constant $H_0/(100\text{km s}^{-1}\ \text{Mpc}^{-1})$ and q_0 is the acceleration parameter.

The total density of the intergalactic medium is expected to be ~ 0.01 of the closure density. To calculate the amount of dispersion, however, it is the ionized portion that is of concern. The Gunn-Peterson effect (Gunn and Peterson 1965) predicts that resonant Lyα scattering by neutral hydrogen should produce a broad trough in the spectra of high redshift quasars. The absence of this effect has been taken as strong evidence that the intergalactic medium is largely ionized at redshifts $z \lesssim 5$ (see Giroux and Shapiro (1998) for a review and models), so that $\Omega_{\rm IGM} \approx \Omega_{\rm IGP}$. So, taking $\Omega_{\rm IGP} = 0.01$, $h = 0.7$ and $q_0 = 0.5$, Equation 4.4 becomes:

$$\mathrm{DM_{IGP}} = 3.7 \times 10^2[(1+z)^{1/2} - 1] \text{ pc cm}^{-3} \tag{4.5}$$

For $z \ll 1$, this gives $\mathrm{DM_{IGP}} \approx 200 \times z$ pc cm^{-3}. For a redshift of 5, $\mathrm{DM_{IGP}} \approx 540$ pc cm^{-3}. This large DM is clearly inconsistent with the low DM observed in the radio transient, even allowing for an order of magnitude uncertainty in $\Omega_{\rm IGP}$.

4.4.5 Scattering effects

In an attempt to explain the somewhat bizarre upward drift in frequency observed in the second pulse, it is worthwhile to investigate other interstellar processes which could produce frequency dependent effects. One possibility is interstellar scattering, in which variations in free electron density result in a combination of geometric and physical optics effects.

Goodman (1997) calculates the relevant interstellar scattering parameters appropriate to cosmological GRBs. When radio sources are observed through the turbulent interstellar medium, localized intensity fluctuations may appear in the time-frequency plane. These fluctuations can be analyzed as if they are caused by a thin "phase screen" which introduces random phase delays into the propagating signal. The timescale over which intensity fluctuations should be observed, $t_{\rm dc}$, is given by

$$t_{\rm dc} = 3.1\nu_{10}^{6/5}(SM_{-3.5})^{-3.5}\left(\frac{v_\perp}{30 \text{ km s}^{-1}}\right)^{-1} \text{hr} \tag{4.6}$$

where ν_{10} is the observed frequency in units of 10 GHz, $SM_{-3.5}$ is the scattering measure scaled to the value near the Sun of $10^{-3.5}$ $\mathrm{m}^{-20/3}$ and $v_{\perp}$ is the relative transverse velocity of the source across the phase screen that causes the fluctuations.

Likewise, correlated intensity fluctuations occur over a limited bandwidth, referred to as the decorrelation bandwidth, $\Delta\nu_{\mathrm{dc}}$ given by

$$\Delta\nu_{\mathrm{dc}} = 7.6\nu_{10}^{22/5}(SM_{-3.5})^{-6.5}d_{\mathrm{scr,kpc}}^{-1}\mathrm{GHz} \tag{4.7}$$

where $d_{\mathrm{scr,kpc}}^{-1}$ is the distance to the phase screen causing the scintillation. For observations at 74 MHz, $t_{dc} \sim 30$ s and $\Delta\nu_{\mathrm{dc}} \sim 3$ Hz. In the ~ 0.5 MHz of a FLIRT channel, scintillation produces roughly 10^5 intensity fluctuations with typical time-scales of 30 seconds. Thus, in any observation, FLIRT averages over many such spectral features so that they should be unobservable. It follows that the effects of interstellar scintillation are negligible and cannot explain the spectrum of the radio transient.

If scattering effects cannot produce the observed signal, one wonders if the signal could be produced at the host itself. The narrow-band nature of the signal and the frequency drift with time are not easy to explain. However, in §4.4.8, solar data showing at least some of the required features are displayed.

4.4.6 Probability of coincidence

We would like to estimate the *a posteori* likelihood of this transient being associated with GRB980329. Such a calculation should be regarded with caution as we are attempting to calculate the probability of an event occurring after it has already happened. Nevertheless, it is useful to quantify our "surprise" at having detected such an odd transient near the time of a GRB. Given that only one such signal was detected in the FLIRT observations, we want to calculate the probability that it satisfied the following requirements:

1. it occurred in a section of data expected if the association between radio transient and GRB is real, and

2. it occurred in data for a bright GRB.

To calculate the first probability, we want to calculate the likelihood that the dispersion of the first pulse predicts a time delay back to infinite frequency (i.e. back to the time of γ-ray emission) which is reasonable. To do so, we use a probability defined as:

$$P = \frac{\min(|\Delta t_{\mathrm{obs}} - \Delta t_{\mathrm{DM}}|, T)}{T} \tag{4.8}$$

where P is the probability of a chance coincidence, $\Delta t_{\rm obs}$ is the observed delay between the GRB and the dispersed radio transient, $\Delta t_{\rm DM}$ is the dispersion delay expected between the GRB and the radio transient given the dispersion delay measured in the radio. T is the length of the data file. Note that Equation 4.8 behaves reasonably in the limits $\Delta t_{\rm obs} - \Delta t_{\rm DM} = 0$ or T. One could argue for corrections to this, of order unity, to account for a belief that the GRB and radio transient look-back time need not exactly coincide or for forcing $P = 1$ for $\Delta t_{\rm obs} - \Delta t_{\rm DM} \approx T/2$ or to give a non-linear dependence on the numerator. Given the information available, this seems like too much fine-tuning. The time delay between the peak of the GRB and the peak in the 74.6 MHz channel is $\Delta t_{\rm obs} = 8$ s. The dispersion measure DM $= 66$ pc cm^{-3} corresponds to a $\Delta t_{\rm DM} = 50$ s (see Appendix A). The total length of the observation is $T = 2530$ s. Thus, $P \sim 0.02$, meaning that there is $\sim 2\%$ chance of randomly placing this radio transient as close or closer to the GRB as observed.

There is no particular reason for singling GRB980329 alone out of the GRBs which were observed by FLIRT. However, it is fairly bright, falling in the top 5% of the BATSE peak flux distribution and in the top 20% of those GRBs followed up by FLIRT. The flux density limits for all of these bursts are a few hundred kJy, so they are a relatively uniform sample. Thus, the probability of randomly seeing a radio transient associated with a GRB as bright as GRB980329 or brighter is $\sim 20\%$.

The probability of finding a radio event associated with a burst in the top 20% of the observed peak flux distribution is $\sim 0.02 \times 0.2 \approx 0.004$. This is a semi-quantitative argument to justify our surprise at finding such an odd signal nearly coincident in time with a bright GRB. The radio transient event is rare (the only one like it in the FLIRT data set) and it occurs near the time of a bright GRB. Nevertheless, the probability of a random coincidence is roughly one in two hundred and not entirely implausible.

4.4.7 Where did it come from?

Although it is not possible to rule out a terrestrial signal, we can rule out various astronomical objects as the source of the radio transient. The sun was 20° or more below the horizon during the entire observation, so it is easily eliminated as the source. Jupiter and the moon were both below the horizon. (Jupiter is unlikely to produce such signals anyway because Jovian radio bursts have an extremely sharp frequency cutoff at 40 MHz (Kraus 1986)). The position of the moon was checked to rule out possible reflections of solar bursts from the moon.

The second, longer pulse is detected in the two highest frequency channels of one of the other subarrays. The signal is very weak, roughly equal to the RMS at the 50 ms timescale and is only detectable due to its long duration. The first, shorter pulse was not detected. This is not particularly surprising since the expected peak signal strength would be about the RMS on the 50 ms timescale and the first pulse is too short to benefit from an integration longer than ~ 1 s. Since this subarray was never properly phased, calibrating any signal from it is difficult. However, based on the observed signal strength of the ubiquitous square wave RFI, that is seen in both subarrays, it is possible to say that the source of the transient is *not* the same as the source of the regular RFI. This is not particularly helpful, however, as there are likely to be many other sources of RFI near the array.

4.4.8 The solar analogy

As claimed in §4.4.5, perhaps the observed temporal and frequency structure observed in the radio transient coincident with GRB980329 was generated at the source of the GRB. In this section, data on a solar flare are presented which help support the claim that narrow-band, rapidly changing radio signals can be observed from a natural source.

The radio transient shown in Figure 4.6 is a solar radio burst. Data from the WIND satellite show that there was a weak Type III noise storm going on throughout the day and a more intense Type III burst around 19:00 UT (M. Kaiser, NASA GSFC, personal communication). The emission in a Type III storm is caused by plasma oscillations (Langmuir waves) set up by an electron jet traveling rapidly ($\sim c/3$) upward through the solar corona. Oscillations in the magnetic field lines are converted into electromagnetic radiation at the local plasma frequency. Since the plasma frequency is proportional to the square root of electron density, it decreases with height above the solar photosphere thereby causing the observed radiation to sweep downward in frequency. Typically, Type III bursts sweep from high to low frequencies at a rate of ~ 100 MHz/s, much too fast to be discerned using the FLIRT spectrometer (McLean 1985).

The density of free electrons where the 74 MHz emission is taking place is 6.8×10^7 cm^{-3}, corresponding to a height above the solar photosphere of 0.2 $R_\odot$ (Kraus 1986). Figure 4.7 shows an expanded section of the event shown in Figure 4.6, in which two features are seen to drift at 7 ± 2 MHz/s. Such features could have been a substantial problem for FLIRT. However, very few FLIRT observations had noticeable

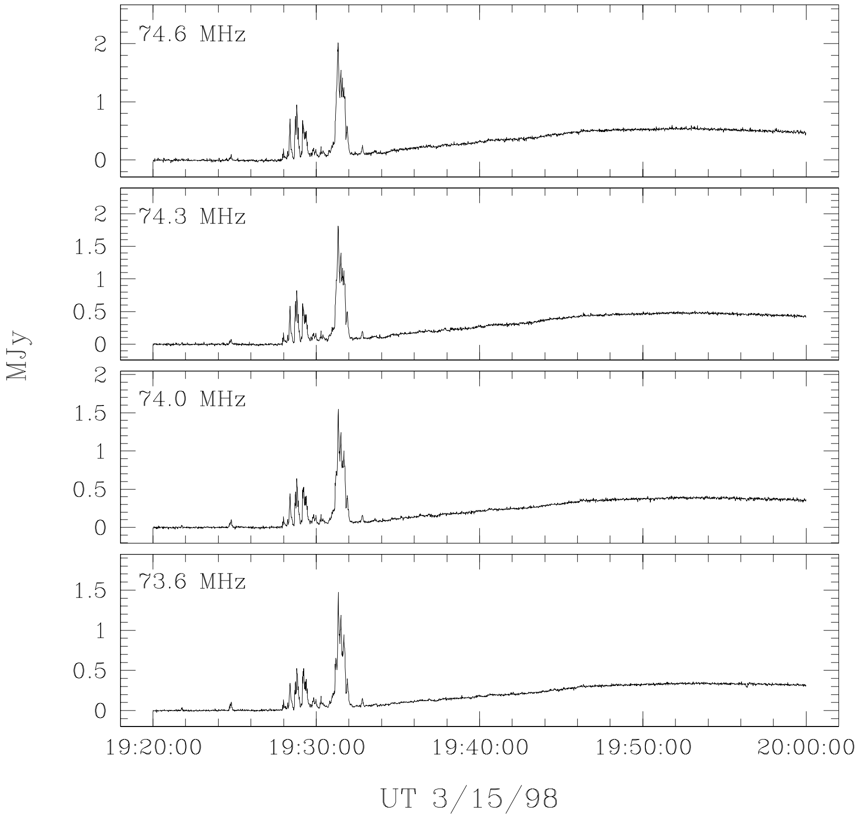

Figure 4.6: Solar radio burst associated with a solar flare on 1998 March 15.

solar contamination and only this solar flare data had drifting bursts.

More important for the discussion in §4.4 are transients in which very steep spectra are found. One such case is found in Figure 4.8. Due to the small fractional separation of the FLIRT passbands in frequency, as well as their significant overlap of several hundred kHz (see Figure 2.8), any substantial difference in signals between frequency channels implies a very steep spectrum. To show this more clearly, in Figure 4.9 the ratio of the 73.6 MHz channel to the 74.6 MHz channel is plotted as a function of spectral index for a power law spectrum. To explain the observed variation among the channels in Figure 4.8, the spectral index would have to be an unphysical $70-100$. A simpler explanation is to assume the transient has narrow-band structure.

Narrow-band, time-dependent emission is in fact seen in solar radiation. Spikes of millisecond duration have been observed with instantaneous bandwidths of 0.5 –

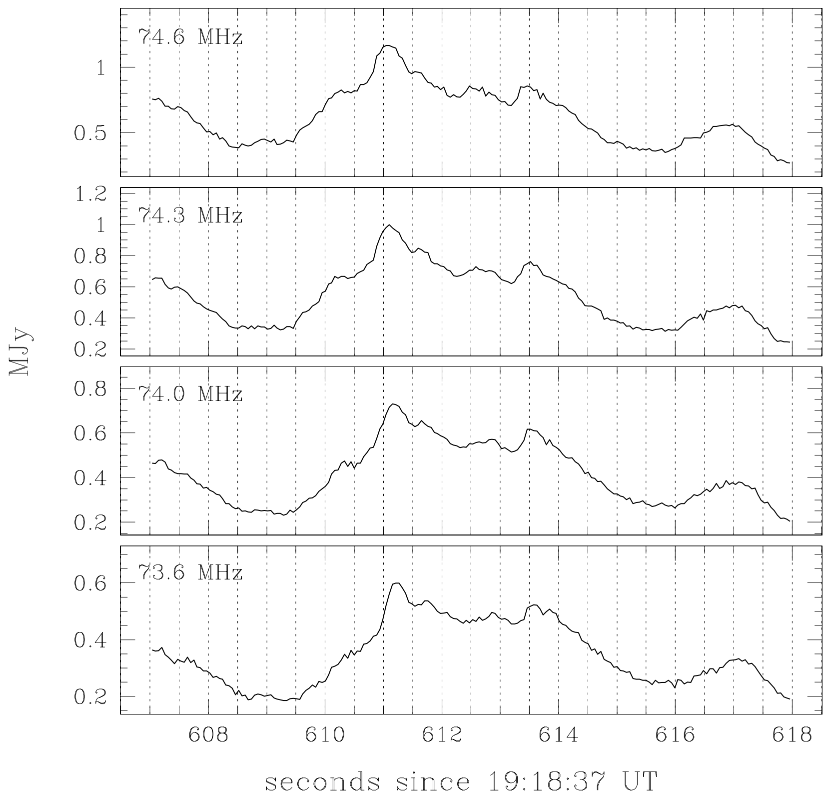

Figure 4.7: Rapidly drifting pulses in the solar burst in Figure 4.6. The features at 611 and 613.5 seconds both drift to lower frequency with time.

15 MHz, with a typical value of $\Delta\nu/\nu \sim 1.5\%$ (Benz 1987).

In addition to producing narrow-band signals, the Sun also produces transients which drift in frequency with time. As already discussed, Type III solar bursts drift rapidly from high to low frequencies. Type II bursts behave similarly, but drift ~ 100 times more slowly. Furthermore, not all solar bursts drift from high to low frequencies. In some Type III storms, pairs of drifting bursts are seen with a narrow instantaneous bandwidth, $\Delta\nu \sim 0.2 - 2$ MHz, and although both forward and reverse drift pairs are known to exist, reverse drift pairs (in which the frequency drift is from low to high frequency) are more common (Kai *et al.* 1985). An upward drift in frequency is also seen in inverted U bursts in which the frequency first decreases then increases again. This behavior is a result of emission from material first passing through a

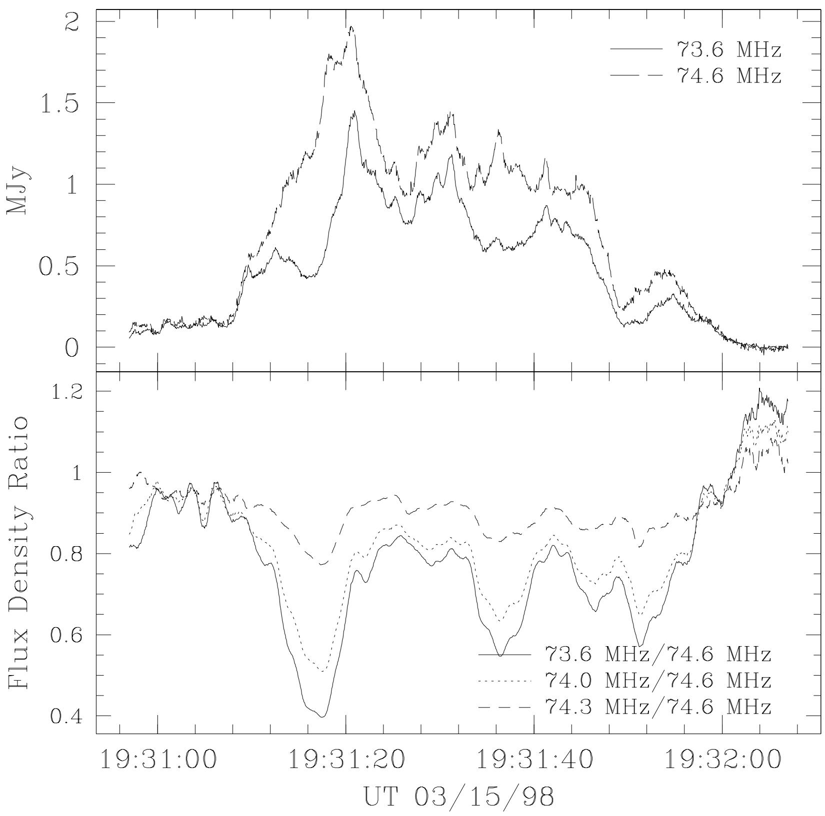

Figure 4.8: A very steep spectrum portion of the transient in Figure 4.6. The upper panel shows the high and low frequency FLIRT channels which differ markedly in several places. The lower panel displays the ratio of the three low frequency channels to the high frequency channel.

region in which N_e is decreasing then one in which it is increasing, such as along a closed magnetic field line.

The environments in solar flares and GRBs are likely to be very different, but perhaps similar narrow-band features with rapid frequency variability could be seen in radio transients associated with GRBs. This seems unlikely to be the case with the radio transient observed near the time of GRB980329, however, as one would still expect to see clear signs of dispersion in addition to any spectral changes at the source.

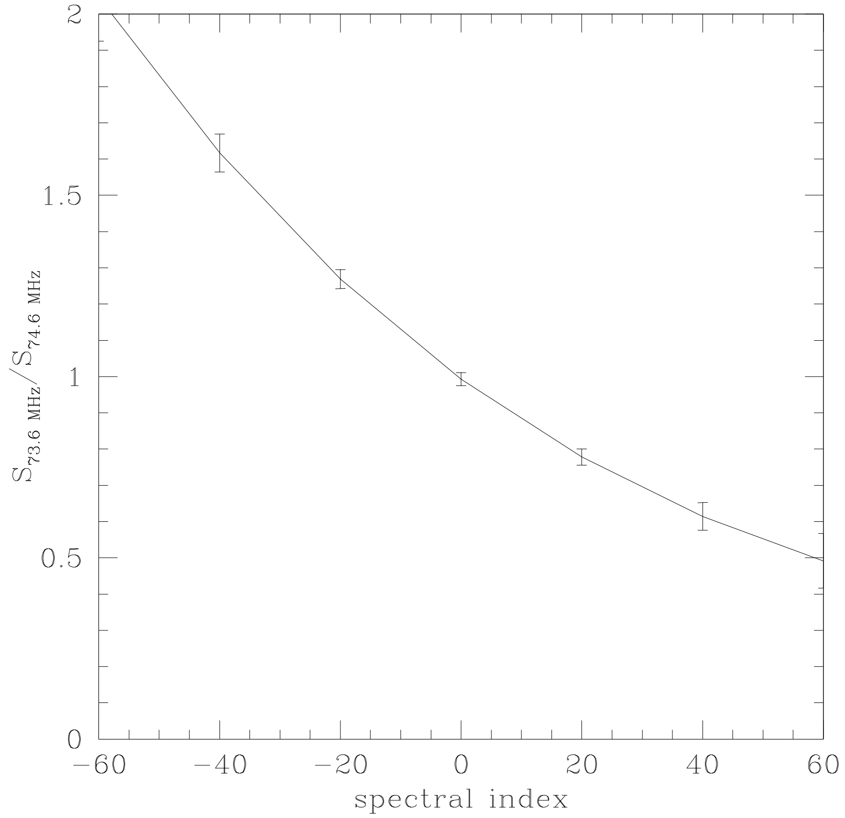

Figure 4.9: The ratio of the 73.6 MHz to 74.6 MHz calibrated flux densities versus spectral index, ν ($S_\nu \propto \nu^\alpha$).

4.4.9 GRB980329: conclusions

The case of the radio transient's association with GRB980329 is far from clear. Here we summarize the arguments for and against an association between GRB980329 and the radio transient observed by FLIRT.

The following arguments can be made in favor of the association:

- the observed signal is unique in the FLIRT data set,
- the Sun and other known astronomical objects can be ruled out as a source,
- the frequency drift of the first pulse could result from a DM of ~ 66 pc cm^{-3},
- *a posteori* arguments suggest a small probability of chance coincidence between

the radio transient and a GRB as bright as GRB980329, and

Despite these arguments, which are moderately convincing, there are strong reasons for doubting the association, including:

- the narrow-band nature of the signal and its temporal structure are most easily explained as terrestrial interference,
- the second pulse is difficult to explain without invoking spectral evolution at the source,
- allowing spectral evolution at the source makes the apparent DM less convincing, and
- the observed DM is too low for a cosmological interpretation unless the ionized intergalactic medium is much less dense than expected.

The large flux density of $\sim 400 - 600$ kJy is an order of magnitude brighter than the brightest 74 MHz source, the radio loud galaxy Cygnus A. This is not terribly restrictive since GRBs can be much brighter than steady sources on the sky (Fishman and Meegan 1995). Thus the flux density cannot, on its own, argue for or against an association.

The main argument for the association is the apparent dispersion measure of the first pulse and the plausible lookback time it implies. The main argument against the association is the appearance of the second pulse which makes the entire event most easily explained as some sort of RFI. The conservative approach is to conclude the event is likely to be terrestrial interference and let observations of from a future experiment settle the question.

4.5 Limits on 74 MHz Emission from 32 GRBs

4.5.1 Interpretation of Limits

In the absence of a positive detection of a prompt counterpart to a GRB, the significance of the non-detections must be assessed. To do so, flux density limits for all observations must be calculated. Obviously these limits are uncertain by as much as $\sim 50\%$ from the calibration of the array. However, a more serious uncertainty in a flux limit comes from the uncertainty in the position of the GRB in the FLIRT beam (cf. Figure 4.2 and 4.4). The approach here is to quote the flux density limit as if the GRB did occur at the final BATSE LOCBURST position. Another approach would be to take the median flux density limit in the BATSE error circle, but the two approaches give similar results. The limits are to be interpreted as the approximate flux density at which a radio counterpart would be detected with 70% efficiency (see Figure 3.7) if it occurred at the LOCBURST position. Typically, the median limit for positions within the BATSE 1σ error circle is comparable to the limit at the LOCBURST position. Thus, approximately $70\% \times 0.5 \times 0.68 \approx 25\%$ of the time, a burst at the quoted limits would be detected.

4.5.2 Calculation of limits

To calculate flux density limits for the observed GRBs, a standard limit of 400 Jy for a burst directly over the array was assumed. If in searching for dispersed transients particularly bad RFI increased the RMS noise level too much and artificial bursts were not reliably detected, this level was increased by a factor of 2. Similarly, if the data were particularly smooth and artificial bursts were easily detected, the limit was decreased to 200 Jy. For data in which no artificial bursts were added prior to searching, these adjustments were done based on the RMS noise level.

To convert the overhead flux density limits to limits at the position of the GRB, the sensitivity of the FLIRT array was calculated according to the beam model presented in §2.3.1. The resulting limits are presented in Table 4.2. A sensitivity was calculated for each GRB at both the original GCN and the final LOCBURST position. The latter limit should be regarded as a typical limit in the 1σ BATSE error circle.

The limits for GRB971208 should be treated with some caution as the GRB was an 800 second long, very smooth fast-rise, exponential decay event. If a radio transient associated with this GRB had similar properties, it would have to be several times the normal limit to be distinguished from the background.

Inspection of Table 4.2 will reveal that BATSE triggers 6488 and 6399 have been excluded. The reason is that both data files are heavily contaminated by many non-dispersed transients, presumably of solar origin.

4.5.3 Discussion of limits

In the early stages of the experiment, it was hoped that FLIRT's ultimate sensitivity would be ~ 100 Jy for a burst which occurred directly over the array. As mentioned

Table 4.2: Radio flux density limits.

BATSE trigger	F_{GCN} (kJy)	F_{loc} (kJy)	Δt_{GRB} [a] (s)	Δt_{pt} [b] (s)	Δt_{F} [c] (s)	$\mathrm{DM}_{\Delta t_{\mathrm{F}}}$ [d] (pc cm^{-3})	$\mathrm{DM}_{(l,b)}$ [e] (pc cm^{-3})
6358	25	110	0.11	0	588	440	20
6366	76	49	250	50	626	460	20
6368	42	750	0.25	0	627	470	20
6385	8	0.8	4	3	9	7	40
6390	19 000	320 000	35	33	345	250	50
6396	1.2	3.7	70	65	8	6	160
6400	100	44 000	17	15	11	8	270
6401	35	480	2	1	8	6	20
6409	27	4 300	16	12	596	440	20
6427	25	400	0.25	0	305	220	80
6437	35	16	12	8	7	5	10
6439	7.3	140	0.5	0	619	460	130
6443	0.2	310	3	1	9	7	20
6455	83	110	28	25	656	490	20
6472	12	320	280	280	9	6	20
6523	11	73	40	30	8	6	140
6526	270	190	800	800	14	10	60
6527	61	550	2	1	9	6	20
6529	300	620	15	15	585	430	20
6540	5.5	78 000	0.04	0	9	6	10
6545	2.6	18	30	17	10	7	30
6547	0.8	1 100	0.04	0	629	470	20
6552	34	11	20	18	8	6	30
6560	210	430	52	52	9	6	100
6562	22	910	1	1	760	570	20
6577	82	170	30	28	7	5	50
6579	4.5	4.7	3.5	2	11	8	10
6581	56	190	270	265	10	7	40
6641	4.8	7.7	0.25	0	8	6	70
6643	28	18 000	0.3	0	8	6	20
6665	540	180	55	42	9	7	40
6666	13	19	8	5	9	7	30

[a] Estimated duration of GRB, from Huntsville GRB reports or GCN lightcurves, available at http://lheawww.gsfc.nasa.gov/docs/gamcosray/legr/bacodine/batse_grbs.html.
[b] Duration of GRB after the trigger, estimated from GCN lightcurves.
[c] Delay between GRB trigger and beginning of FLIRT observation.
[d] Minimum observable DM based on time delay from trigger.
[e] Estimated DM through galaxy for LOCBURST (l,b) position.

in the preceding section, the standard limit was 4 times this. The main reason for this, as discussed in §2.3.3, was that we had assumed $T_{sys} \sim 10^3$ K, when it was, in fact, closer to $T_{sys} \sim 10^4$ K. However, some of the sensitivity was recovered by pushing the search down to the RMS noise level.

The problem was compounded since no GRBs occurred close to the array zenith; the closest that a GRB was to the array zenith was 17°. In addition, as can be seen in Table 4.2, the change from the original GCN coordinates to the final LOCBURST coordinates substantially lowered the sensitivity of most observations. Had all 4 subarrays been functional as originally planned, FLIRT would have better covered the GCN error circle minimizing this problem.

Although the FLIRT limits are higher than expected, when put in proper context they are still reasonable. Figure 4.10 shows the limits produced by FLIRT and other prompt GRB counterpart search experiments. The data are plotted twice. In the lefthand figure, two Band model (Band *et al.* 1993) spectra are shown with extrapolations from γ-rays to optical and radio. There is a considerable range over which the extrapolation could fall and there is no particular reason for expecting the power law behavior to continue over so many orders of magnitude in frequency. Nevertheless, it shows that current experiments are probing interesting parameter space. The righthand plot shows the νF_ν (power) spectra of two synchrotron sources, the Crab nebula and the BL Lac object Markarian 421. Two copies of both spectra are plotted and offset so that they span the range of energy fluxes seen in the sample of GRBs observed by FLIRT. When viewed in this manner, for synchrotron sources, FLIRT is as sensitive as BATSE. One might expect, however, that low frequencies are attenuated by synchrotron self-absorption. Nevertheless, this is a reasonable way to compare the FLIRT limits with those of other experiments at other frequencies.

4.6 Conclusion

The FLIRT experiment is just one of several searches for prompt emission from GRBs which was carried out over the last several years. This is an exciting time in GRB science and long wavelength studies still hold the promise of helping to unravel the mysteries of GRBs. The results of previous radio experiments were discussed in §1.6.3 while the FLIRT results were discussed in the previous section, so there is no need to review them here.

Instead, it is appropriate to look to the future of prompt GRB followup experi-

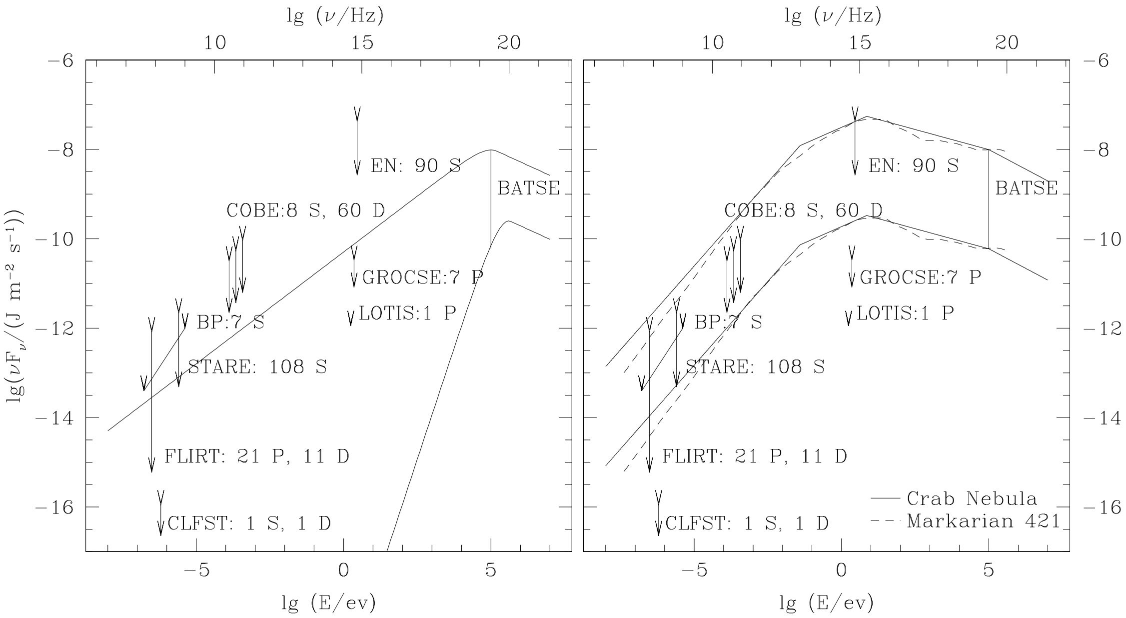

Figure 4.10: Comparison between limits on prompt emission from GRBs at radio and optical wavelengths with the range of GRB fluxes observed in the FLIRT experiment. In the left panel, the curves show Band (Band *et al.* 1993) model GRB spectra with break energy $E_0 = 200$ keV, high energy spectral index $\beta = -2.3$ and low energy spectral indices -1.5 and 0 (see Equation 1.1) to give the range of extrapolations from γ-rays to optical and radio. In the right panel, the curves show the spectra of the Crab nebula (Hillas *et al.* 1998) and Markarian 421 (Makino *et al.* 1987), which are both synchrotron sources. In both panels, the number of GRBs observed by followup experiments is given as a number next to the name of the experiment followed by S, P or D for simultaneous, prompt or delayed followup respectively. The division between prompt and delayed is at $\sim$ 20 seconds. Data for experiments were taken from the following sources: CLFST, Dessenne *et al.* (1996); STARE, Katz (1997); BP, Benz and Paesold (1998); COBE, Jackson *et al.* (1998); EN, Hudec *et al.* (1998); GROSCE, Lee *et al.* (1997); and LOTIS, Park *et al.* (1997).

ments. It is constructive to ask how an experiment could place better radio flux limits than FLIRT.

FLIRT had a very rapid response; the only way to do better than FLIRT's response times of ~ 10 s, would be to monitor the position of a GRB before it occurred, which is only possible with a lower sensitivity large area beam (such as that used for STARE). Existing radio telescopes are incapable of slewing to positions rapidly, so this is a firm constraint. It is unlikely that an antenna more sensitive than FLIRT will be able to respond as quickly to a large sample of GRBs.

FLIRT was sensitive. However, building a system with a receiver temperature $T_{\rm rec} \sim 1000$ K could increase the sensitivity of an array like FLIRT by about an order of magnitude in cold parts of the sky. Using a larger array than the one used for FLIRT limits the area of sky that can be searched, which is incompatible with the large BACODINE error circles. Covering a larger area on the sky at similar sensitivity to what FLIRT achieved, however, would be a feasible improvement.

FLIRT has demonstrated the efficacy of using dispersion as an RFI-rejection scheme. This could be improved by use of a system of narrow-band channels; the broad channels used in FLIRT were heavily contaminated by numerous narrow-band signals, which made their effect difficult to remove. An alternative to using a total power detection scheme would be to use a system in which the radio signal is mixed down to baseband and the electric field vector is sampled (Stairs 1998). Such a system would provide excellent spectral coverage over a finite bandwidth and could be used to remove both narrow-band RFI and the effects of dispersion.

The use of a second, geographically isolated antenna could provide an additional RFI rejection system. However, FLIRT used an existing array and construction of a second array would have been impractical.

FLIRT was a low-cost system. Searches for new phenomena are unlikely to succeed and are given relatively low priority in science budgets. It is necessary to keep the costs of such projects to a minimum while maximizing the return. Without the construction of specialized equipment, at substantial cost, it is difficult to out-perform FLIRT.

If a new source of rapid GRB coordinates would become available, small gains could be achieved in that a smaller beam, such as would be produced by the full FLIRT array, could be used. The rapid response, however, still limits one to use of a relatively small array.

The combination of poor GRB positions, the relatively low event rate and requirements for a rapid response make current GRB counterpart searches quite challenging. One must conclude than, that FLIRT was both an important step forward and nearly at the limit of what is feasible in terms of rapid response, sensitivity and sky coverage.

Appendix A

Dispersion

A.1 Derivation of dispersion measure

The goal here is to understand dispersion of electromagnetic radiation traveling through the interstellar medium (ISM). The ISM is a plasma, mostly ionized hydrogen, consisting of free electrons and largely immobile positive ions. The propagation of electromagnetic waves through this plasma produces a time delay between the arrival of high and low frequency radiation. This is a well-known effect worked out in detail in many textbooks; it is included here for completeness.

To find the dispersion relation for a plasma, it is necessary to derive the speed at which radiation propagates through this medium. As in Rybicki and Lightman (1979) , begin with Maxwell's equations:

$$\vec{\nabla} \cdot \vec{E} = \rho \tag{A.1}$$

$$\vec{\nabla} \times \vec{E} = \frac{-1}{c}\frac{\partial \vec{B}}{\partial t} \tag{A.2}$$

$$\vec{\nabla} \cdot \vec{B} = 0 \tag{A.3}$$

$$\vec{\nabla} \times \vec{B} = \frac{4\pi}{c}\vec{J} + \frac{1}{c}\frac{\partial \vec{E}}{\partial t}. \tag{A.4}$$

The spacetime dependence of $\exp(i(\vec{k} \cdot \vec{x} - \omega t))$ is assumed for both $\vec{E}$ and $\vec{B}$ so that all the derivatives in Equations A.1 — A.4 may be eliminated. Thus, $\partial/\partial t \rightarrow -i\omega$, $\vec{\nabla}\times \rightarrow i\vec{k}\times$, and $\vec{\nabla}\cdot \rightarrow i\vec{k}\cdot$.

Since the plasma is electrically neutral overall, the source term, ρ, in Equation A.1 is neglected. However, the current density in the plasma, $\vec{J}$, must be calculated. To do so, first note that the positive charges are effectively immobile due to their mass, so only the electrons need to be considered. Applying Newton's Second Law to an electron, and ignoring the magnetic force, gives

$$m\vec{a} = -e\vec{E}. \tag{A.5}$$

Assuming that an electron's position is $\vec{x} = \vec{x_0}exp(-i\omega t)$, gives its velocity,

$$\vec{v} = -i\omega\vec{x}, \tag{A.6}$$

and its acceleration,

$$\vec{a} = -\omega^2\vec{x}. \tag{A.7}$$

Putting Equation A.7 into Equation A.5, yields

$$-\omega^2 m\vec{x} = -e\vec{E}. \tag{A.8}$$

Now assume that the plasma is ohmic so that

$$\vec{J} = \sigma\vec{E}, \tag{A.9}$$

where the current is

$$\vec{J} = -ne\vec{v} \tag{A.10}$$

with n the density of free electrons, $-e$ their charge, and $\vec{v}$ their velocity. Using Equations A.6 and A.8 in Equation A.10 gives:

$$\vec{J} = \frac{ine^2}{m\omega}\vec{E}, \tag{A.11}$$

so that

$$\sigma = \frac{ine^2}{m\omega}. \tag{A.12}$$

Equations A.2 and A.4 now give

$$i\vec{k} \times \vec{E} = \frac{i\omega}{c}\vec{B} \tag{A.13}$$

and

$$i\vec{k} \times \vec{B} = (\frac{4\pi\sigma}{c} - \frac{i\omega}{c})\vec{E}. \tag{A.14}$$

Taking $\vec{k}\times$ Equation A.13 and inserting Equation A.14 yields:

$$\begin{aligned} -k^2\vec{E} &= \frac{\omega}{c}\vec{k} \times \vec{B} \\ -k^2\vec{E} &= \frac{\omega}{c}(\frac{4\pi\sigma}{ic}\vec{E} - \frac{\omega}{c}\vec{E}) \\ k^2 &= (\frac{w^2}{c^2} - \frac{4\pi ne^2}{mc^2}) \end{aligned} \tag{A.15}$$

Now define the plasma frequency as

$$\omega_p^2 \equiv \frac{4\pi n e^2}{m}, \tag{A.16}$$

which gives

$$k^2 = \frac{w^2}{c^2}(1 - \frac{\omega_p^2}{\omega^2}). \tag{A.17}$$

In order to find the velocity at which different frequencies propagate, the group velocity of the radiation is required,

$$v_{gr} \equiv d\omega/dk = c(1 - \omega_p^2/\omega^2)^{1/2}. \tag{A.18}$$

The time it takes radiation to reach an observer is simply

$$t = \int_0^L \frac{dz}{v_{gr}}. \tag{A.19}$$

The integral allows for changes in the group velocity along the line of sight due to electron density fluctuations. Assuming that $\omega^2 \gg \omega_p^2$, we can expand $1/v_{gr}$ to obtain:

$$\begin{aligned} t &\approx \int_0^L \frac{dz}{c}(1 + \frac{\omega_p^2}{2\omega^2}) \\ &= \frac{L}{c} + \frac{1}{2c\omega^2}\int_0^L \omega_p^2 dz \\ &= t_0 + \frac{2\pi e^2}{mc\omega^2}\int_0^L n dz. \end{aligned} \tag{A.20}$$

The difference in arrival times of radiation at different frequencies is the interesting quantity, given by:

$$\Delta t = \frac{2\pi e^2}{mc\omega^2}\int_0^L n dz. \tag{A.21}$$

with $\Delta t = t - t_0$. By introducing the dispersion measure,

$$\mathrm{DM} = \int_0^{\mathrm{L}} \mathrm{n_e(z)dz}, \tag{A.22}$$

dispersion constant,

$$\alpha_d = \frac{2\pi mc}{e^2} = 2.4 \times 10^{-16}\ \mathrm{pc\ cm^{-3}\ s} \tag{A.23}$$

and switching from angular frequency (rad/s) to a frequency (Hz), Equation A.21 is replaced by:

$$\Delta t = \frac{\mathrm{DM}}{\alpha_d \nu^2}. \tag{A.24}$$

Thus, the time delay for a signal sent through a dispersive medium such as the ISM, goes as $1/\nu^2$. Equation A.24 is useful for comparing the time delay between infinite frequency and some finite frequency. Of more relevance for calculating the dispersion across a finite bandwidth in the radio is the *differential* time delay, i.e. the time delay between the arrival of two frequencies ν_2 and ν_1,

$$\Delta t_{2\rightarrow 1} = \frac{\mathrm{DM}}{\alpha_d}(\frac{1}{\nu_1^2} - \frac{1}{\nu_2^2}) \approx \frac{2\mathrm{DM}\Delta\nu}{\alpha_d \nu_1^3} \tag{A.25}$$

with $\nu_2 = \nu_1 + \Delta\nu$.

For FLIRT, $\nu_1 =$ 74 MHz and the separation between the lowest and highest frequency channels is 1 MHz, so that by Equation A.24, $\Delta t \approx 0.76 \times \mathrm{DM}$ and by Equation A.25, $\Delta t_{2\rightarrow 1} \approx \mathrm{DM}/50$.

A.2 Expected values of dispersion

If radiation emitted by a source has some time-dependence, the effects of dispersion may be measureable. In particular, radio waves from pulsars, which emit regular clocklike pulses of radiation, have been used to map out the ionized component of the ISM (Taylor and Cordes 1993). The amount of dispersion a signal experiences is dependent on both distance from the solar system and galactic latitude. For instance, at the north galactic pole, a pulsar $\sim$ 1 kpc away would have a DM $\sim$ 13 pc cm^{-3} and at a distance of $\sim$ 5 kpc would have DM $\sim$ 16 pc cm^{-3}. The DM quickly saturates as the source is moved above the scale height of the galactic disk. In contrast, in the direction of the galactic center, a pulsar at a distance of $\sim$ 1 kpc would have DM $\sim$ 20 pc cm^{-3} while at a distance of $\sim$ 5 kpc would have a DM $\sim$ 400 pc cm^{-3}. Observing a signal from beyond the galactic center could produce a DM $\sim$ 1400 pc cm^{-3}. Within the Milky Way Galaxy, the observed dispersion measures range from $\sim 1 - 1000$ pc cm^{-3}.

Palmer (1993) has estimated that the dispersion measure due to intergalactic plasma is:

$$\mathrm{DM}_{\mathrm{IGP}} = 2.64 \times 10^4 \Omega_{IGP} \frac{h}{q_0}[(1 + 2q_0 z)^{1/2} - 1] \text{ pc cm}^{-3} \tag{A.26}$$

where Ω_{IGP} is the density of the ionized intergalactic plasma in units of the closure density, h is the Hubble constant $H_0/(100\text{km s}^{-1}\text{ Mpc}^{-1})$ and q_0 is the acceleration parameter. For $z \ll 1$, $\mathrm{DM}_{\mathrm{IGP}} \approx 600 \times z$. This estimate ignores the redshift dependence of both the frequency of the radiation and the electron density. Nevertheless for $z < 1$ it is likely to be reasonable.

Appendix B

Phased Arrays

B.1 Phased array telescopes

FLIRT uses a phased array telescope located in Fallbrook, California. The array consists of 128 $4\lambda \times 1\lambda$ elements, each of which has 8 full-wave dipoles, with alternate dipoles phase reversed to put them on $\lambda/2$ spacing. A phased array is "pointed" by adding phase delays to the signals from all the elements in the array in such a way that they correspond to receiving a plane wave coming from a particular point on the sky. This can be seen relatively easily by looking at Figure B.1. We define $\vec{x_{00}}$ and

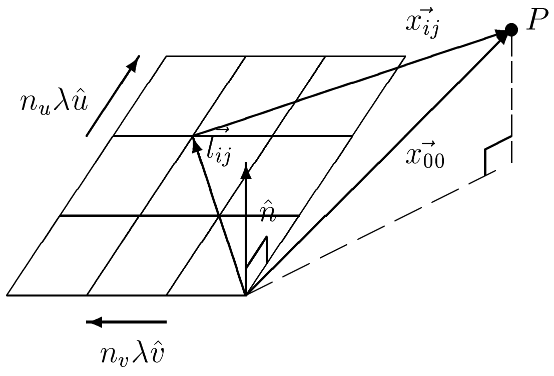

Figure B.1: Schematic of a phased array, showing source position, P, the array normal $\hat{n}$, reference element to source distance, $\vec{x_{00}}$, and arbitrary element to source distance, $\vec{x_{ij}}$. Also drawn are the array element spacings $n_v\lambda\hat{v}$ and $n_u\lambda\hat{u}$

$\vec{x_{ij}}$ as the vectors from the reference element to the source and from the ijth element to the source respectively. Let $\vec{l_{ij}}$ be the vector from the reference element to the ijth element of the array. The power from the elements will have a phase term going as $\vec{k} \cdot \vec{x_{ij}} - \vec{k} \cdot \vec{x_{00}}$. Using the fact that $\vec{l_{ij}} + \vec{x_{ij}} = \vec{x_{00}}$ (see Figure B.1), we find that the delay that should be added to the phase of a signal from the ijth element is given by: $\Delta_{ij} = -\vec{k} \cdot \vec{l_{ij}} = -2\pi(in_u\hat{k} \cdot \hat{u} + jn_v\hat{k} \cdot \hat{v})$, where in_u and jn_v give the spacing between array elements in wavelengths. At Fallbrook, the spacing is 4λ in the E-W direction and 0.9084λ in the N-S direction. The phase delay given above points the array when the wave vector of the source is given with respect to the array normal. A rotation of the coordinates transforms this into right ascension and declination.

References

Atteia, J. L. *et al.* 1987a, *Astrophys. J. Supp. Series*, **64**, 305.

Atteia, J.-L. *et al.* 1987b, *Astrophys. J.*, **320**, L105.

Baars, J. W. M., Genzel, R., Pauliny-Toth, I. I. K., and Witzel, A. 1977, *Astr. Astrophys.*, **61**, 99.

Baird, G. A. *et al.* 1975, *Astrophys. J.*, **196**, L11.

Balsano, R. J. *et al.* 1996, in *Gamma Ray Bursts: 3rd Huntsville Symposium*, ed. C. Kouveliotou, M. F. Briggs, and G. J. Fishman, (Woodbury, New York: AIP), 575.

Balsano, R. J. *et al.* 1998, in *Gamma Ray Bursts: 4th Huntsville Symposium*, ed. C. A. Meegan, R. Preece, and T. Koshut, (Woodbury, New York: AIP), 585.

Band, D. *et al.* 1993, *Astrophys. J.*, **413**, 281.

Baring, M. G. and Harding, A. K. 1997, *Astrophys. J.*, **491**, 663.

Barthelmy, S. 1998, GCN webpage available at http://lheawww.gsfc.nasa.gov/docs/gamcosray/legr/bacodine/gcn_main.html.

Barthelmy, S. D., Butterworth, P. S., Cline, T. L., Gehrels, N., Fishman, G. J., Kouveliotou, C., Meegan, C., and Hurley, K. 1996, in *Gamma Ray Bursts: 3rd Huntsville Symposium*, ed. C. Kouveliotou, M. F. Briggs, and G. J. Fishman, (Woodbury, New York: AIP), 580.

Barthelmy, S. D. *et al.* 1998, in *Gamma Ray Bursts: 4th Huntsville Symposium*, ed. C. A. Meegan, R. Preece, and T. Koshut, (Woodbury, New York: AIP), 99.

Belli, B. M. 1997, *Astrophys. J.*, **479**, L31.

Benz, A. O. 1987, in *Rapid Fluctuations in Solar Flares*, ed. B. R. Dennis, L. E. Orwig, and A. L. Kiplinger, 143.

Benz, A. O. and Paesold, G. 1998, *Astr. Astrophys.*, **329**, 61.

Bhat, P. N. *et al.* 1994, *Astrophys. J.*, **426**, 604.

Bickert, K. and Greiner, J. 1993, in *Compton Gamma-Ray Observatory Symposium*, ed. M. Friedlander, N. Gehrels, and D. Macomb, (Woodbury, New York: AIP), 1059.

Briggs, M. S. *et al.* 1996, *Astrophys. J.*, **459**, 40.

Briggs, M. S. *et al.* 1998. IAU circular 6856.

Chakrabarty, D. 1996. PhD thesis, California Institute of Technology.

Christiansen, W. N. and Hogbom, J. A. 1987, *Radio telescopes*, (Cambridge: Cambridge University Press).

Clarke, T. E., Blaes, O., and Tremaine, S. 1994, *Astron. J.*, **107**, 1873.

Cline, T. L., Mazets, E. P., and Golenetskii, S. V. 1998. IAU circular 7002.

Cline, T. L. *et al.* 1982, *Astrophys. J.*, **255**, L45.

Coles, W. A., Frehlich, R. G., and Kojima, M. 1994, *Proc. I. E. E. E.*, **82**.

Colgate, S. A. 1968, *Canadian J. Phys.*, **46**, S476.

Corbel, S. *et al.* 1997, *Astrophys. J.*, **478**, 624.

Costa, E. *et al.* 1997a, *Nature*, **387**, 783.

Costa, E. *et al.* 1997b. IAU circular 6576.

Crider, A. and Fenimore, E. E. 1996, in *The 3rd Huntsville Symposium on Gamma Ray Bursts*, ed. C. Kouveliotou, M. F. Briggs, and G. J. Fishman, (Woodbury, New York: AIP), 926.

Dessenne, C.-C. *et al.* 1996, *Mon. Not. R. astr. Soc.*, **281**, 977.

Djorgovski, S. G. *et al.* 1997, *Nature*, **387**, 876.

Dwarakanath, K. S. and Shankar, N. U. 1990, *J. Astrophys. Astr.*, **11**, 323.

Erickson, W. C. 1984, *J. Astrophys. Astr.*, **5**, 55.

Fenimore, E. E. 1993, *Astr. Astrophys.*, **97**, 59.

Fenimore, E. E., Epstein, R. I., and Ho, C. 1993, *Astr. Astrophys. Suppl. Ser.*, **97**, 59.

Fenimore, E. E., Klebsadel, R. W., and Laros, J. G. 1996, *Astrophys. J.*, **460**, 964.

Fenimore, E. E., Madras, C. D., and Nayakchin, S. 1996, *Astrophys. J.*, **473**, 998.

Fenimore, E. E., Ramirez, E., and Sumner, M. C. 1998, in *Gamma Ray Bursts: 4th Huntsville Symposium*, ed. C. A. Meegan, R. Preece, and T. Koshut, (Woodbury, New York: AIP), 657.

Feroci, M. *et al.* 1997, in *Proc. SPIE Vol. 3114, EUV, X-Ray, and Gamma-Ray*

Instrumentation for Astronomy VIII, 186.

Feroci, M. *et al.* 1998a, *Astr. Astrophys.*, **332**, L29.

Feroci, M. *et al.* 1998b, GCN notice 153.

Fishman, G. J. *et al.* 1994a, *Science*, **264**, 1313.

Fishman, G. J. and Meegan, C. A. 1995, *Ann. Rev. Astr. Ap.*, **33**, 415.

Fishman, G. J. *et al.* 1989, in *Proceedings of the GRO Science Workshop, Goddard Space Flight Center*, ed. W. N. Johnson, 2.

Fishman, G. J. *et al.* 1994b, *Astrophys. J. Supp. Series*, **92**, 229.

Ford, L. A. *et al.* 1995, *Astrophys. J.*, **439**, 307.

Frail, D. A. 1998, GRB Radio Counterpart webpage available at http://www.nrao.edu/˜dfrail/grb.html.

Frail, D. A. *et al.* 1997a, *Nature*, **389**, 261.

Frail, D. A. *et al.* 1997b, *Astrophys. J.*, **483**, L91.

Frontera, F. *et al.* 1998. IAU circular 6853.

Fruchter, A. S. 1998, *Astrophys. J.* In press, astro-ph/9810224v2.

Fruchter, A. S. *et al.* 1998a, Submitted to ApJ.

Fruchter, A. S. *et al.* 1998b, in *Gamma Ray Bursts: 4th Huntsville Symposium*, ed. C. A. Meegan, R. Preece, and T. Koshut, (Woodbury, New York: AIP), 509.

Galama, T. J., Vreeswijk, P. M., Pian, E., Frontera, F., Doublier, V., and Gonzalez, J.-F. 1998a. IAU circular 6895.

Galama, T. J. *et al.* 1997, *Astrophys. J.*, **486**, L5.

Galama, T. J. *et al.* 1998b, Submitted to Nature, astro-ph/9806175.

Ginzburg, V. L. 1973, *Nature*, **246**, 415.

Giroux, M. L. and Shapiro, P. R. 1998, *Astrophys. J. Supp. Series*, **102**, 191.

Goodman, J. 1997, *New Astr.*, **2**(5), 449.

Goodman, J. 86, *Astrophys. J.*, **308**, 47.

Green, D. A. *et al.* 1996, in *Gamma Ray Bursts: 3rd Huntsville Symposium*, ed. C. Kouveliotou, M. F. Briggs, and G. J. Fishman, (Woodbury, New York: AIP), 617.

Guarnieri, A. *et al.* 1998. IAU circular 6855.

Gunn, J. E. and Peterson, B. A. 1965, *Astrophys. J.*, **142**, 1633.

Gupta, Y., Rickett, B. J., and Coles, W. A. 1993, *Astrophys. J.*, **403**, 183.

Halpern, J., Thorstensen, J., Helfand, D., and Costa, E. 1998, *Nature*, **393**, 41.

Harding, A. K. 1994, *Astrophys. J. Supp. Series*, **90**, 863.

Harris, M. J. and Share, G. H. 1998, in *Gamma Ray Bursts: 4th Huntsville Symposium*, ed. C. A. Meegan, R. Preece, and T. Koshut, (Woodbury, New York: AIP), 67.

Haslam, C. G. T., Salter, C. J., Stoffel, H., and Wilson, W. E. 1982, *Astr. Astrophys. Suppl. Ser.*, **47**, 1.

Hillas, A. M. *et al.* 1998, *Astrophys. J.*, **503**, 744.

Holden, D. N., Munson, C. P., and Devenport, J. C. 1995, *Geophysical Research Letters*, **22**, 889.

Hook, I. M., Duffett-Smith, P. J., and Shakeshaft, J. R. 1992, *Astr. Astrophys.*, **255**, 285.

Horváth, I. 1998, astro-ph 9803077.

Hudec, R. *et al.* 1998, in *Gamma Ray Bursts: 4th Huntsville Symposium*, ed. C. A. Meegan, R. Preece, and T. Koshut, (Woodbury, New York: AIP), 851.

Hurley, K. 1992, in *Gamma-Ray Bursts*, ed. W. Paciesas and G. Fishman, (Woodbury, New York: AIP).

Hurley, K. 1994, *Astrophys. J. Supp. Series*, **90**, 857.

Hurley, K. 1996, in *Gamma Ray Bursts: 3rd Huntsville Symposium*, ed. C. Kouveliotou, M. F. Briggs, and G. J. Fishman, (Woodbury, New York: AIP), 889.

Hurley, K. *et al.* 1996, *Astrophys. J.*, **463**, L13.

Hurley, K. *et al.* 1998. IAU circular 7004.

in 't Zand, J. *et al.* 1998. IAU circular 6854.

Inzani, P., Sironi, G., Mandolesi, N., and Morigi, G. 1982, in *Gamma Ray*

Transients and Related Astrophysical Phenomena, ed. R. E. Lingenfelter, H. S. Hudson, and D. M. Worrall, AIP, 79.

Jackson, P. D. *et al.* 1998, *Astrophys. J.*, **505**, 1.

Jager, R. *et al.* 1997, *Astr. Astrophys.*, **125**, 557.

Jaroszynski, M. 1996, *Astr. Astrophys.*, **305**, 839.

Kai, K. *et al.* 1985. *Solar Radiophysics*, chapter 16. Cambridge University Press.

Kane, S. R. 1972, *Solar Physics*, **27**, 174.

Katz, C. A. 1997. PhD thesis, Massachusetts Institute of Technology.

Katz, C. A., Hewitt, J. N., Moore, C. B., and Corey, B. E. 1998, in *Gamma Ray Bursts: 4th Huntsville Symposium*, ed. C. A. Meegan, R. Preece, and T. Koshut, (Woodbury, New York: AIP), 581.

Katz, C. A., Hewitt, J. N., Moore, C. B., Ellithorpe, J. D., and Rabii, B. 1996, in *The 3rd Huntsville Symposium on Gamma Ray Bursts*, ed. C. Kouveliotou, M. F. Briggs, and G. J. Fishman, (Woodbury, New York: AIP), 651.

Klebesadel, R. *et al.* 1982, *Astrophys. J.*, **259**, L51.

Klebesadel, R. W., Strong, I. B., and Olson, R. A. 1973, *Astrophys. J.*, **182**, L85.

Koranyi, D. M. *et al.* 1995, *Mon. Not. R. astr. Soc.*, **276**, L13.

Kouveliotou, C., Meegan, C. A., Fishman, G. J., Bhat, N. P., Briggs, M. S., Koshut, T. M., Paciesas, W. S., and Pendleton, G. N. 1993, *Astrophys. J.*, **413**, 101.

Kouveliotou, C. *et al.* 1994, *Nature*, **368**, 125.

Kouveliotou, C. *et al.* 1996a, in *The 3rd Huntsville Symposium on Gamma-Ray Bursts*, ed. C. Kouveliotou, M. F. Briggs, and G. J. Fishman, (Woodbury, New York: AIP), 42.

Kouveliotou, C. *et al.* 1996b, *Nature*, **379**, 799.

Kouveliotou, C. *et al.* 1998. IAU circular 6944.

Kraus, J. D. 1986, *Radio Astronomy*, (Powell, Ohio: Cygnus–Quasar Books).

Kulkarni, S. R., Bloom, J. S., Frail, D. A., Ekers, R., Wieringa, M., Wark, R., and Higdon, J. L. 1998a, GCN notice 70.

Kulkarni, S. R. and Frail, D. A. 1993, *Nature*, **365**, 33.

Kulkarni, S. R. *et al.* 1998b, Submitted to Nature, astro-ph/9807001.

Kulkarni, S. R. *et al.* 1998c, *Nature*, **393**, 35.

Lamb, D. Q. 1995, *Publ. Astr. Soc. Pacific*, **107**, 1152.

Laros, J. G. *et al.* 1987, *Astrophys. J.*, **320**, L111.

Lee, B. *et al.* 1997, *Astrophys. J.*, **482**, L125.

Lloyd, N. M. and Petrosian, V. 1998, in *Gamma Ray Bursts: 4th Huntsville Symposium*, ed. C. A. Meegan, R. Preece, and T. Koshut, (Woodbury, New York: AIP), 67.

Makino, F. *et al.* 1987, *Astrophys. J.*, **313**, 662.

Mandolesi, N. *et al.* 1977, *Nature*, **266**, 427.

Massey, R. S. and Holden, D. N. 1995, Available at http://nis-www.lanl.gov/nis-projects/blackbeard/mass.html.

Mazets, E. P. and Golenskii, S. V. 1981, *Astrophys. Space Sci.*, **75**, 47.

McKee, C. R. and Colgate, S. A. 1973, *Astrophys. J.*, **181**, 903.

McLean, D. J. 1985. *Solar Radiophysics*, chapter 3. Cambridge University Press.

Meegan, C. *et al.* 1992, *Nature*, **355**, 143.

Meegan, C. A., Fishman, G. J., and Wilson, R. B. 1985, *Astrophys. J.*, 479.

Meegan, C. A. *et al.* 1998a, in *Gamma Ray Bursts: 4th Huntsville Symposium*, ed. C. A. Meegan, R. Preece, and T. Koshut, (Woodbury, New York: AIP), 3.

Meegan, C. A. *et al.* 1998b, Available at http://www.batse.msfc.nasa.gov/data/grb/catalog.

Mészáros, P. and Rees, M. J. 1993, *Astrophys. J.*, **405**, 278.

Mészáros, P. and Rees, M. J. 1997a, *Astrophys. J.*, **476**, 232.

Mészáros, P. and Rees, M. J. 1997b, *Astrophys. J.*, **482**, L29.

Metzger, M. R., Cohen, J. G., Chaffee, F. H., and Blandford, R. D. 1997a. IAU circular 6676.

Metzger, M. R., Djorgovski, S. G., Kulkarni, S. R., Steidel, C. C., Adelberger, K. L., Frail, D. A., Costa, E., and Fronterra, F. 1997b, *Nature*, **387**, 879.

Mukherjee, S. *et al.* 1998, astro-ph 9802085.

Murakami, T., Tanaka, Y., Kulkarni, S. R., Ogasaka, Y., Sonobe, T., Ogawara, Y., Aoki, T., and Yoshida, T. 1994, *Nature*, **368**, 127.

Narayan, R., Paczyński, B., and Piran, T. 1992, *Astrophys. J.*, **395**, L83.

Nemiroff, R. J. 1994, *Comm. Astrophys.*, **17**(4), 189.

Norris, J. P., Hertz, P., Wood, K. S., and Kouveliotou, C. 1991, *Astrophys. J.*, **366**, 240.

Paciesas, W. S. *et al.* 1989, in *Proc. SPIE Vol. 1159, EUV, X-Ray, and Gamma-Ray Instrumentation for Astronomy and Atomic Physics*, 156.

Paczyński 1998a, in *Gamma Ray Bursts: 4th Huntsville Symposium*, (Woodbury, New York: AIP), 783.

Paczyński, B. 1986, *Astrophys. J.*, **308**, L43.

Paczyński, B. 1995, *Publ. Astr. Soc. Pacific*, **107**, 1167.

Paczyński, B. 1998b, *Astrophys. J.*, **494**, L45.

Paczyński, B. and Rhoads, J. 1993, *Astrophys. J.*, **418**, L5.

Paczyński, B. and Xu, G. 1994, *Astrophys. J.*, **424**, 708.

Palazzi, E. *et al.* 1998, *Astr. Astrophys.*, **336**, L95.

Palmer, D. M. 1993, *Astrophys. J.*, **417**, L25.

Park, H. S. *et al.* 1997, *Astrophys. J.*, **490**, L21.

Pata, F. and Piemonte, A. 1998. IAU circular 6918.

Pedersen, H. *et al.* 1998, *Astrophys. J.*, **496**, 311.

Pendleton, G. N., Briggs, M. S., and Meegan, C. A. 1996, in *Gamma Ray Bursts: 3rd Huntsville Symposium*, ed. C. Kouveliotou, M. F. Briggs, and G. J. Fishman, (Woodbury, New York: AIP), 877.

Pendleton, G. N. *et al.* 1996, *Astrophys. J.*, **464**, 606.

Pendleton, G. N. *et al.* 1997, *Astrophys. J.*, **489**, 175.

Piran, T. 1997, in *Unsolved Problems in Astrophysics*, (Princeton, New Jersey: Princeton University Press), 343.

Piran, T. and Shemi, A. 1993, *Astrophys. J.*, **403**, 67.

Piro, L. *et al.* 1998, GCN notice 155.

Ramanamurthy, P. V. *et al.* 1995, *Astrophys. J.*, **447**, L109.

Rees, M. J. and Mészáros, P. 1992, *Mon. Not. R. astr. Soc.*, **258**, P41.

Rees, M. J. and Mészáros, P. 1994, *Astrophys. J.*, **403**, L93.

Reichart, D. E. *et al.* 1998, *Astrophys. J.* astro-ph/9806082.

Rohlfs, K. and Wilson, T. L. 1996, *Tools of Radio Astronomy*, (Berlin: Springer-Verlag).

Ruffert, M., Janka, H.-T., and Shäfer, G. 1996, in *Gamma Ray Bursts: 3rd Huntsville Symposium*, ed. C. Kouveliotou, M. F. Briggs, and G. J. Fishman, (Woodbury, New York: AIP), 777.

Rybicki, G. B. and Lightman, A. P. 1979, *Radiative Processes in Astrophysics*, (New York: John Wiley & Sons).

Sari, R. and Piran, T. 1997, *Astrophys. J.*, **485**, 270.

Smith, A. F. M. 1975, *Biometrika*, **62**, 407.

Soffitta, P. *et al.* 1998. IAU circular 6884.

Sommer, M. and Müller, D. 1978, *Astrophys. J.*, **222**, L17.

Stairs, I. H. 1998. PhD thesis, Princeton University.

Taylor, G. B., Frail, D. A., Beasley, A. J., and Kulkarni, S. R. 1997, *Nature*, **389**, 263.

Taylor, G. B., Frail, D. A., and Kulkarni, S. R. 1998, GCN notice 40.

Taylor, G. B. *et al.* 1998, *Astrophys. J.*, **502**, L115.

Taylor, J. H. and Cordes, J. M. 1993, *Astrophys. J.*, **411**, 674.

Taylor, J. H., Manchester, R. N., and Lyne, A. G. 1993, *Astrophys. J. Supp. Series*, **88**, 529.

Taylor, J. H. and Weisberg, J. M. 1982, *Astrophys. J.*, **253**, 908.

Tinney, C. *et al.* 1998. IAU circular 6896.

van Paradijs, J. *et al.* 1997, *Nature*, **386**, 686.

Vasisht, G., Kulkarni, S. R., Frail, D. A., and Greiner, J. 1994, *Astrophys. J.*, **431**, L35.

Vietri, M. 1996, *Astrophys. J.*, **471**, L95.

Vietri, M. 1997, *Astrophys. J.*, **488**, 105.

Waxman, E. 1997, *Astrophys. J.*, **489**, L33.

Waxman, E., Kulkarni, S. R., and Frail, D. A. 1998, *Astrophys. J.*, **497**, 288.

Woods, P. *et al.* 1998. IAU circular 6948.

Woosley, S. E. 1993, *Astrophys. J.*, **405**, 273.

Woosley, S. E., Eastman, R. G., and Schmidt, B. P. 1998, Submitted to ApJ, astro-ph/9806299.